IMPROVED TEMPORAL COHERENCE AND SHORT PULSE GENERATION IN FREE ELECTRON LASERS

A thesis submitted to the University of Strathclyde
for the degree of Doctor of Philosophy

June 2013

By
Neil Roger Thompson
Department of Physics and Applied Physics

Declaration

This thesis is the result of the author's original research. It has been composed by the author and has not been previously submitted for examination which has led to the award of a degree.

Signed:

Date:

Abstract

The output from a Self-Amplified Spontaneous Emission (SASE) Free-Electron Laser (FEL) has poor temporal coherence because the SASE process is a localised collective interaction that occurs on a scale far smaller than the typical length of the electron bunch used within the FEL. In this thesis a new technique, called High-Brightness SASE [1], is described in which the temporal alignment between radiation and electrons in the FEL is manipulated using magnetic chicanes. This delocalises the SASE process allowing the temporal coherence length of the radiation to grow exponentially and be extended by up to two orders of magnitude. Simulations are shown which indicate the technique may generate fully transform-limited FEL pulses in the hard X-ray at 0.15 nm. In the second part of the thesis it is shown how the magnetic chicanes may be used to synthesise the effect of an optical cavity with an axial mode structure, and how these axial modes may be phase locked, using concepts from conventional lasers, to produce FEL pulses with durations an order of magnitude shorter than those predicted by other short pulse schemes. This technique is called the Mode-Locked Amplifier FEL [2] and simulations are shown which predict pulse durations of approximately 20 attoseconds in the hard X-ray at 0.15 nm.

Acknowledgements

I must thank my supervisor Brian M^{c}Neil for all his help and for teaching me that having crazy FEL ideas can be a lot of fun. Particularly when you discuss them over a beer or two. Without his idea for the Harmonic Amplifier FEL, which sowed the seeds, this thesis would have been a lot different....

I must also thank Jim Clarke for his support and encouragement and for creating the right conditions within his group at ASTeC for ideas to grow.

Thank you Rachel for helping insulate me from the chaos. XXX

Thank you Izzy, Gracie, Rosie and Isaac for creating the chaos—I wouldn't have it any other way.

Contents

Declaration **2**

Abstract **3**

Acknowledgements **4**

1 Introduction **8**

2 FEL Theory **13**

2.1 Introduction 13

2.1.1 Derivation of the Resonance Condition 14

2.2 Derivation of the One-Dimensional FEL Equations including Pulse Propagation 18

2.2.1 Electron Equations of Motion 19

2.2.2 Wave Equation 27

2.3 Final Form of the Averaged FEL Equations 32

2.4 A Description of the FEL Mechanism 32

2.5 Linear Stability Analysis of FEL Equations 35

2.5.1 A Revised Scaling for the FEL Equations 35

2.5.2 Linearisation of the Equations 37

2.5.3 Solution of Linear Equations for $\delta = 0$ 40

2.5.4 Solution of Linear Equations for $\delta \neq 0$ 42

2.6 FEL Output Properties 45

2.7 Output Properties of the SASE FEL 47

2.7.1 A Typical SASE Output Pulse 50

3 High-Brightness SASE **52**

3.1 Introduction 52

3.2 Numerical Implementation 53
3.3 First Numerical Results 55
3.4 A Numerical Experiment with Random Numbers 58
3.5 Theoretical Model Spectra 60
3.5.1 Spontaneous Emission Spectrum 60
3.5.2 Emission Spectrum with Gain Term 65
3.5.3 Discussion 69
3.6 Numerical Results 69
3.6.1 SASE Control 69
3.6.2 Equal Chicane Delays 76
3.6.3 Random Chicane Delays 82
3.6.4 Prime Number Delays 89
3.6.5 Comparison of Chicane Delay Sequences 100
3.6.6 The Development of Longitudinal Coherence 102
3.7 Numerical Parameter Range Study 105
3.7.1 Effect of Undulator Module Length 105
3.7.2 Effect of Longitudinal Chicane Dispersion 109
3.8 Practical Examples 116
3.8.1 Hard X-Ray HB-SASE 116
3.8.2 Soft X-ray HB-SASE 116
3.8.3 Brightness Comparison 120

4 Mode-Locked Amplifier FEL 122
4.1 Introduction 122
4.2 Generation of Axial Modes 123
4.2.1 Axial Mode Spectrum of a Laser Cavity 124
4.2.2 The Analogy Between HB-SASE and Cavity Lasers 125
4.3 Locking the Modes 125
4.4 Simulation Results 127
4.4.1 One-Dimensional Simulations 128
4.4.2 Three-Dimensional Simulations 133
4.5 Assessment of Tolerances 138
4.5.1 Energy Spread 138
4.5.2 Magnet Stability 139
4.5.3 Energy Stability 140
4.5.4 Conclusion 140

4.6 Further Mode-Locking Development 141
4.6.1 Non-Averaged Code Simulations 141
4.6.2 Mode-Locking with Very Large Energy Spread Beam . . . 143
4.6.3 Mode-Locked Single-Spike SASE 145
4.6.4 Other Developments 147

5 Conclusions and Further Work **149**

Bibliography **152**

Chapter 1

Introduction

The Free-Electron Laser (FEL) was first proposed by Madey in 1971 who published the seminal theory of a small gain process in a relativistic electron beam and undulator system [3]. The first experimental demonstrations of amplification [4] and lasing [5] were achieved at Stanford a few years later. The historical development of the FEL and current prospects for future development are summarised in a number of recent review articles [6, 7, 8].

In the Self-Amplified Spontaneous Emission (SASE) FEL [9, 10], as will be discussed, the cooperation length l_c is a scale length for the local collective instability that develops between the relativistic electrons and the radiation as they co-propagate through an array of alternating polarity dipole magnets called an undulator. The cooperation length controls the coherence length of the radiation output, preventing the SASE FEL from generating transform limited pulses because the electron bunch length is much greater than the cooperation length. In techniques for the generation of short intense pulses within the FEL, which typically involve changing the properties of the electron bunch over a very short section of the bunch then arranging that only that section of the bunch lases, the cooperation length l_c defines the minimum output FEL pulse length. Thus the cooperation length is fundamental—it gives a maximum coherence length and also a minimum pulse length. In this thesis, it is shown how both these limits can be broken by orders of magnitude using magnetic delay sections to manipulate the temporal alignment between electrons and radiation—in Chapter 3 the HB-SASE scheme [1] is described in which it may be possible to generate fully transform limited FEL pulses in the hard X-ray, and in Chapter 4 the Mode-Locked Amplifier FEL [2] is described which may be able to generate FEL pulses

of duration ∼20 as in the hard X-ray, shorter than the typical cooperation length by an order of magnitude.

In order to understand fully the motivation for this work, and to develop a framework in which to assess the effect achieved, it is necessary to first understand the basics of the FEL interaction and how this interaction defines the properties of the output radiation. The principle of operation of the FEL is thus described in Chapter 2 followed by a derivation of a set of differential equations used to describe the FEL interaction within a defined set of conditions. To briefly summarise, the FEL mechanism is an interaction between a collection of relativistic electrons, as they propagate through a transverse magnetic field of periodically alternating polarity, and a co-propagating electromagnetic radiation field, as shown schematically in Figure 1.1. The transverse electric field component couples to the transverse electron velocity allowing an exchange of energy to occur between the electron kinetic energy and the electric field. The mean electron longitudinal velocity is less than the velocity of light c due to the fact that the electron has a rest mass and because the transverse oscillations increase the path length. This means that the electrons progressively slip back with respect to the field and the distance by which an electron slips back, relative to the field, in one period of the magnetic field, defines a resonant wavelength λ_r for which the electron transverse oscillation remains in phase with the transverse electric field component. At the resonant wavelength a sustained transfer of energy can then occur allowing the electron and radiation systems to couple. The resonant wavelength can be adjusted by varying the degree of transverse oscillation and hence the velocity difference between electrons and radiation—in practice this can be achieved by adjusting the strength of the magnetic field. As the electron bunch continues to propagate an instability develops in the coupled electron/radiation system which shifts the electron phase leading to a periodic electron bunching and strong coherently enhanced emission such that the radiation power grows exponentially.

In a SASE FEL the initial field is the spontaneous radiation emitted at the start of the undulator. This emission is noisy, or phase-uncorrelated, due to the random longitudinal positions of the emitting electrons, known as shot noise. The FEL acts as a narrow band amplifier (due to the fact that it relies on a narrow resonance to operate) so the output emission, although coherently enhanced in power due to the fact that the electrons are bunched at the radiation wavelength

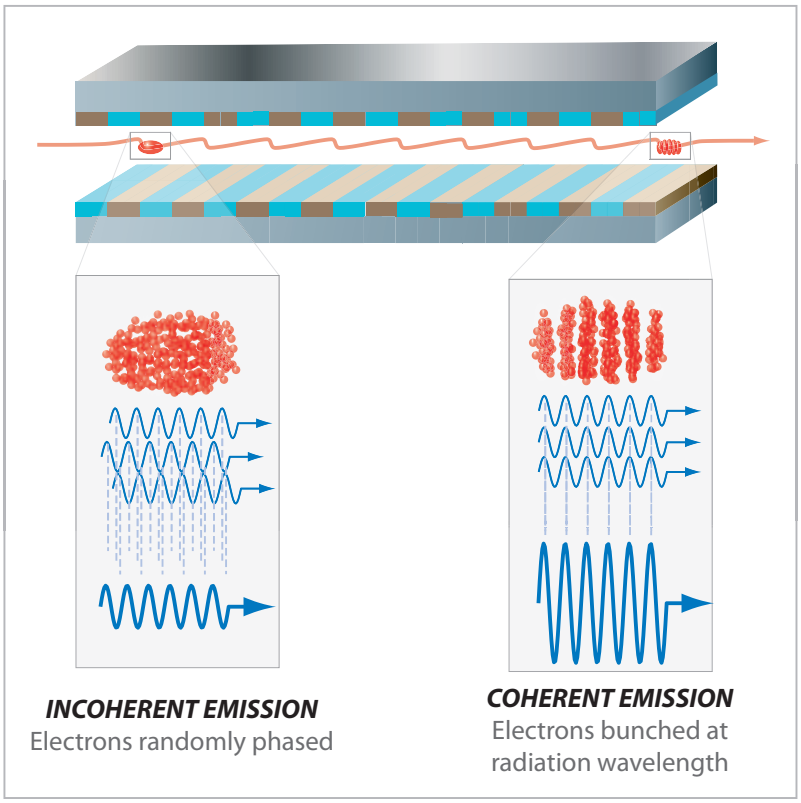

Figure 1.1: Schematic showing the principle of the free-electron laser interaction. As the initially randomly phased electrons oscillate transversely within the undulator, the electric field of the radiation couples to the electron transverse velocity giving a sustained transfer of energy. An instability develops in the coupled electron/radiation system which shifts the electron phase leading to a periodic electron bunching and strong coherently enhanced emission such that the radiation power grows exponentially.

by the interaction, is just amplified noise with the radiation phase found to be discontinuous along the output pulse. Simple 1D analysis shows [11] that the output comprises a series of spikes of random phase and amplitude, separated by a maximum distance $2\pi l_c$, where l_c is the slippage distance in one gain length of the interaction. Thus the relative slippage plays an important part in the evolution of the longitudinal coherence of the FEL output and the cooperation length defines the scale length over which the electrons and radiation can interact collectively. In a typical SASE FEL the electron bunch length greatly exceeds $2\pi l_c$ so the output pulse comprises many spikes and is far from transform limited.

Several methods may be used to improve the temporal coherence of the SASE FEL output. These can be divided into two general classes. In the first class, an

externally injected source of good temporal coherence 'seeds' the FEL interaction so that noise effects are reduced. This seed field may be either at the resonant radiation wavelength, where available, or at a subharmonic which is then up-converted within the FEL. These methods, which include High Gain Harmonic Generation (HGHG) [12, 13, 14, 15] and Echo-Enabled Harmonic Generation (EEHG) [16, 17], rely on a synchronised external seed at the appropriate wavelength, pulse energy and repetition rate. In the second class, the coherence is created by optical manipulation of the FEL radiation itself, for example by spectrally filtering the SASE emission at an early stage for subsequent re-amplification to saturation in a self-seeding method [18, 19, 20, 21], or via the use of an optical cavity [22, 23, 24, 25, 26, 27, 28, 29]. Methods in this class rely on potentially complex material-dependent optical systems which limit the ease and range of wavelength tuning. If an optical cavity is used, the electron source repetition rate should also be in the MHz regime to enable a practical cavity length.

The initial aim of the work in this thesis was to develop an alternative technique for the improvement of SASE longitudinal coherence. The idea, inspired by earlier proposals to use phase shifters to stimulate the production of higher harmonics by disrupting the development of the fundamental [30], was to use magnetic delay sections between modules of a long FEL undulator to repeatedly delay the electron bunch during the FEL process. In this way the longitudinal slippage could be greatly enhanced leading possibly to improved temporal coherence. The details of this work are given in Chapter 3 where it is shown that in fact the longitudinal coherence length can be increased beyond l_c by over two orders of magnitude leading to the enticing prospect of fully transform limited X-Ray FEL pulses [1]. The name given to this scheme is High-Brightness SASE because the improvement in longitudinal coherence gives a corresponding increase in spectral brightness. In the early stages of this work it was discovered that if the delays between undulator sections are equal then a periodic structure emerges in the radiation temporal profile with period equal to the delay applied between modules added to the natural slippage in one module. This effect hinders the development of a smooth temporal profile in the FEL output pulse. In the frequency domain the pulse exhibits evenly spaced spaced side-band frequencies around the FEL resonance with no fixed phase relationship between the sidebands. In the HB-SASE scheme this effect is removed by choosing an appropriate sequence of unequal delays so that the supported sideband frequencies for each delay are

unique and are thus not continually amplified to saturation. Equivalently this is a spectral filtering of the growing radiation.

In Chapter 4 further investigation is made of the modal radiation structure discovered during the development of HB-SASE in Chapter 3. This leads to the concept of the Mode-Locked Amplifier FEL [2]. The idea is to retain the modal structure by using equal delays but to add a modulation to the electron beam with a frequency equal to the spacing between the modes. This introduces side-bands to each mode which overlap neighbouring modes allowing them to phase-lock. In the temporal domain this converts the previously observed periodic structure in the radiation pulse to a train of cleanly separated phase-locked radiation spikes with the duration of each spike dependent on the number of periods in each undulator module, rather than the cooperation length l_c, giving the possibility of pulse durations $\ll l_c$. Simulations for operation in the hard X-ray predict the production of attosecond pulse trains of GW peak power and the duration of each pulse $\sim$20 as. The mode-locked FEL has been studied and developed further, and results included in Chapter 4 include: simulations of the technique in non-averaged codes which can access an enhanced frequency range and suggest the possibility of producing pulse lengths in the zeptosecond regime; study of mode-locking applied to very large energy spread beams such as those produced by plasma based accelerators; application of mode-locking to single-spike SASE operation using parameters of a proposed future light source facility. Other work by the author and co-workers has produced a number of related peer-reviewed publications. The main results of these are summarised at the end of Chapter 4 and include: application of the scheme to the direct amplification of a coherent seed field generated in gas while retaining the attosecond pulse structure of the seed [31]; complete start-to-end simulations using a realistically modelled electron bunch distribution [32]; mode-locking in a oscillator FEL in the high gain and low gain regimes [33].

Finally, Chapter 5 contains a brief conclusion and looks ahead to consider future research possibilities and the prospects for experimental realisation of some of the ideas presented in this thesis.

Chapter 2

FEL Theory

2.1 Introduction

A free-electron laser is a radiation source in which relativistic electrons propagate along the axis of a transversely oscillating dipole magnetic field provided by a device called an undulator. It is well known that an oscillating electron emits electromagnetic radiation with a frequency f equal to that of the oscillation and that this radiation propagates at velocity c as an electromagnetic wave of wavelength $\lambda = c/f$. In the rest frame of a relativistic electron moving along the undulator axis at velocity $v = \beta c$ the magnetic field of period λ_w is Lorentz contracted by the factor $\gamma = (1 - \beta^2)^{-1/2}$ giving emission at wavelength λ_w/γ. To a stationary on-axis observer the wavelength of the propagating field is further contracted by a relativistic Doppler shift of factor $\gamma(1 + \beta)$ giving observed wavelength

$$\lambda = \frac{\lambda_w}{\gamma^2(1+\beta)} \simeq \frac{\lambda_w}{2\gamma^2} \tag{2.1}$$

where the approximation assumes the source is relativistic so that $\beta \simeq 1$. In fact, as will be shown in the following sections, the resonant wavelength of the free-electron laser is slightly modified by a factor $(1+K^2/2)$, where K is the undulator deflection parameter (the maximum deflection angle of the electrons normalised by γ) which depends on the undulator magnetic field and period. K has typical value between 1 and 3 so this correction is relatively small and in fact K can easily be changed by varying the gap between the undulator arrays to smoothly tune the FEL wavelength. Equation (2.1) shows one of the most important characteristics of the free-electron laser—because the electrons are relativistic it

is easy to achieve emission at very short wavelengths. For example, for $\lambda_w = 3$ cm and beam energy 2 GeV, so that $\gamma = eE[\text{eV}]/m_0c^2 \simeq 4000$, the wavelength of emission is around 1 nm, or for beam energy 6 GeV the emission is in the 1Å regime.

In this chapter a derivation is presented of a set of differential equations that describe the FEL interaction. The starting points for the derivation are the Lorentz force equation and the one-dimensional wave equation which become coupled together, and the final form of the equations is amenable to numerical integration. In Chapters 3 and 4 these equations are solved numerically in a simulation code which models the HB-SASE FEL and the Mode-Locked FEL. The equations themselves can be analysed via a linearisation process to gain an insight into the process of exponential gain. An outline of this analysis is given together with the important results. The chapter concludes with a brief summary of the output properties of the SASE FEL.

2.1.1 Derivation of the Resonance Condition

Electron Trajectory in the Undulator

The electron trajectory in the undulator is found from the Lorentz force equation which gives the force on a charged particle of charge q moving in an electric field $\mathbf{E}$ and magnetic field $\mathbf{B}$ with velocity $\mathbf{v}$:

$$\mathbf{F} = q(\mathbf{E} + \mathbf{v} \times \mathbf{B}). \tag{2.2}$$

The relativistic momentum is given by $\mathbf{p} = \gamma m_0 \mathbf{v}$ with $\gamma = (1 - v^2/c^2)^{-1/2}$ and m_0 the rest mass. Writing $\mathbf{F} = \mathrm{d}\mathbf{p}/\mathrm{d}t$, changing the independent variable t to the propagation distance along the undulator axis z using $\mathrm{d}z = v_z \mathrm{d}t$, where $v_z = c\beta_z$, the Lorentz force equation (2.2) can be written

$$\frac{\mathrm{d}(\gamma m_0 \mathbf{v})}{\mathrm{d}z} = \frac{e}{c\beta_z}(\mathbf{E} + \mathbf{v} \times \mathbf{B}). \tag{2.3}$$

In the absence of a radiation field, so that $\mathbf{E} = 0$, and for $\gamma = \gamma_0$, a constant, (2.3) becomes

$$\frac{\mathrm{d}\boldsymbol{\beta}}{\mathrm{d}z} = \frac{e}{\beta_z \gamma m_0 c}(\boldsymbol{\beta} \times \mathbf{B}). \tag{2.4}$$

where $\boldsymbol{\beta} = \mathbf{v}/c$. On axis the planar undulator field is given by the expression $\mathbf{B} = B_w[0, \sin(k_w z), 0]$ so the cross product $\boldsymbol{\beta} \times \mathbf{B} = \hat{\mathbf{x}}\beta_z B_y + \hat{\mathbf{z}}\beta_x B_y$. For relativistic particles $\beta_z \gg \beta_x$ at all times during motion in the undulator so the second term can be neglected. Taking only the $\hat{\mathbf{x}}$ component

$$\frac{d\beta_x}{dz} = \frac{eB_w}{\gamma m_0 c} \sin(k_w z). \tag{2.5}$$

This can now be integrated to determine the transverse velocity component

$$\beta_x = \frac{eB_w}{\gamma m_0 c k_w} \cos(k_w z) \tag{2.6}$$

which has maximum value

$$\beta_{x,\max} = \frac{eB_w}{\gamma m_0 c k_w}. \tag{2.7}$$

The maximum deflection angle $\theta_{\max} = \beta_{x,\max}/\beta \simeq \beta_{x,\max}$ for $\beta \simeq 1$ which can be written

$$\theta_{\max} = \frac{K}{\gamma} \tag{2.8}$$

where

$$K = \frac{eB_w}{m_0 c k_w} \tag{2.9}$$

is the undulator deflection parameter. It should be noted that the rms undulator parameter for a helical undulator, as used in the derivation of the coupled FEL equations later in this thesis, has the equivalent notation

$$\bar{a}_w = \frac{eB_w}{m_0 c k_w}. \tag{2.10}$$

Equation (2.6) can now be expressed

$$\beta_x = \frac{K}{\gamma} \cos(k_w z). \tag{2.11}$$

With β_x known the variation of β_z with z can be determined using

$$\beta_z^2 = \beta^2 - \beta_x^2 \tag{2.12}$$

$$= 1 - \frac{1}{\gamma^2} - \frac{K^2}{\gamma^2} \cos^2(k_w z) \tag{2.13}$$

the cosine term of which can be averaged over one undulator period to give the mean longitudinal velocity

$$\bar{\beta}_z = \left[1 - \frac{1}{\gamma^2} - \frac{K^2}{2\gamma^2}\right]^{1/2} \tag{2.14}$$

$$= \left[1 - \frac{1}{\gamma^2}\left(1 + \frac{K^2}{2}\right)\right]^{1/2} \tag{2.15}$$

$$\simeq 1 - \frac{1}{2\gamma^2}\left(1 + \frac{K^2}{2}\right). \tag{2.16}$$

Here the approximation $(1-x)^n \simeq 1 - nx$ has been used which is valid for $x \ll 1$ and therefore justified because $\gamma \gg 1$.

Interaction with Co-Propagating Wave

The next step is to consider the classical interaction between the electron and a constant co-propagating electromagnetic wave [34]. The change in electron energy due to the EM wave is given by

$$\frac{\mathrm{d}\gamma m_0 c^2}{\mathrm{d}t} = -e\mathbf{E}\cdot\mathbf{v} \tag{2.17}$$

The EM wave can be described as a product of a real envelope $|\xi|$ and an oscillatory term:

$$\mathbf{E}(z,t) = \hat{\mathbf{x}}E_x(z,t) = \hat{\mathbf{x}}|\xi|\cos(kz - \omega t + \phi) \tag{2.18}$$

where k is the wavenumber, ω is the angular frequency and ϕ is the phase. The electron has a transverse velocity component given by (2.6) and this component couples to the transverse electric field of the EM wave. The corresponding electron energy change is thus

$$\frac{\mathrm{d}\gamma m_0 c^2}{\mathrm{d}t} = -eE_x v_x \tag{2.19}$$

$$= -e|\xi|\cos(kz - \omega t + \phi)\frac{cK}{\gamma}\cos(k_w z) \tag{2.20}$$

which becomes

$$\frac{\mathrm{d}\gamma m_0 c^2}{\mathrm{d}t} = -\frac{e|\xi|cK}{2\gamma}\left(\cos[(k-k_w)z - \omega t + \phi] + \cos[(k+k_w)z - \omega t + \phi]\right). \tag{2.21}$$

Equation (2.21) is a superposition of a rapidly varying wave of wavenumber $(k - k_w)$ with a slowly varying wave of wavenumber $(k + k_w)$. The slow wave is known as the 'ponderomotive' wave and from the above has phase

$$\theta = (k + k_w)z - \omega t + \phi. \tag{2.22}$$

with $(k + k_w)z - \omega t$ the phase of the electron with respect to the ponderomotive wave and ϕ the radiation phase.

A continuous exchange of energy can occur when the electron longitudinal velocity is matched to the phase velocity of the ponderomotive wave—in this case the relative phases of the electron transverse velocity component and the ponderomotive wave remain constant as the electron and wave co-propagate through the undulator. Depending on the value of this relative phase, energy is transferred either from the electric field to the electron kinetic energy, or vice versa.

From the condition that the phase velocity of the slow wave $\omega_r/(k + k_w)$ is matched to the electron mean longitudinal velocity $c\bar{\beta}_z$ an expression can be found for the resonant wavelength λ_r of the field at which energy transfer can occur. Using (2.16),

$$\begin{aligned} c\left[1 - \frac{1}{2\gamma^2}\left(1 + \frac{K^2}{2}\right)\right] &= \frac{\omega_r}{k_r + k_w} && (2.23)\\ &= \frac{\frac{2\pi c}{\lambda_r}}{\frac{2\pi}{\lambda_r} + \frac{2\pi}{\lambda_w}} && (2.24)\\ &= c\left(1 + \frac{\lambda_r}{\lambda_w}\right)^{-1} && (2.25)\\ &\simeq c\left(1 - \frac{\lambda_r}{\lambda_w}\right) && (2.26) \end{aligned}$$

where in the final step the approximation is valid because (from (2.1)) $\lambda_r/\lambda_w \ll 1$. Hence rearranging gives the expression for the resonant FEL wavelength

$$\lambda_r = \frac{\lambda_w}{2\gamma^2}\left(1 + \frac{K^2}{2}\right) \tag{2.27}$$

Due to the process described above an electron energy modulation is created along the electron bunch with the direction of energy transfer dependent on the relative phase between electron oscillation and ponderomotive wave. Half of the

electrons gain energy and half of the electrons lose energy. This energy modulation causes the electrons to start to bunch at the resonant electron wavelength allowing a coherent interaction between electrons and radiation. In a constant field, as assumed so far, the bunching process cannot describe any energy gain of the radiation field due to conservation of energy. The gain process can be described by lifting this restriction of a constant field and considering how the electron bunching and field growth self-consistently drive each other in an exponentially unstable feedback loop.

2.2 Derivation of the One-Dimensional FEL Equations including Pulse Propagation

In the previous analysis the electron motion has been examined. The electron transverse velocity due to the magnetic field of the undulator was determined, then the coupling of this transverse velocity with the electric field of a co-propagating electromagnetic wave was examined, leading to the derivation of the FEL resonance condition and the description of electron bunching in a constant radiation field. In order to describe the process of radiation amplification a set of differential equations which describe self-consistently the coupling between electrons and radiation is derived. It is necessary to extend the analysis by lifting the restriction that the radiation field is constant and by considering the evolution of the electron longitudinal velocity. The effect of the magnetic component of the radiation field upon the electrons is also included but shown later to be small enough to be neglected.

The final set of equations, which are those solved numerically in the investigations of the HB-SASE and mode-locked FELs, are averaged over an undulator period. For the planar geometry considered so far (planar undulator and planar co-propagating field) this averaging process is complicated by an oscillatory term in the longitudinal electron motion, leading to the introduction of Bessel functions in the final result. It is therefore convenient to switch to a helical geometry, where the electrons oscillate on a helical path though a helical undulator field with a constant longitudinal velocity. This considerably simplifies the algebra and the final form of the equations derived can be applied to a planar geometry by the inclusion of a Bessel function scaling factor.

2.2.1 Electron Equations of Motion

The helical electric field of the radiation is defined as

$$\mathbf{E} = \frac{1}{\sqrt{2}}\left(\hat{\mathbf{e}}\xi(z,t)e^{i(k_r z-\omega_r t)} + \hat{\mathbf{e}}^*\xi^*(z,t)e^{-i(k_r z-\omega_r t)}\right) \tag{2.28}$$

where $\hat{\mathbf{e}}$ is the helical unit vector

$$\hat{\mathbf{e}} \equiv \frac{\hat{\mathbf{x}} + i\hat{\mathbf{y}}}{\sqrt{2}} \tag{2.29}$$

and $\xi(z,t) = |\xi|e^{i\phi}$ is the complex radiation field envelope specifying the amplitude and phase. The magnetic field is defined as

$$\mathbf{B} = \frac{B_w}{\sqrt{2}}\left(\hat{\mathbf{e}}e^{-ik_w z} + \hat{\mathbf{e}}^* e^{ik_w z}\right) - \frac{i}{\sqrt{2}}\left(\hat{\mathbf{e}}\frac{\xi(z,t)}{c}e^{i(k_r z-\omega_r t)} - \hat{\mathbf{e}}^*\frac{\xi^*(z,t)}{c}e^{-i(k_r z-\omega_r t)}\right) \tag{2.30}$$

where the second term is the magnetic field component of the radiation found from Maxwell's equation

$$\nabla \times \mathbf{E} = -\frac{\partial \mathbf{B}}{\partial t}. \tag{2.31}$$

The rate of change of electron momentum is given by the Lorentz force equation (2.2) rearranged here as

$$\frac{-c\beta_{zj}}{e}\frac{\mathrm{d}\mathbf{p}_j}{\mathrm{d}z} = \mathbf{E} + \frac{1}{\gamma_j m}\left(\mathbf{p}_j \times \mathbf{B}\right). \tag{2.32}$$

Transverse Components of Lorentz Equation

The evolution of the transverse momentum can be determined by taking the scalar product of both sides of (2.32) with the complex conjugate of the helical unit vector, $\hat{\mathbf{e}}^*$, and defining a transverse momentum component

$$p_\perp \equiv p_x - ip_y \tag{2.33}$$

so that

$$\mathbf{p}_j \cdot \hat{\mathbf{e}}^* = \frac{p_\perp}{\sqrt{2}} \tag{2.34}$$

hence

$$\frac{-c\beta_{zj}}{\sqrt{2}e}\frac{\mathrm{d}p_{\perp j}}{\mathrm{d}z} = \left[\mathbf{E} + \frac{1}{\gamma_j m}\left(\mathbf{p}_j \times \mathbf{B}\right)\right] \cdot \hat{\mathbf{e}}^* \tag{2.35}$$

giving

$$\begin{aligned}\frac{-c\beta_z}{e}\frac{\mathrm{d}p_\perp}{\mathrm{d}z} &= \Big[E_x\hat{\mathbf{x}} + E_y\hat{\mathbf{y}} + \frac{1}{\gamma_j m}\left(-p_{zj}B_y\hat{\mathbf{x}} + p_{zj}B_x\hat{\mathbf{y}}\right.\\ &\quad \left. + [p_xB_y - p_yB_x]\hat{\mathbf{z}}\right)\Big]\cdot(\hat{\mathbf{x}} - i\hat{\mathbf{y}}) \qquad (2.36)\\ &= \left[E_x - \frac{1}{\gamma_j m}p_{zj}B_y\right] - i\left[E_y + \frac{1}{\gamma_j m}p_{zj}B_x\right] \qquad (2.37)\\ &= (E_x - iE_y) - \frac{p_{zj}}{\gamma_j m}(B_y + iB_x). \qquad (2.38)\end{aligned}$$

Substituting in the components of the electric and magnetic fields (2.28) and (2.30), written explicitly here as

$$\begin{aligned}E_x &= \frac{1}{2}\left(\xi e^{i(k_rz-\omega_rt)} + \xi^* e^{-i(k_rz-\omega_rt)}\right) \qquad (2.39)\\ E_y &= \frac{1}{2}\left(i\xi e^{i(k_rz-\omega_rt)} - i\xi^* e^{-i(k_rz-\omega_rt)}\right) \qquad (2.40)\\ B_x &= \frac{B_w}{2}\left(e^{-ik_wz} + e^{ik_wz}\right) - \frac{i}{2}\left(\frac{\xi}{c}e^{i(k_rz-\omega_rt)} - \frac{\xi^*}{c}e^{-i(k_rz-\omega_rt)}\right) \qquad (2.41)\\ B_y &= \frac{B_w}{2}\left(ie^{-ik_wz} - ie^{ik_wz}\right) - \frac{i}{2}\left(\frac{\xi}{c}ie^{i(k_rz-\omega_rt)} + \frac{\xi^*}{c}ie^{-i(k_rz-\omega_rt)}\right) \qquad (2.42)\end{aligned}$$

the Lorentz equation (2.38) simplifies to

$$\frac{\mathrm{d}p_{\perp j}}{\mathrm{d}z} = \frac{-e}{\beta_{zj}}\left[\xi e^{i(k_rz-\omega_rt)} + \frac{p_{zj}}{\gamma_j m}\left(-iB_we^{-ik_wz} - \frac{\xi}{c}e^{i(k_rz-\omega_rt)}\right)\right] \qquad (2.43)$$

and with the final substitution $p_{zj} = \gamma_j mc\beta_{zj}$ simplifies to:

$$\frac{\mathrm{d}p_{\perp j}}{\mathrm{d}z} = eiB_we^{-ik_wz} + \frac{1-\beta_{zj}}{\beta_{zj}}\frac{e\xi}{c}e^{i(k_rz-\omega_rt)} \qquad (2.44)$$

Longitudinal Components of Lorentz Equation

Taking the longitudinal component of (2.32) gives

$$\frac{-c\beta_{zj}}{e}\frac{\mathrm{d}p_{zj}}{\mathrm{d}z} = \frac{1}{\gamma_j m}(p_xB_y - p_yB_x). \qquad (2.45)$$

From (2.33) the p_x and p_y can be expressed in terms of $p_\perp$ as

$$p_x = \frac{1}{2}(p_\perp + p_\perp^*) \quad p_y = \frac{i}{2}(p_\perp - p_\perp^*) \qquad (2.46)$$

hence

$$\begin{aligned} p_x B_y - p_y B_x &= \frac{1}{2}(p_\perp + p_\perp^*)B_y - \frac{i}{2}(p_\perp - p_\perp^*)B_x && (2.47)\\ &= \frac{p_\perp}{2}(B_y - iB_x) + \frac{p_\perp^*}{2}(B_y + iB_x) && (2.48)\\ &= \frac{p_\perp}{2}(B_y - iB_x) + c.c. && (2.49)\\ &= \frac{p_\perp}{2}\left(\frac{\xi^*}{c}e^{-i(k_r z - \omega_r t)} - iB_w e^{ik_w z}\right) + c.c && (2.50) \end{aligned}$$

using (2.41) and (2.42). Equation (2.44) expresses the evolution of the transverse momentum as a function of the longitudinal velocity β_{zj}. To complete the coupled system the longitudinal equation (2.45) must be manipulated to give the evolution of β_{zj} as a function of the transverse momentum. The derivative on the LHS of (2.45) can be expanded as

$$\frac{\mathrm{d}p_{zj}}{\mathrm{d}z} = mc\frac{\mathrm{d}}{\mathrm{d}z}(\gamma_j\beta_{zj}) = mc\left(\gamma_j\frac{\mathrm{d}\beta_{zj}}{\mathrm{d}z} + \beta_{zj}\frac{\mathrm{d}\gamma_j}{\mathrm{d}z}\right). \quad (2.51)$$

Changing the independent variable from t to z equation (2.17) becomes

$$\begin{aligned} mc^2\frac{\mathrm{d}\gamma_j}{\mathrm{d}z} &= \frac{-e}{c\beta_{zj}}\mathbf{E}\cdot\mathbf{v} && (2.52)\\ \frac{\mathrm{d}\gamma_j}{\mathrm{d}z} &= \frac{-e}{mc^2\beta_{zj}}\mathbf{E}\cdot\boldsymbol{\beta} && (2.53)\\ &= \frac{-e}{m^2c^3\gamma_j}\mathbf{E}\cdot\mathbf{p} && (2.54)\\ &= \frac{-e}{m^2c^3\gamma_j}(E_x p_x + E_y p_y) && (2.55)\\ &= \frac{-e}{m^2c^3\gamma_j}\left[\frac{1}{2}(p_\perp + p_\perp^*)\left(\frac{1}{2}\xi e^{i(k_r z - \omega_r t)} + c.c.\right)\right. \\ &\quad \left. + \frac{i}{2}(p_\perp - p_\perp^*)\left(\frac{i}{2}\xi e^{i(k_r z - \omega_r t)} - c.c.\right)\right] && (2.56) \end{aligned}$$

which simplifies after some straightforward algebra to

$$\frac{\mathrm{d}\gamma_j}{\mathrm{d}z} = \frac{-e}{2m^2c^3\gamma_j}\left[p_\perp\xi^* e^{-i(k_r z - \omega_r t)} + p_\perp^*\xi e^{i(k_r z - \omega_r t)}\right]. \quad (2.57)$$

Equations (2.50), (2.51) and (2.57) can now be substituted into (2.45) to give

$$\begin{aligned}\frac{-c\beta_{zj}}{e}mc\gamma_j\frac{\mathrm{d}\beta_{zj}}{\mathrm{d}z} &= -\frac{-c\beta_{zj}}{e}\frac{mce}{2m^2c^3\gamma_j}\left[p_\perp\xi^* e^{-i(k_rz-\omega_rt)}+p_\perp^*\xi e^{i(k_rz-\omega_rt)}\right]\\ &\quad+\frac{1}{\gamma_j m}\left[\frac{p_\perp}{2}\left(\frac{\xi^*}{c}e^{-i(k_rz-\omega_rt)}-iB_we^{ik_wz}\right)+c.c.\right] \qquad (2.58)\end{aligned}$$

which through simple rearrangement and manipulation becomes

$$\begin{aligned}\frac{-c\beta_{zj}}{e}mc\gamma_j\frac{\mathrm{d}\beta_{zj}}{\mathrm{d}z} &= \xi^* e^{-i(k_rz-\omega_rt)}\frac{p_\perp}{2mc\gamma_j}(1-\beta_{zj})+\xi e^{i(k_rz-\omega_rt)}\frac{p_\perp^*}{2mc\gamma_j}(1-\beta_{zj})\\ &\quad+\frac{1}{\gamma_j m}\left(\frac{p_\perp^*}{2}iB_we^{-ik_wz}-c.c.\right) \qquad (2.59)\end{aligned}$$

leading to

$$\frac{\mathrm{d}\beta_{zj}}{\mathrm{d}z}=\frac{-e}{2m^2c^3\gamma_j^2}\left[\left(\frac{1-\beta_{zj}}{\beta_{zj}}\right)\left(p_\perp\xi^*\mathrm{e}^{-i(k_rz-\omega_rt)}+c.c.\right)+\frac{ic}{\beta_{zj}}(p_\perp^*B_we^{-ik_wz}-c.c.)\right]. \qquad (2.60)$$

Coupling the Transverse and Longitudinal Equations

Coupling the electron equations can be done by integrating the transverse momentum equation (2.44), holding β_{zj} constant as assumed slowly varying on the timescale of the fast undulator oscillations, to give the transverse momentum $p_{\perp j}$, and then substituting $p_{\perp j}$ into the longitudinal equation (2.60). Integrating (2.44) gives

$$p_{\perp j}=-\frac{eB_w}{k_w}e^{-ik_wz}-\frac{1-\beta_{zj}}{\beta_{zj}}\frac{e\xi}{c}\frac{i}{k_r}e^{i(k_rz-\omega_rt)} \qquad (2.61)$$

which when substituted into (2.60), after some lengthy but straightforward algebra, gives

$$\frac{\mathrm{d}\beta_{zj}}{\mathrm{d}z}=\frac{-e}{2m^2c^3\gamma_j^2}\frac{1-\beta_{zj}}{\beta_{zj}}\left[\left(-\frac{eB_w}{k_w}-\frac{eB_w}{k_r\beta_{zj}}\right)\left(\xi e^{i(k_r+k_w)z-\omega t}+\xi^* e^{-i(k_r+k_w)z-\omega t}\right)\right]. \qquad (2.62)$$

Recognising that $k_r \gg k_w$ the common factor $eB_w/k_r\beta_{zj}$ which originates from the magnetic component of the radiation field can be ignored. Using $\theta=(k_r+k_w)z-\omega t$ for the ponderomotive phase, the expression simplifies to

$$\frac{\mathrm{d}\beta_{zj}}{\mathrm{d}z}=\frac{-e^2B_w}{2k_wm^2c^3\gamma_j^2}\left(\frac{1-\beta_{zj}}{\beta_{zj}}\right)\left(\xi e^{i\theta}+\xi^* e^{-i\theta}\right) \qquad (2.63)$$

The Universal Scaling

The universal scaling can now be applied to the electron equation, and later the wave equation, resulting in a coupled system of equations free of constants. The scaled coordinates are

$$\bar{z} = 2k_w\rho z \tag{2.64}$$

$$\bar{z}_1 = \frac{2k_r\rho}{\bar{\beta}_z}(z - c\bar{\beta}_z t) \tag{2.65}$$

so $\bar{z}$ is the scaled coordinate along the undulator axis and $\bar{z}_1$ is the scaled coordinate in the frame moving at the velocity of the ponderomotive wave. The parameter ρ is known as the FEL parameter, or Pierce parameter, and is defined as

$$\rho = \frac{1}{\gamma_r}\left(\frac{\bar{a}_w\omega_p}{4ck_w}\right)^{\frac{2}{3}} \tag{2.66}$$

where

$$\omega_p = \left(\frac{e^2 n_p}{\epsilon_0 m}\right)^{\frac{1}{2}} \tag{2.67}$$

is the plasma frequency for peak electron number density of the electron bunch n_p. The scaled complex field envelope is

$$A = \frac{e\varepsilon}{mc\omega_p\sqrt{\rho\gamma_r}}. \tag{2.68}$$

It is useful to also express $(k_r z - \omega_r t)$ and the ponderomotive phase $\theta = (k_r + k_w)z - \omega_r t$ in terms of $\bar{z}$ and $\bar{z}_1$. Starting from (2.65) and recalling the discussion prior to equation (2.23) that the phase velocity of the ponderomotive wave is the same as the mean longitudinal velocity,

$$\frac{\omega_r}{k_r + k_w} = c\bar{\beta}_z \tag{2.69}$$

the relation

$$\frac{k_w}{k_r} = \frac{1 - \bar{\beta}_z}{\bar{\beta}_z} \tag{2.70}$$

is found and substituted into (2.65) to give

$$\bar{z}_1 = 2\rho k_r \frac{k_r + k_w}{k_r} z - k_r ct \tag{2.71}$$

$$= 2\rho[(k_r + k_w)z - \omega_r t] \tag{2.72}$$

therefore the scaled ponderomotive phase is

$$\theta = \frac{\bar{z}_1}{2\rho} \tag{2.73}$$

Similarly,

$$k_r z - \omega_r t = (k_r + k_w)z - k_w z - \omega t = \frac{\bar{z}_1}{2\rho} - \frac{\bar{z}}{2\rho} \tag{2.74}$$

therefore

$$k_r z - \omega_r t = \frac{\bar{z}_1 - \bar{z}}{2\rho}. \tag{2.75}$$

A scaled electron energy variable $\bar{p}$ is also derived as follows. Starting with the ponderomotive phase

$$\theta_j = (k_w + k_r)z - \omega_r t_j(z) \tag{2.76}$$

$p_j(z)$ is defined as

$$\frac{\mathrm{d}\theta_j}{\mathrm{d}z} = k_w + k_r - \omega_r \frac{\mathrm{d}t_j}{\mathrm{d}z} \equiv p_j(z) \tag{2.77}$$

It is now shown that p is actually the deviation of the electron energy relative to the resonant energy. Using

$$\frac{\mathrm{d}t_j}{\mathrm{d}z} = \frac{1}{v_j} = \frac{1}{c\beta_{zj}}, \quad \frac{\omega_r}{c} = k_r \tag{2.78}$$

equation (2.77) becomes

$$p_j = \frac{\mathrm{d}\theta_j}{\mathrm{d}z} = k_w - k_r \left(\frac{1 - \beta_{zj}}{\beta_{zj}} \right). \tag{2.79}$$

Using (2.70) to replace k_r in (2.79) gives

$$p_j = k_w \left[1 - \left(\frac{\bar{\beta}_z}{1 - \bar{\beta}_z} \right) \left(\frac{1 - \beta_{zj}}{\beta_{zj}} \right) \right]. \tag{2.80}$$

The resonance condition (2.27) can be written

$$\frac{k_w}{k_r} = \frac{1+\bar{a}_w^2}{2\gamma_r^2} \tag{2.81}$$

so equating (2.81) and (2.70)

$$\frac{1-\bar{\beta}_z}{\bar{\beta}_z} = \frac{1+\bar{a}_w^2}{2\gamma_r^2}. \tag{2.82}$$

This expression can be perturbed away from resonance by adding a small energy deviation $\Delta\gamma = \gamma_j - \gamma_r$ then examined to see the effect on β_{zj} for an individual electron:

$$\begin{aligned}
\frac{1-\beta_{zj}}{\beta_{zj}} &= \frac{1+\bar{a}_w^2}{2(\gamma_r+\Delta\gamma)^2} && (2.83)\\
&= \frac{1+\bar{a}_w^2}{2\gamma_r^2}\left(1+\frac{\Delta\gamma}{\gamma_r}\right)^{-2} && (2.84)\\
&\simeq \frac{1+\bar{a}_w^2}{2\gamma_r^2}\left(1-2\frac{\Delta\gamma}{\gamma_r}\right) && (2.85)\\
&= \frac{k_w}{k_r}\left(1-2\frac{\Delta\gamma}{\gamma_r}\right). && (2.86)
\end{aligned}$$

The right hand side of (2.86) can now be substituted for the final term in (2.80) to give

$$\begin{aligned}
p_j &= k_w\left[1-\frac{\bar{\beta}_z}{1-\bar{\beta}_z}\frac{k_w}{k_r}\left(1-2\frac{\Delta\gamma}{\gamma_r}\right)\right] && (2.87)\\
&= k_w\left[1-\frac{k_r}{k_w}\frac{k_w}{k_r}\left(1-2\frac{\Delta\gamma}{\gamma_r}\right)\right] && (2.88)\\
&= 2k_w\frac{\gamma_j-\gamma_r}{\gamma_r} && (2.89)
\end{aligned}$$

Finally the scaled energy variable is defined as

$$\bar{p}_j \equiv \frac{\mathrm{d}\theta_j}{\mathrm{d}\bar{z}} \tag{2.90}$$

which from the scalings (2.64) becomes

$$\bar{p}_j = \frac{\mathrm{d}\theta_j}{\mathrm{d}\bar{z}} = \frac{1}{2\rho k_w}\frac{\mathrm{d}\theta_j}{\mathrm{d}z} = \frac{1}{2\rho k_w}p_j \tag{2.91}$$

so using (2.89) the scaled electron energy variable is

$$\bar{p}_j = \frac{1}{\rho}\frac{\gamma_j - \gamma_r}{\gamma_r} \tag{2.92}$$

Electron Equations in Scaled Form

From (2.77) and (2.78),

$$\begin{aligned}
\frac{\mathrm{d}p_j}{\mathrm{d}z} &= -\frac{\mathrm{d}}{\mathrm{d}z}\left(\frac{\omega_r}{c\beta_{zj}}\right) && (2.93)\\
&= -\frac{\mathrm{d}}{\mathrm{d}z}\left(k_r\beta_{zj}^{-1}\right) && (2.94)\\
&= \frac{k_r}{\beta_{zj}^2}\frac{\mathrm{d}\beta_{zj}}{\mathrm{d}z}. && (2.95)
\end{aligned}$$

From (2.64) the differential operator transforms as

$$\frac{\mathrm{d}}{\mathrm{d}\bar{z}} = \frac{1}{2\rho k_w}\frac{\mathrm{d}}{\mathrm{d}z} \tag{2.96}$$

therefore

$$\begin{aligned}
\frac{\mathrm{d}\bar{p}_j}{\mathrm{d}\bar{z}} &= \frac{\mathrm{d}^2\theta}{\mathrm{d}\bar{z}^2} && (2.97)\\
&= \frac{1}{4\rho^2k_w^2}\frac{\mathrm{d}^2\theta}{\mathrm{d}z^2} && (2.98)\\
&= \frac{1}{4\rho^2k_w^2}\frac{\mathrm{d}p_j}{\mathrm{d}z} && (2.99)\\
&= \frac{1}{4\rho^2k_w^2}\frac{k_r}{\beta_{zj}^2}\frac{\mathrm{d}\beta_{zj}}{\mathrm{d}z} && (2.100)
\end{aligned}$$

using (2.95) in the final step. An expression for $\mathrm{d}\beta_{zj}/\mathrm{d}z$ has already been derived (equation (2.63)), so substituting this into (2.100) gives

$$\frac{\mathrm{d}\bar{p}_j}{\mathrm{d}\bar{z}} = \frac{1}{4\rho^2k_w^2}\frac{k_r}{\beta_{zj}^2}\frac{-e^2B_w}{2k_wm^2c^3\gamma_j^2}\left(\frac{1-\beta_{zj}}{\beta_{zj}}\right)\left(\xi e^{i\theta} + \xi^* e^{-i\theta}\right). \tag{2.101}$$

This expression can now be simplified by applying the Compton limit which implies $\beta_j \simeq 1$. The assumption is also made that the common factors multiplying the field term vary much more slowly than the field term itself. This allows the

approximation

$$\frac{1-\beta_{zj}}{\beta_{zj}} \simeq \frac{1-\bar{\beta}_z}{\bar{\beta}_z} \tag{2.102}$$

to be applied. Using also the definitions of the undulator parameter $\bar{a}_w$ (2.10), the ρ parameter (2.66) and the scaled field envelope A (2.68), as well as (2.70), the expression (2.101) straightforwardly assumes its final form giving the evolution of the scaled electron energy $\bar{p}_j$ with scaled propagation distance $\bar{z}$ in the presence of the scaled field A:

$$\frac{\mathrm{d}\bar{p}_j}{\mathrm{d}\bar{z}} = -(A(\bar{z},\bar{z}_1)\exp(i\theta_j) + A^*\exp(-i\theta_j)) \tag{2.103}$$

2.2.2 Wave Equation

To complete the coupled system it is necessary to determine a suitable equation describing the propagation of the electromagnetic wave in the presence of the electron bunch. The derivation starts, following [35], with the one dimensional wave equation which describes an electromagnetic wave E driven by a time-dependent current source term J

$$\frac{\partial^2\mathbf{E}}{\partial z^2} - \frac{1}{c^2}\frac{\partial^2\mathbf{E}}{\partial t^2} = \mu_o\frac{\partial\mathbf{J}_\perp}{\partial t}. \tag{2.104}$$

with the electric field defined, as in (2.28), as

$$\mathbf{E} = \frac{1}{\sqrt{2}}\left(\hat{\mathbf{e}}\xi(z,t)e^{i(k_r z-\omega_r t)} + \hat{\mathbf{e}}^*\xi^*(z,t)e^{-i(k_r z-\omega_r t)}\right) \tag{2.105}$$

and the transverse current density given as

$$\mathbf{J}_\perp = -ec\sum_{j=1}^{N}\boldsymbol{\beta}_\perp\delta(\mathbf{r}-\mathbf{r}_j(t)) \tag{2.106}$$

and N the total number of electrons in the pulse. If it is assumed that the electron and radiation pulses have equal cross sectional areas σ and that the field amplitude and electron density are constant across that area, then taking the scalar product of the wave equation with $\hat{\mathbf{e}}^*$ and integrating over the interaction volume gives

$$\left[\frac{\partial^2}{\partial z^2} - \frac{1}{c^2}\frac{\partial^2}{\partial t^2}\right]\left(\xi(z,t)e^{i(k_r z-\omega_r t)}\right) = \frac{2}{\epsilon_0 c^2\sigma}\frac{\partial J_\perp}{\partial t} \tag{2.107}$$

where the transverse current density is now

$$J_\perp = -ec\sum_{j=1}^{N}\beta_\perp\delta(z - z_j(t)). \tag{2.108}$$

The scalings (2.64) and (2.65) can be applied and the left hand side of the wave equation becomes

$$8\rho k_w^2\frac{\bar{\beta}_z}{1-\bar{\beta}_z}\left(\frac{\partial}{\partial\bar{z}}+\frac{\partial}{\partial\bar{z}_1}\right)\left[\frac{\partial}{\partial\bar{z}_1}+\frac{1-\bar{\beta}_z}{2\bar{\beta}_z}\left(\frac{\partial}{\partial\bar{z}}+\frac{\partial}{\partial\bar{z}_1}\right)\right]\left(\xi(\bar{z},\bar{z}_1)e^{i(\bar{z}_1-\bar{z})/2\rho}\right) \tag{2.109}$$

Expanding from the opening square bracket onwards gives

$$e^{i(\bar{z}_1-\bar{z})/2\rho}\left[\frac{\partial\xi}{\partial\bar{z}_1}+\frac{i}{2\rho}\xi+\frac{1-\bar{\beta}_z}{2\bar{\beta}_z}\left(\frac{\partial\xi}{\partial\bar{z}}+\frac{\partial\xi}{\partial\bar{z}_1}\right)\right]. \tag{2.110}$$

so the differential operator

$$\frac{1-\bar{\beta}_z}{2\bar{\beta}_z}\left(\frac{\partial}{\partial\bar{z}}+\frac{\partial}{\partial\bar{z}_1}\right) \tag{2.111}$$

may be neglected if

$$\frac{1-\bar{\beta}_z}{2\bar{\beta}_z}\left|\frac{\partial\xi(\bar{z},\bar{z}_1)}{\partial\bar{z}}+\frac{\partial\xi(\bar{z},\bar{z}_1)}{\partial\bar{z}_1}\right| \ll \left|\frac{i}{2\rho}\xi(\bar{z},\bar{z}_1)+\frac{\partial\xi(\bar{z},\bar{z}_1)}{\partial\bar{z}_1}\right|. \tag{2.112}$$

Using (2.70) this inequality may be rewritten

$$\left|\frac{\partial\xi(\bar{z},\bar{z}_1)}{\partial\bar{z}}+\frac{\partial\xi(\bar{z},\bar{z}_1)}{\partial\bar{z}_1}\right| \ll \left|\frac{2\bar{\beta}_z}{1-\bar{\beta}_z}\frac{\partial\xi(\bar{z},\bar{z}_1)}{\partial\bar{z}_1}+\frac{i\lambda_w\xi(\bar{z},\bar{z}_1)}{\rho\lambda_r}\right| \tag{2.113}$$

which apart from a factor 2 in the final term is identical to that derived in [36] and which gives immediately the condition

$$\lambda_w \gg \lambda\rho. \tag{2.114}$$

Since in a FEL $\lambda_w \simeq 2\gamma^2\lambda_r$, from (2.1), the inequality (2.114) becomes

$$\rho \ll 2\gamma^2 \tag{2.115}$$

which is easily satisfied in the Compton limit. Hence the wave equation can then be written

$$\frac{\partial}{\partial \bar{z}_1}\left[\left(\frac{\partial}{\partial \bar{z}}+\frac{\partial}{\partial \bar{z}_1}\right)\left[\xi(\bar{z},\bar{z}_1)e^{i(z_1-z)/2\rho}\right]+\frac{1}{2\epsilon_0 c\sigma\rho k_w}J_\perp\right]=0 \tag{2.116}$$

where the order of the differentiation has been reversed. The approximation made in the derivation, following the discussion in [36], just means that the field cannot be amplified much over an undulator period and places no constraints on the smoothness of the envelope. For equation (2.116) to be satisfied there are two possibilities. The first possibility is that the term in the square brackets is a general function of $\bar{z}$ plus a constant, in which case its partial derivative with respect to $\bar{z}_1$ is zero. In the limit that the source term $J_\perp \to 0$ the bracketed term represents a wave propagating in free space therefore the general function and constant must be zero for energy and momentum conservation. The other remaining possibility is that the bracketed term itself is equal to zero which gives

$$\left(\frac{\partial}{\partial \bar{z}}+\frac{\partial}{\partial \bar{z}_1}\right)\left[\xi(\bar{z},\bar{z}_1)e^{i(z_1-z)/2\rho}\right]=\frac{-1}{2\epsilon_0 c\sigma\rho k_w}J_\perp \tag{2.117}$$

Performing the differentiation of the left hand side factors out the rapidly varying field term leaving the differential operators acting only on the complex envelope, so the LHS becomes

$$e^{i(\bar{z}_1-\bar{z})/2\rho}\left(\frac{\partial}{\partial \bar{z}}+\frac{\partial}{\partial \bar{z}_1}\right)\xi(\bar{z},\bar{z}_1). \tag{2.118}$$

Using (2.106) with $\beta_\perp = p_\perp/(\gamma mc)$ and

$$p_\perp = \frac{eB_w}{k_w}e^{-ik_w z} \tag{2.119}$$

which is the first term of (2.61) (therefore ignoring the radiation field contribution to the electron transverse momentum) and which once transformed using (2.64) to $\bar{z}$ becomes

$$p_\perp = \frac{eB_w}{k_w}e^{-i\bar{z}/2\rho} \tag{2.120}$$

and transforming the δ-function to

$$\delta(z-z_j(t)) = 2k_w\rho\frac{\bar{\beta}_z}{1-\bar{\beta}_z}\frac{\delta(\bar{z}_1-\bar{z}_{1j})}{\beta_{zj}} \tag{2.121}$$

the wave equation can eventually be written

$$\left(\frac{\partial}{\partial\bar{z}}+\frac{\partial}{\partial\bar{z}_1}\right)\xi(\bar{z},\bar{z}_1)=\frac{e^2B_wk_r}{\varepsilon_0\sigma k_w^2\gamma_j mc\beta_{zj}}\sum_{j=1}^{N}e^{-i(\bar{z}_1-\bar{z})/2\rho}e^{-i\bar{z}/2\rho}\delta(\bar{z}_1-\bar{z}_{1j}). \quad (2.122)$$

Now also transforming the field envelope using (2.68) and substituting the definition of the undulator parameter (2.10) some algebraic manipulation gives

$$\left(\frac{\partial}{\partial\bar{z}}+\frac{\partial}{\partial\bar{z}_1}\right)A(\bar{z},\bar{z}_1)=\frac{2k_r\rho}{n_p\sigma}\sum_{j=1}^{N}e^{-i\bar{z}_1/2\rho}\delta(\bar{z}_1-\bar{z}_{1j}). \quad (2.123)$$

The term $n_p\sigma$ is the electron number density multiplied by the cross sectional area, and therefore gives the number of electrons per unit length. The term $2k_r\rho$, as seen from (2.65), is $1/l_c$ therefore

$$n_{\|p}=\frac{n_p\sigma}{2k_r\rho}=l_cn_p\sigma \quad (2.124)$$

is the peak number of electrons per unit length in $\bar{z}_1$. The product of the two exponential terms in (2.122) has given $\exp(-i\bar{z}_1/2\rho)=\exp(-i\theta)$ with θ the ponderomotive phase. As a final step to convert the wave equation into a form suitable for numerical integration, it is integrated over a regions one radiation wavelength long $\bar{z}_1-2\pi\rho\le\bar{z}_1\le\bar{z}_1+2\pi\rho$ as follows:

$$\int_{\bar{z}_1-2\pi\rho}^{\bar{z}_1+2\pi\rho}\left(\frac{\partial}{\partial\bar{z}}+\frac{\partial}{\partial\bar{z}_1}\right)A(\bar{z},\bar{z}_1)\mathrm{d}\bar{z}_1=\frac{1}{n_{\|p}}\int_{\bar{z}_1-2\pi\rho}^{\bar{z}_1+2\pi\rho}\sum_{j=1}^{N}e^{-i\bar{z}_1/2\rho}\delta(\bar{z}_1-\bar{z}_{1j})\mathrm{d}\bar{z}_1. \quad (2.125)$$

The radiation field envelope can now be replaced by a local value $\bar{A}$ which is constant over the integration window $\bar{A}(\bar{z})=[A(\bar{z},\bar{z}_1+2\pi\rho)+A(\bar{z},\bar{z}_1-2\pi\rho)]/2$ and the order of the integration and summation can be reversed on the RHS giving

$$\left(\frac{\partial}{\partial\bar{z}}+\frac{\partial}{\partial\bar{z}_1}\right)\bar{A}(\bar{z})\int_{\bar{z}_1-2\pi\rho}^{\bar{z}_1+2\pi\rho}\mathrm{d}\bar{z}_1=\frac{1}{n_{\|p}}\sum_{j=1}^{N}\int_{\bar{z}_1-2\pi\rho}^{\bar{z}_1+2\pi\rho}e^{-i\bar{z}_1/2\rho}\delta(\bar{z}_1-\bar{z}_{1j})\mathrm{d}\bar{z}_1. \quad (2.126)$$

Using the δ-function sampling property

$$\int_{T-\epsilon}^{T+\epsilon}f(t)\,\delta(t-T)\,\mathrm{d}t=f(T) \quad (2.127)$$

and evaluating the definite integral on the LHS the equation becomes

$$\left(\frac{\partial}{\partial\bar{z}}+\frac{\partial}{\partial\bar{z}_1}\right)\bar{A}(\bar{z},\bar{z}_1)\times 4\pi\rho = \frac{1}{n_{\|p}}\sum_{j=1}^{N_\lambda}e^{-i\bar{z}_{1j}/2\rho} \tag{2.128}$$

$$\left(\frac{\partial}{\partial\bar{z}}+\frac{\partial}{\partial\bar{z}_1}\right)\bar{A}(\bar{z},\bar{z}_1) = \frac{1}{4\pi\rho n_{\|p}}\sum_{j=1}^{N_\lambda}e^{-i\bar{z}_{1j}/2\rho} \tag{2.129}$$

$$= \frac{1}{N_\lambda}\sum_{j=1}^{N_\lambda}e^{-i\theta_j} \tag{2.130}$$

where $\theta_j = \bar{z}_{1j}/2\rho$ is the ponderomotive phase of the jth electron (from (2.73)). The sum on the RHS is now taken over the number of electrons per radiation wavelength slice N_λ. The term on the RHS is therefore an average over a wavelength of the electrons' complex phasors. If all electrons have the same phase the complex phasors all point in the same direction and the average is unity. If the electrons have evenly distributed phases over the interval $[0,\, 2\pi)$ the phasors all cancel and the average is zero. The term

$$b(\bar{z},\bar{z}_1)\equiv\frac{1}{N_\lambda}\sum_{j=1}^{N_\lambda}e^{-i\theta_j}=\langle e^{-i\theta_j}\rangle \tag{2.131}$$

therefore quantifies the 'bunching' of the electrons, and is referred to as the 'bunching parameter'. The final averaged form of the wave equation is therefore

$$\left(\frac{\partial}{\partial\bar{z}}+\frac{\partial}{\partial\bar{z}_1}\right)A(\bar{z},\bar{z}_1)=\chi\left(\bar{z}_1\right)b\left(\bar{z},\bar{z}_1\right)=\chi\left(\bar{z}_1\right)\langle e^{-i\theta_j}\rangle \tag{2.132}$$

where the field term A is now understood to represent the average value of the complex field envelope over a radiation period and a normalised current weighting parameter $\chi(\bar{z}_1)$ has been introduced to allow for a current distribution that varies along the electron bunch.

2.3 Final Form of the Averaged FEL Equations

The final set of universally scaled one-dimensional FEL equations, which describe self-consistently the coupled system of electrons and co-propagating wave, comprise equations (2.90), (2.103) and (2.132), restated here as a complete set as

$$\frac{\mathrm{d}\theta_j}{\mathrm{d}\bar{z}} = \bar{p}_j \tag{2.133}$$

$$\frac{\mathrm{d}\bar{p}_j}{\mathrm{d}\bar{z}} = -\left(A\left(\bar{z},\bar{z}_1\right)\exp\left(i\theta_j\right)+c.c.\right) \tag{2.134}$$

$$\left(\frac{\partial}{\partial\bar{z}}+\frac{\partial}{\partial\bar{z}_1}\right)A\left(\bar{z},\bar{z}_1\right) = \chi\left(\bar{z}_1\right)b\left(\bar{z},\bar{z}_1\right)=\chi\left(\bar{z}_1\right)\langle e^{-i\theta}\rangle. \tag{2.135}$$

with $\theta_j = (k_w+k_r)z-\omega_r t$ the electron ponderomotive phase, $\bar{p}_j = (\gamma_j-\gamma_r)/\rho\gamma_j$ the scaled electron energy, A the scaled complex field envelope, $\bar{z} = 2k_w\rho z$ the scaled coordinate along the undulator axis, $\bar{z}_1 = 2k_r\rho(z-c\bar{\beta}_z t)/\bar{\beta}_z$ the coordinate in the frame moving at the velocity of the ponderomotive wave, $\chi(\bar{z}_1)$ the normalised current weighting and $b = \langle e^{i\theta_j}\rangle$ the bunching parameter. For N electrons this is therefore a system of $2N+1$ equations.

2.4 A Description of the FEL Mechanism

This section brings together some of the concepts discussed so far to provide a descriptive account of the FEL mechanism, following that given in [6]. First the steady state approximation is applied to the FEL equations (2.133–2.135). In this approximation the assumption is made that the slippage length $N_w\lambda_r$ is much shorter than the electron pulse length l_b, so that the current profile can be treated as a constant $\chi\left(\bar{z}_1\right) = 1$. It is also assumed that all other electron properties, including the bunching parameter b, do not vary along the bunch. Under these assumptions the derivative of A with respective to $\bar{z}_1$ can be neglected [37], removing the effect on the system of the relative slippage between radiation and electron bunch (otherwise known as *pulse propagation*) from the analysis. The wave equation (2.135) can then be written so that the field is expressed explicitly

in terms of its amplitude and phase:

$$\frac{\mathrm{d}}{\mathrm{d}\bar{z}}|A|e^{i\phi} = |A|ie^{i\phi}\frac{\mathrm{d}\phi}{\mathrm{d}\bar{z}} + e^{i\phi}\frac{\mathrm{d}A}{\mathrm{d}\bar{z}} \tag{2.136}$$

$$= e^{i\phi}\left[|A|i\frac{\mathrm{d}\phi}{\mathrm{d}\bar{z}} + \frac{\mathrm{d}A}{\mathrm{d}\bar{z}}\right] = \langle e^{-i\theta}\rangle \tag{2.137}$$

which can be rearranged to give

$$|A|i\frac{\mathrm{d}\phi}{\mathrm{d}\bar{z}} + \frac{\mathrm{d}A}{\mathrm{d}\bar{z}} = \langle e^{-i(\theta+\phi)}\rangle \tag{2.138}$$

$$= \langle\cos(\theta+\phi)\rangle - i\langle\sin(\theta+\phi)\rangle. \tag{2.139}$$

Now equating real and imaginary parts, the evolution of the field amplitude A is given by

$$\frac{\mathrm{d}A}{\mathrm{d}\bar{z}} = \langle\cos(\theta+\phi)\rangle \tag{2.140}$$

and the evolution of the field phase ϕ is given by

$$\frac{\mathrm{d}\phi}{\mathrm{d}\bar{z}} = -\frac{1}{|A|}\langle\sin(\theta+\phi)\rangle. \tag{2.141}$$

Recall also equation (2.21) which described the energy transfer between an electron and co-propagating field. This is rewritten here, neglecting the fast varying wave and constants, leaving only the ponderomotive wave, as

$$\frac{\mathrm{d}\gamma}{\mathrm{d}t} \propto -A\cos(\theta+\phi). \tag{2.142}$$

The free-electron laser interaction is now described with the aid of Equations (2.140–2.142) and Figure 2.1:

- **Panel (a)**: Consider an initial electron beam with electrons distributed evenly in phase, propagating in the presence of a small field with $A \ll 1$ and initial phase $\phi_0 = 0$. From inspection of (2.142) no energy change occurs for $\theta = \pi/2$ or $\theta = 3\pi/2$. However for $\pi < \theta < 3\pi/2$ the electrons gain energy and for $0 \leq \theta < \pi/2$ and $3\pi/2 < \theta \leq 2\pi$ the electrons lose energy. The higher energy electrons move ahead, and the lower energy electrons move back, giving a small bunching developing at $\theta = 3\pi/2$. The forces that bunch the electrons, represented by the red arrows, can be considered as a series of potential wells Φ travelling at the resonant electron velocity.

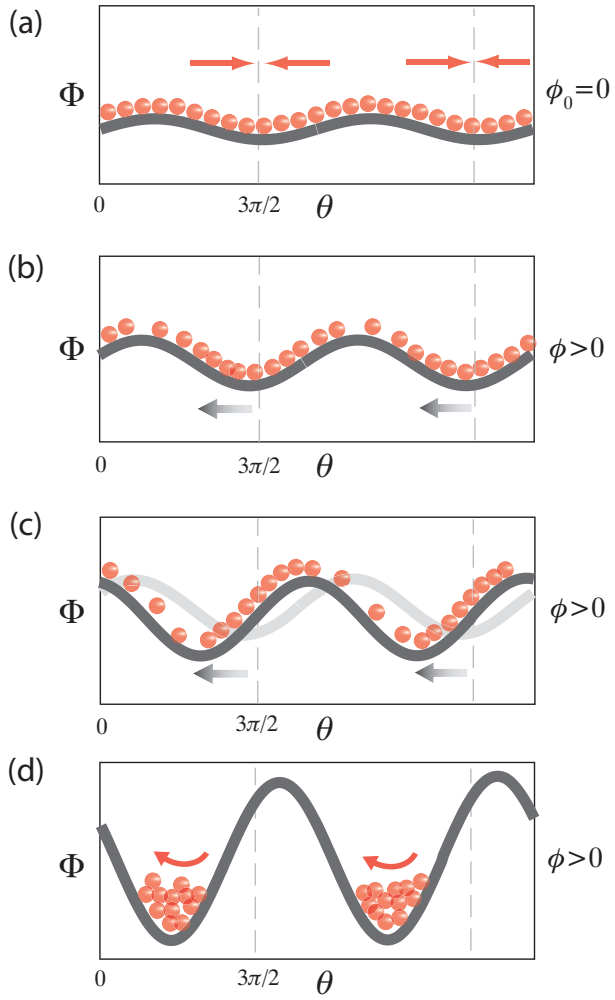

Figure 2.1: Schematic showing the principle of the FEL interaction.

The bunching at phase $3\pi/2$ cannot drive a change in the field amplitude, because at this phase, from equation (2.140), $\mathrm{d}A/\mathrm{d}\bar{z} = 0$. However the bunching can drive a change in the radiation phase because from equation (2.141) $\mathrm{d}\phi/\mathrm{d}\bar{z} > 0$ and quite large because A is small.

- **Panel (b)**: Now that $\phi > 0$ the potential well is shifted to the left and the weakly bunched electrons are raised in potential energy. They start to fall into the potential well, losing kinetic energy to the radiation field (from equation (2.142)) which increases the depth of the well. They also become more strongly bunched.

- **Panel (c)**: The radiation phase continues to be driven rapidly and the process of phase shifting, electron bunching and energy exchange to the

field continues exponentially until from equation (2.141) the field becomes large enough to slow down the phase change.

- **Panel (d)**: The system now enters the nonlinear saturation regime where the the strongly bunched electrons start to regain energy from the field.

In the following section the set of equations (2.133–2.135) are studied further to obtain an analytic formulation of the expontential gain mechanism described here.

2.5 Linear Stability Analysis of FEL Equations

The set of $2N+1$ differential equations (2.133-2.135), where N is the number of electrons in the system, are those solved in the numerical simulation code used to study the concepts presented in this thesis. It is not feasible however to extract an analytic solution to such a large set of nonlinear differential equations. In this section, the steady state approximation is applied once again, so the evolution of the field term with $\bar{z}_1$ can be neglected, and the equations are converted into a set of just three linear ordinary differential equations which *can* then be solved analytically to obtain a solution. This solution describes the exponential increase in the radiation field intensity and gives some further insight into the FEL interaction.

The process involves linearising equations (2.133–2.135) by examining their behaviour in the presence of a small perturbation applied to the initial conditions, then redefining the electron variables as *collective variables* [38] which represent the collective behaviour of the complete set of electrons.

2.5.1 A Revised Scaling for the FEL Equations

It is convenient to introduce a slightly different scaling more suitable for the discussion of the collective FEL instability and the high gain regime [37]. The electron phase and energy θ_j and $\bar{p}_j$ and radiation field complex amplitude A are redefined in terms of the detuning parameter δ

$$\tilde{\theta}_j = \theta_j - \delta\bar{z}, \quad \tilde{p}_j = \bar{p}_j - \delta, \quad \tilde{A} = Ae^{i\delta\bar{z}} \tag{2.143}$$

where

$$\delta = \frac{1}{2\rho}\frac{\langle\gamma\rangle_0^2 - \gamma_r^2}{\gamma_r^2} \tag{2.144}$$

which for $|(\langle\gamma\rangle_0 - \gamma_r)/\langle\gamma\rangle_0| \ll 1$ reduces to

$$\delta = \frac{1}{\rho}\frac{\langle\gamma\rangle_0 - \gamma_r}{\gamma_r}. \tag{2.145}$$

This scaling will later enable an examination of the dependence of the FEL exponential instability on the electron energy detuning δ. Equation (2.133) transforms as follows:

$$\frac{\mathrm{d}\theta_j}{\mathrm{d}\bar{z}} = \frac{\mathrm{d}}{\mathrm{d}\bar{z}}(\tilde{\theta}_j + \delta\bar{z}) \tag{2.146}$$

$$= \frac{\mathrm{d}\tilde{\theta}_j}{\mathrm{d}\bar{z}} + \delta = \tilde{p}_j + \delta \tag{2.147}$$

therefore

$$\frac{\mathrm{d}\tilde{\theta}_j}{\mathrm{d}\bar{z}} = \tilde{p}_j. \tag{2.148}$$

Equation (2.134) transforms as

$$\frac{\mathrm{d}\bar{p}_j}{\mathrm{d}\bar{z}} = \frac{\mathrm{d}}{\mathrm{d}\bar{z}}(\tilde{p}_j + \delta) = \frac{\mathrm{d}\tilde{p}_j}{\mathrm{d}\bar{z}} = -\tilde{A}e^{-i\delta\bar{z}}e^{i(\tilde{\theta}_j+\delta\bar{z})} - \tilde{A}^* e^{i\delta\bar{z}}e^{-i(\tilde{\theta}_j+\delta\bar{z})} \tag{2.149}$$

$$= -\tilde{A}e^{i\tilde{\theta}_j} - \tilde{A}^* e^{-i\tilde{\theta}_j} \tag{2.150}$$

and finally Equation (2.135) transforms in the steady state case ($\partial A/\partial\bar{z}_1 = 0$) as

$$\frac{\mathrm{d}A}{\mathrm{d}\bar{z}} = \frac{\mathrm{d}}{\mathrm{d}\bar{z}}(\tilde{A}e^{-i\delta\bar{z}}) \tag{2.151}$$

$$= \frac{\mathrm{d}\tilde{A}}{\mathrm{d}\bar{z}}e^{-i\delta\bar{z}} - \tilde{A}i\delta e^{-i\delta\bar{z}} = \langle e^{-i(\tilde{\theta}_j+\delta\bar{z})}\rangle \tag{2.152}$$

which after multiplying through by $e^{i\delta\bar{z}}$ and rearranging becomes

$$\frac{\mathrm{d}\tilde{A}}{\mathrm{d}\bar{z}} = \langle e^{-i\tilde{\theta}_j}\rangle + i\delta\tilde{A} \tag{2.153}$$

so the complete set of equations (2.133–2.134), remembering that in the steady state $\partial A/\partial\bar{z}_1 = 0$, becomes

$$\frac{\mathrm{d}\tilde{\theta}_j}{\mathrm{d}\bar{z}} = \tilde{p}_j \tag{2.154}$$

$$\frac{\mathrm{d}\tilde{p}_j}{\mathrm{d}\bar{z}} = -\tilde{A}e^{i\tilde{\theta}_j} - \tilde{A}^* e^{-i\tilde{\theta}_j} \tag{2.155}$$

$$\frac{\mathrm{d}\tilde{A}}{\mathrm{d}\bar{z}} = \langle e^{-i\tilde{\theta}} \rangle + i\delta.\tilde{A} \tag{2.156}$$

Compared to the original set of equations (2.133-2.135) a term $i\delta\tilde{A}$ has appeared in the final equation which represents a shift in the radiation resonant wavelength due to the electron energy detuning δ.

2.5.2 Linearisation of the Equations

It is assumed that the initial state of the system is no field, with an unbunched, uniform density mono-energetic electron beam. The initial conditions are thus

$$\tilde{A}(0) = \tilde{A}_0 = 0, \quad \tilde{p}_j(0) = \tilde{p}_{j0}, \quad \tilde{\theta}_j(0) = \tilde{\theta}_{0j} \tag{2.157}$$

with $\tilde{\theta}_{0j}$ evenly distributed over the interval $[0, 2\pi)$. Small perturbations are applied to the electron variables so that

$$\tilde{p}_j(z) = \tilde{p}_{0j} + \tilde{p}_{1j} \tag{2.158}$$

and

$$\tilde{\theta}_j(z) = \tilde{\theta}_{0j} + \tilde{\theta}_{1j} \tag{2.159}$$

where $|\tilde{p}_{1j}| \ll 1$ and $|\tilde{\theta}_{1j}| \ll 1$. In the following the dot notation $\dot{x} \equiv \mathrm{d}x/\mathrm{d}\bar{z}$ is used for convenience.

Linearisation of $\dot{\tilde{A}}$

Substituting the perturbation (2.159) into equation (2.156) gives

$$\dot{\tilde{A}} = \langle e^{-i(\tilde{\theta}_0 + \tilde{\theta}_1)} \rangle + i\delta\tilde{A} \tag{2.160}$$

$$= \langle e^{-i\tilde{\theta}_0} e^{-i\tilde{\theta}_1} \rangle + i\delta\tilde{A} \tag{2.161}$$

$$= \langle e^{-i\tilde{\theta}_0}(1 - i\tilde{\theta}_1) \rangle + i\delta\tilde{A} \tag{2.162}$$

$$= \langle e^{-i\tilde{\theta}_0} \rangle - \langle i\tilde{\theta}_1 e^{-i\tilde{\theta}_0} \rangle + i\delta\tilde{A} \tag{2.163}$$

where the approximation $e^x \approx 1 + x$ when $x \ll 1$ has been applied. Before being perturbed the electrons are initially distributed evenly over all phases $[0,\, 2\pi)$ so the first term $\langle e^{-i\tilde{\theta}_0} \rangle = 0$. A new collective variable

$$b \equiv -\langle i\tilde{\theta}_1 e^{-i\tilde{\theta}_0} \rangle \tag{2.164}$$

can now be defined so that (2.163) becomes

$$\dot{\tilde{A}} = b + i\delta\tilde{A} \tag{2.165}$$

with b representing the electron beam bunching.

Linearisation of $\dot{\tilde{p}}$

Substituting perturbation (2.159) into equation (2.155) gives

$$\begin{aligned} \dot{\tilde{p}}_j &= -\tilde{A}e^{i(\tilde{\theta}_{0j}+\tilde{\theta}_{1j})} - \tilde{A}^* e^{-i(\tilde{\theta}_{0j}+\tilde{\theta}_{1j})} && (2.166) \\ &= -\tilde{A}\left[e^{i\tilde{\theta}_{0j}}(1 + i\tilde{\theta}_{1j})\right] - \tilde{A}^*\left[-e^{i\tilde{\theta}_{0j}}(1 - i\tilde{\theta}_{1j})\right] && (2.167) \end{aligned}$$

which, because $\tilde{A}$ is small and the perturbation $\tilde{\theta}_{1j}$ is small, can be simplified by neglecting terms with the products $\tilde{A}\tilde{\theta}_{ij}$ and $\tilde{A}^*\tilde{\theta}_{ij}$. Making this assumption and multiplying both sides by $e^{-i\tilde{\theta}_{j0}}$ gives

$$\dot{\tilde{p}}_j e^{-i\tilde{\theta}_{j0}} = -\tilde{A} - \tilde{A}^* e^{-2i\tilde{\theta}_{j0}} \tag{2.168}$$

the second term of which again equates to zero when averaged over all electrons giving

$$\langle \dot{\tilde{p}}\, e^{-i\tilde{\theta}_0} \rangle = -\tilde{A}. \tag{2.169}$$

From (2.158) it can be seen that $\dot{\tilde{p}}_j = \dot{\tilde{p}}_1$ therefore

$$\langle \dot{\tilde{p}}_1\, e^{-i\tilde{\theta}_0} \rangle = -\tilde{A}. \tag{2.170}$$

Another collective variable can now be defined as

$$P \equiv \langle \tilde{p}_1 e^{-i\tilde{\theta}_0} \rangle \tag{2.171}$$

which is a phase-momentum average [38] and can be interpreted as the Fourier coefficient of the beam energy modulation. Therefore,

$$\dot{P} = \langle \dot{\tilde{p}}_1 e^{-i\tilde{\theta}_0} \rangle \tag{2.172}$$

and by combining (2.170) and (2.172) it is seen that

$$\dot{P} = -\tilde{A}. \tag{2.173}$$

Linearisation of $\dot{\theta}$

So far two of the equations (2.154-2.156) have been linearised leading to the definition of two new collective variables b and P and linearised equations

$$\dot{\tilde{A}} = f(b, \delta, \tilde{A}) \tag{2.174}$$

$$\dot{P} = f(\tilde{A}). \tag{2.175}$$

To complete the set of three coupled linearised equations it is necessary to find the equation for the evolution of b. Differentiating (2.164) gives

$$\dot{b} = -\langle i\dot{\tilde{\theta}}_1 e^{-i\tilde{\theta}_0} \rangle. \tag{2.176}$$

Now substituting the perturbations (2.159) and (2.158) into (2.154) gives

$$\frac{\mathrm{d}}{\mathrm{d}\bar{z}}(\tilde{\theta}_{0j} + \tilde{\theta}_{1j}) = \tilde{p}_{0j} + \tilde{p}_{1j} \tag{2.177}$$

therefore $\dot{\tilde{\theta}}_{1j} = \tilde{p}_{1j}$ and (2.176) becomes

$$\dot{b} = -\langle i\tilde{p}_1 e^{-i\tilde{\theta}_0} \rangle. \tag{2.178}$$

which, using (2.171), becomes

$$\dot{b} = -iP \tag{2.179}$$

The complete set of linear ordinary differential equations can therefore be

written

$$\dot{\tilde{A}} = b + i\delta\tilde{A} \tag{2.180}$$
$$\dot{P} = -\tilde{A} \tag{2.181}$$
$$\dot{b} = -iP \tag{2.182}$$

where the collective electron variables are defined as $b \equiv -\langle i\tilde{\theta}_1 e^{-i\tilde{\theta}_0}\rangle$ and $P \equiv \langle\tilde{p}_1 e^{-i\tilde{\theta}_0}\rangle$.

2.5.3 Solution of Linear Equations for $\delta = 0$

The most simple case to analyse is the case when all the electrons are injected into the undulator at the resonant energy, so that $\delta = 0$. The equations (2.180–2.182) then reduce to the following:

$$\dot{\tilde{A}} = b \tag{2.183}$$
$$\dot{P} = -\tilde{A} \tag{2.184}$$
$$\dot{b} = -iP \tag{2.185}$$

This set of three first order equations can be converted to a single third order differential equation as follows:

$$\dot{\tilde{A}} = b \rightarrow \ddot{\tilde{A}} = \dot{b} \tag{2.186}$$
$$= -iP \tag{2.187}$$

using (2.185). Then

$$\dddot{\tilde{A}} = -i\dot{P} \tag{2.188}$$
$$\dddot{\tilde{A}} = i\tilde{A} \tag{2.189}$$

using (2.184).

A trial solution of form

$$\tilde{A}(\bar{z}) = \tilde{A}_0 e^{i\lambda\bar{z}} \tag{2.190}$$

so that $\dot{\tilde{A}} = i\lambda\tilde{A}$, $\ddot{\tilde{A}} = -\lambda^2\tilde{A}$ and $\dddot{\tilde{A}} = -i\lambda^3\tilde{A}$, can be substituted into (2.189) to

obtain the cubic dispersion relation $\lambda^3 + 1 = 0$ so that

$$\lambda = [\lambda_1, \lambda_2, \lambda_3] = \left[-1, \frac{1}{2} + \frac{i\sqrt{3}}{2}, \frac{1}{2} - \frac{i\sqrt{3}}{2}\right] \tag{2.191}$$

and the general solution is some linear combination

$$\tilde{A}(\bar{z}) = \tilde{A}_0 \sum_k c_k e^{i\lambda_k \bar{z}}. \tag{2.192}$$

A full solution to the linearised system, found by a Fourier-Laplace transform, shows that for initial conditions $\tilde{A}_0 \neq 0$, $b_0 = 0$ and $P_0 = 0$ the coefficients $c_k = 1/3 \,\forall\, k$ so that the power is distributed evenly between the three modes [39].

Figure 2.2 shows an illustrative example with initial field $\tilde{A}_0 = 10^{-4}$. The evolution of the individual terms of (2.192) are plotted. The top left panel shows the evolution with $\bar{z}$ of the real part of $(\tilde{A}_0/3)e^{i\lambda_1\bar{z}}$. This is an oscillatory term with period 2π. The top left panel shows $|(\tilde{A}_0/3)e^{i\lambda_2\bar{z}}|^2$. This is an exponentially decaying term. The bottom left panel shows $|(\tilde{A}_0/3)e^{i\lambda_2\bar{z}}|^2$ which is seen to grow exponentially and is hence the component responsible for the exponential instability in the FEL radiation power. The bottom right panel shows $|\tilde{A}|^2$ for the sum of the three components. It is seen that the FEL radiation power does not grow at all until $\bar{z} \simeq 2$. This behaviour is referred to as the initial lethargy. For $\bar{z} \geq 2$ the field grows exponentially as

$$\tilde{A}(\bar{z}) \simeq \frac{\tilde{A}_0}{3} e^{\sqrt{3}\bar{z}/2} \tag{2.193}$$

or equivalently the power grows as

$$|\tilde{A}(\bar{z})|^2 \simeq \frac{|\tilde{A}_0|^2}{9} e^{\sqrt{3}\bar{z}} \tag{2.194}$$

which is shown as the red dashed line in the bottom right panel of Figure 2.2.

The full solution of the linearised system can also be used to show the growth of the field when the instability starts from a small initial bunching $b_0 \ll 1$ with $\tilde{A}_0 = 0$ [9, 10, 39]. The evolution of $\tilde{A}$ with $\bar{z}$ converges after $\bar{z} \simeq 2$ to the case starting up from an initial field, showing that the FEL instability can start up due to electron beam shot noise without the requirement of an initial field. This

is the principle of the SASE FEL, as discussed further in Section 2.7.

In S. I. units the evolution of the power evolves with z as

$$P_{\rm rad} \propto e^{z/L_g} \tag{2.195}$$

where L_g is the e-folding power gain length. Note that (2.194) can be expressed using (2.64) as

$$|\tilde{A}(z)|^2 \propto e^{2\sqrt{3}k_w\rho z} \tag{2.196}$$

therefore comparing (2.195) and (2.196) it can be seen that the power gain length

$$L_g = \frac{1}{2\sqrt{3}\,\rho k_w} = \frac{\lambda_w}{\sqrt{3}\,4\pi\rho} = \frac{l_g}{\sqrt{3}} \tag{2.197}$$

where

$$l_g = \frac{1}{2k_w\rho} = \frac{\lambda_w}{4\pi\rho} \tag{2.198}$$

is called the 'nominal' gain length. Thus the universal scaling (2.64) is seen to be a scaling of the interaction length in units of l_g.

2.5.4 Solution of Linear Equations for $\delta \neq 0$

A similar procedure to that used in section 2.5.3 can be followed to reduce the system (2.180–2.182) to a third order ODE. Starting from (2.180),

$$\dot{\tilde{A}} - i\delta\tilde{A} - b = 0 \tag{2.199}$$

$$\therefore \dddot{\tilde{A}} - i\delta\ddot{\tilde{A}} - \ddot{b} = 0 \tag{2.200}$$

then using (2.182)

$$\dddot{\tilde{A}} - i\delta\ddot{\tilde{A}} - (-i\dot{P}) = 0 \tag{2.201}$$

then using (2.181)

$$\dddot{\tilde{A}} - i\delta\ddot{\tilde{A}} - i\tilde{A} = 0. \tag{2.202}$$

Adopting the trial solution (2.190) the following dispersion relation is easily obtained:

$$\lambda^3 - \delta\lambda^2 + 1 = 0. \tag{2.203}$$

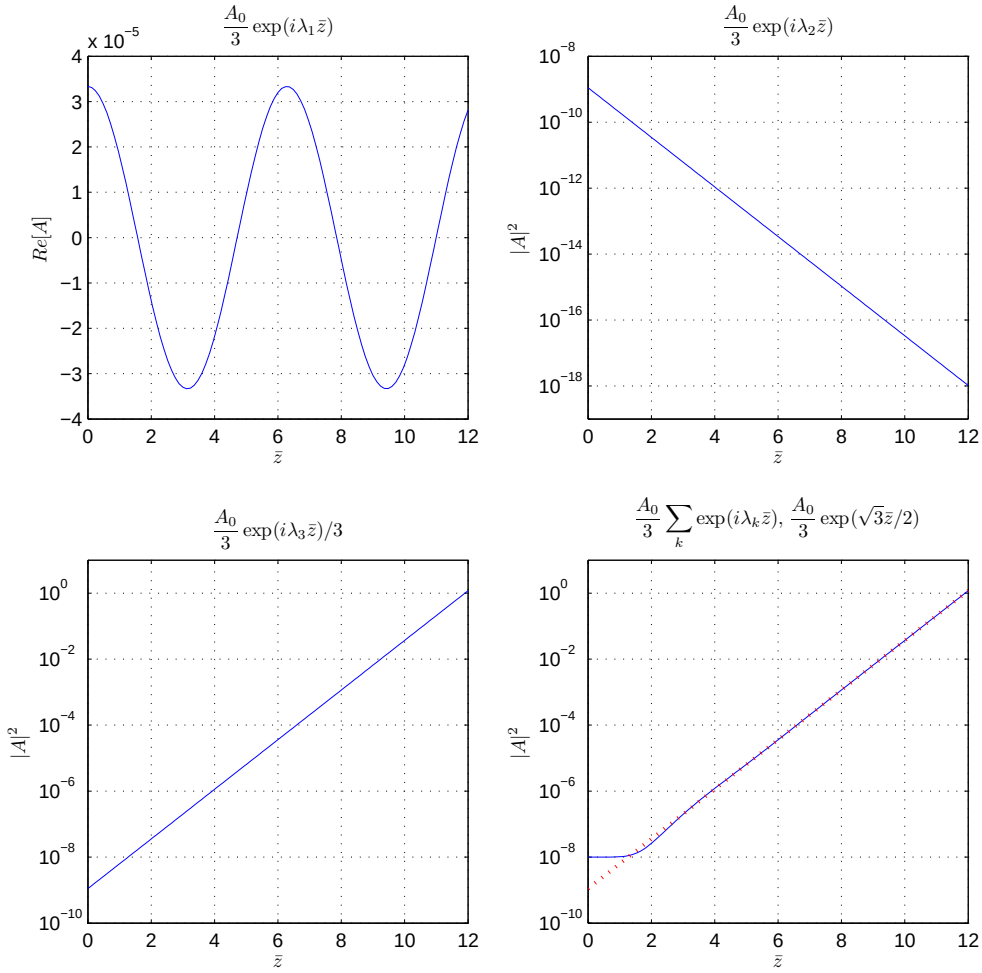

Figure 2.2: Solution of linearised equations for $\delta = 0$, $\tilde{A}_0 = 10^{-4}$. The first three panels show the individual components of Equation (2.192) with $c_k = 1/3 \,\forall\, k$. The bottom right panel shows the full solution with all components (in blue) and Equation (2.194) (in dashed red).

The nature of the roots of a cubic equation $ax^3 + bx^2 + cx + d = 0$ depends on the discriminant

$$\Delta = 18abcd - 4b^3d + b^2c^2 - 4ac^3 - 27a^2d^2 \tag{2.204}$$

which for (2.203) gives

$$\Delta = 4\delta^3 - 27. \tag{2.205}$$

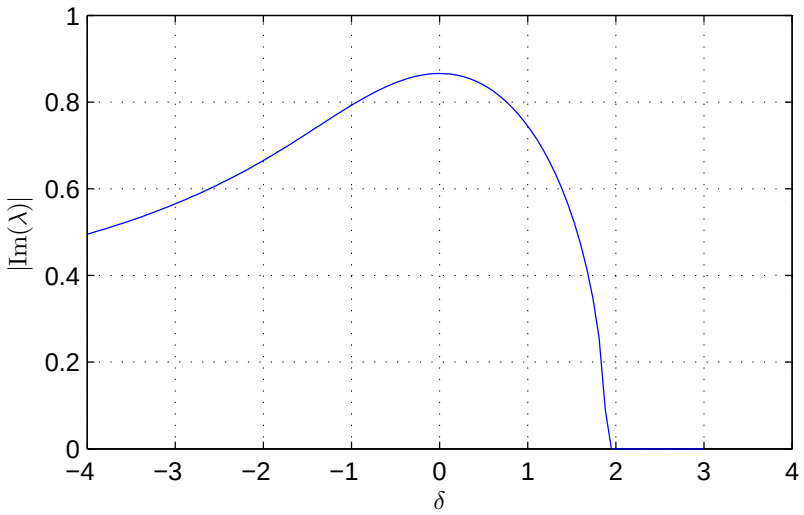

Figure 2.3: Absolute value of the imaginary part of the root of the dispersion relation (2.203) $|\mathrm{Im}(\lambda)|$, *vs* electron detuning δ.

In general, if $\Delta > 0$ then the cubic has three distinct real roots and the general solution

$$\tilde{A}(\bar{z}) = \tilde{A}_0 \sum_k c_k e^{i\lambda_k \bar{z}}. \tag{2.206}$$

comprises only oscillatory terms and there can be no exponential instability. If however $\Delta < 0$ the cubic has one real root and a pair of complex conjugate roots and the complex conjugate root with the negative imaginary component will give an exponentially increasing growth in the radiation field. For exponential gain it is therefore required that $4\delta^3 - 27 < 0$ leading to the result that the energy detuning δ must be less than the critical detuning δ_T:

$$\delta < \delta_T = \sqrt[3]{27/4} \simeq 1.89. \tag{2.207}$$

The dispersion relation (2.203) may also be solved to find the roots as a function of detuning δ. Figure 2.3 shows the absolute value of the imaginary part of the complex conjugate root, $|\mathrm{Im}(\lambda)|$, *vs* electron detuning δ. For $\delta > \delta_T \simeq 1.89$ the imaginary part of the root vanishes and there is no exponential instability, as discussed previously. The maximum growth rate is seen to be at resonance where $\delta = 0$.

2.6 FEL Output Properties

An approximate estimate of the radiation bandwidth can be made by considering the energy bandwidth of the exponential instability [37]. The electron energy detuning must be less than the critical detuning $\delta_T = 1.89$. Therefore, from (2.145),

$$\frac{1}{\rho}\frac{\Delta\gamma}{\gamma_r} \leq 1.89 \tag{2.208}$$

and from differentiating the resonance condition (2.27) the radiation bandwidth corresponding to a given energy bandwidth is

$$\left|\frac{\Delta\lambda}{\lambda_r}\right| = 2\frac{\Delta\gamma}{\gamma} \tag{2.209}$$

therefore combining (2.208) and (2.209) gives a full width

$$\left|\frac{\Delta\lambda}{\lambda_r}\right|_{\mathrm{FW}} \simeq 4\rho. \tag{2.210}$$

A more complete analysis can be done [37] by expanding the imaginary part of the root (as plotted in Figure 2.3 as a function of δ) around $\delta = 0$. This gives

$$\mathrm{Im}(\lambda) \simeq \frac{\sqrt{3}}{2}\left(1 - \frac{\delta^2}{9}\right) \tag{2.211}$$

for $|\delta| \ll \delta_T$ which, using (2.145), (2.206) and (2.209) leads to

$$|\tilde{A}(\bar{z}, \Delta\lambda/\lambda_r)|^2 \simeq \frac{|\tilde{A}(0)|^2}{9}\exp(\sqrt{3}\bar{z})\exp\left(-\frac{(\Delta\lambda/\lambda)^2}{2\sigma_\lambda^2}\right) \tag{2.212}$$

with

$$\sigma_\lambda \simeq 2\rho\sqrt{\frac{\pi}{\bar{z}}} \tag{2.213}$$

therefore the bandwidth reduces as $1/\sqrt{\bar{z}}$. Using this result, derived from the linear theory, an approximation can be made of the bandwidth at the end of the linear regime as the FEL enters saturation. This typically occurs at $\bar{z} \approx 10$ so using this value in (2.213) gives

$$\sigma_\lambda \simeq \rho \tag{2.214}$$

The linear theory gives a good description of the start-up from initial conditions and subsequent exponential field gain in the linear regime (so called because it is described by the linear equations) but does not describe the saturation of the FEL power which starts when the strongly bunched electrons start to re-absorb energy from the radiation field. This process can only be described properly through a numerical solution to the non-linearised FEL equations. It is found that in the scaled units, at saturation the field has intensity $|\tilde{A}|^2_{\rm sat} \simeq 1$ [40]. This can be shown from the set of nonlinear FEL equations (2.133-2.135) written in the steady state approximation. Multiplying (2.135) by A^* then adding the complex conjugate gives

$$A^*\frac{\mathrm{d}A}{\mathrm{d}\bar{z}} + A\frac{\mathrm{d}A^*}{\mathrm{d}\bar{z}} = A^*b + b^*A \tag{2.215}$$

$$\therefore \frac{\mathrm{d}}{\mathrm{d}\bar{z}}|A|^2 = A^*b + b^*A. \tag{2.216}$$

Now averaging (2.134),

$$\frac{\mathrm{d}\langle\bar{p}\rangle}{\mathrm{d}\bar{z}} = -\left(A\langle e^{i\theta}\rangle + A^*\langle e^{-i\theta}\rangle\right) \tag{2.217}$$

$$= -(Ab^* + A^*b) \tag{2.218}$$

so adding (2.216) and (2.218) gives

$$\frac{\mathrm{d}}{\mathrm{d}\bar{z}}\left(|A|^2+\langle\bar{p}\rangle\right) = 0 \tag{2.219}$$

therefore

$$|A|^2+\langle\bar{p}\rangle = \text{constant}. \tag{2.220}$$

This means that for a small initial field $A_0 \ll 1$ the maximum field intensity is constrained by the average change in electron energy which is of the order unity, therefore at saturation $|A|^2_{\rm sat} \simeq 1$ as before.

The scaled field can be shown to satisfy the relation

$$|\tilde{A}|^2 = \frac{1}{\rho}\frac{P_{\rm rad}}{P_{\rm beam}} \tag{2.221}$$

therefore the saturation power is

$$P_{\rm rad,\,sat} = \rho|\tilde{A}|^2_{\rm sat}P_{\rm beam} \simeq \rho P_{\rm beam} \tag{2.222}$$

since $|\tilde{A}|^2_{\rm sat} \simeq 1$. The ρ parameter thus gives the efficiency of the FEL mechanism, or the fraction of electron beam power that is converted to radiation power [40].

2.7 Output Properties of the SASE FEL

The linear analysis of the previous sections was done in the steady-state approximation. This thesis however is particularly concerned with longitudinal effects—with the generation of short pulses and the evolution of the temporal coherence within the free-electron laser (and by corollary with its spectral characteristics because these are coupled via the Fourier transform). For this reason it is necessary to understand how the radiation properties change longitudinally along the pulse. For example the temporal coherence is a function of the radiation phase and amplitude along the photon pulse—the coherence length is in fact a measure of the longitudinal delay over which the pulse can be made to interfere destructively with a copy of itself. This is how it can be determined experimentally via a Michelson Interferometer and also expressed mathematically (in the units of the universal scaling) as [41]

$$\bar{l}_{\rm coh} = \int_{-\infty}^{+\infty} |g(\bar{\tau}_1)|^2 d\bar{\tau}_1 \tag{2.223}$$

where

$$g(\bar{\tau}_1) = \frac{\langle \tilde{A}^*(\bar{z}_1)\tilde{A}(\bar{z}_1+\bar{\tau}_1)\rangle}{\langle \tilde{A}^*(\bar{z}_1)\tilde{A}(\bar{z}_1)\rangle}. \tag{2.224}$$

The coherence function has the property that $|g(0)|^2 = 1$ with $|g(\bar{\tau}_1)|^2$ exhibiting a Gaussian form, as demonstrated in Figure 2.4 which shows an example of the function for a chaotic SASE output pulse.

The evolution along the undulator of the longitudinal pulse characteristics is also strongly dependent on the relative slippage between radiation and electron bunch. Therefore to investigate the temporal and spectral properties of the SASE FEL output pulse at any distance through the undulator it is necessary to remove the constraint $\partial\tilde{A}/\partial\bar{z}_1 = 0$ and include pulse propagation. It can be shown that the linear system (2.183–2.185) can then be written as

$$\frac{\partial\tilde{A}(\bar{z},\bar{z}_1)}{\partial\bar{z}} + \frac{\partial\tilde{A}(\bar{z},\bar{z}_1)}{\partial\bar{z}_1} = b(\bar{z},\bar{z}_1) \tag{2.225}$$

$$\frac{\partial^2 b(\bar{z},\bar{z}_1)}{\partial\bar{z}^2} = iA(\bar{z},\bar{z}_1) \tag{2.226}$$

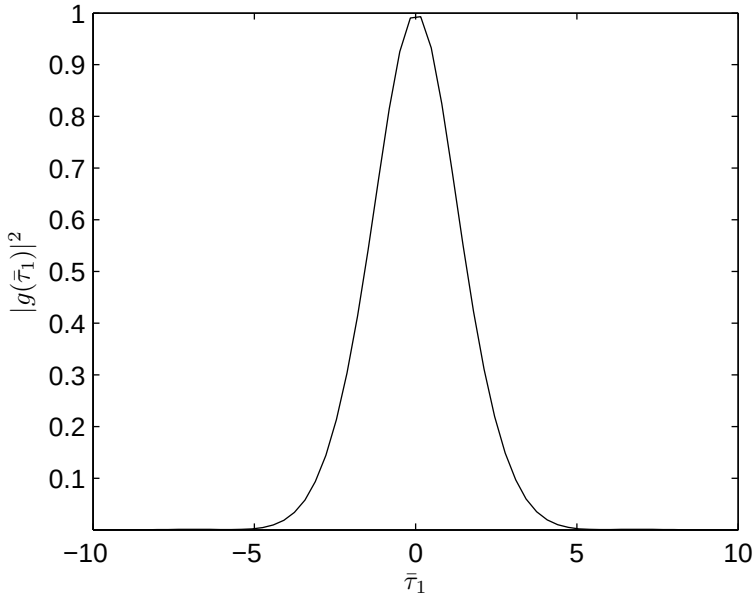

Figure 2.4: Typical calculated coherence function $|g(\bar{\tau}_1)|^2$ for a SASE pulse.

and the system can be solved to describe mathematically the onset of the FEL process from a small initial bunching $b_0(\bar{z}, \bar{z}_1)$ due to the shot noise in an electron beam injected into the undulator [11].

An important result of this analysis is that the temporal structure of the radiation pulse at saturation is a random superposition of many spikes with uncorrelated phases, with a maximum peak-to-peak distance $2\pi l_c$ where the cooperation length

$$l_c \equiv \frac{\lambda_r}{4\pi\rho}. \tag{2.227}$$

From the definition of the nominal gain length (2.198), the number of undulator periods in a gain length is

$$N_{l_g} = \frac{l_g}{\lambda_w} = \frac{1}{4\pi\rho} \tag{2.228}$$

therefore the slippage in a gain length is

$$N_{l_g}\lambda_r = \frac{\lambda_r}{4\pi\rho} \tag{2.229}$$

which from (2.227) is the cooperation length l_c. On propagating through one gain length of the undulator, a wavefront therefore propagates through the electron beam a distance l_c and the cooperation length thus defines the scale at which

collective effects evolve throughout the electron beam, and so how the temporal coherence of the radiation field evolves from the initially spontaneous noise. For a sufficiently long electron beam, different regions along the beam develop from the localised noise source autonomously and are therefore uncorrelated in phase. In this sense, the SASE process can be considered as a 'localised' collective process.

Typically, in the X-ray the electron bunch length $l_b \gg 2\pi l_c$, so the output comprises a series of many phase spikes. At saturation the SASE radiation coherence time is [42]

$$\tau_{\rm coh} \simeq \frac{1}{\rho\omega}\sqrt{\frac{\pi \ln N_c}{18}} \tag{2.230}$$

where $N_c = I/(e\rho\omega)$ with I the electron bunch current. This expression can be simplified further by noting that for a wide range of typical X-ray FELs the square root term evaluates to $\simeq 1.6$, hence the coherence length

$$l_{\rm coh} = c\tau_{\rm coh} \simeq \frac{3.2c}{2\rho\omega} = \frac{3.2c}{2\rho}\frac{\lambda}{2\pi c} = 3.2\frac{\lambda}{4\pi\rho} \tag{2.231}$$

or approximately 3.2 cooperation lengths

$$l_{coh} \simeq 3.2 l_c. \tag{2.232}$$

If however the electron bunch length $l_b \leq 2\pi l_c$ only one SASE spike can develop and single spike output is possible. Such a regime is known as weak superradiance or single-spike SASE [43, 44].

As discussed, the SASE FEL starts up from the initial shot noise in the electron beam, which results in the small initial bunching. This shot noise has a white spectrum and a thorough analysis of its statistical properties has been done [45]. It is also common to refer to an equivalent shot noise input power. This is the equivalent radiation power that would give an identical saturation length in the absence of the initial bunching. Thus, using (2.194) and (2.195) the power growth in the linear regime is given in S. I. units by

$$P_{\rm rad}(z) = \frac{P_{\rm rad}(0)}{9} e^{z/L_g} \tag{2.233}$$

and $P_{\rm rad}(0)$ is the equivalent input shot noise power given by [46]

$$P_{\rm rad}(0) = \frac{6\sqrt{\pi}}{N_\lambda \sqrt{\ln(N_\lambda/\rho)}}\ \rho^2 P_{beam} \tag{2.234}$$

with N_λ the number of electrons within an optical period.

2.7.1 A Typical SASE Output Pulse

A simulation of a typical SASE output pulse at saturation is shown in Figure 2.5. The electron bunch has a Gaussian current profile. The top plot shows scaled radiation power $|A|^2$ *vs* $\bar{z}_1$, radiation phase ϕ *vs* $\bar{z}_1$ and spectrum obtained from the Fourier transform of the complex radiation envelope. The scaled frequency $\bar{\omega}$ is defined

$$\bar{\omega} = \frac{1}{2\rho}\frac{\omega - \omega_r}{\omega_r} = \frac{1}{2\rho}\frac{\lambda_r - \lambda}{\lambda_r}. \tag{2.235}$$

The bottom plot shows an inset of the same pulse, with the peaks of the SASE spikes marked in red dots. Green dots mark the corresponding radiation phases ϕ. It is clearly seen here that the SASE pulse is a series of spikes of uncorrelated phases. The average spacing between the spikes in the inset is $\Delta s = 6.5$ in units of $\bar{z}_1$. In this scaling unity represents one cooperation length l_c so the average spike spacing is very close to the theoretical $\Delta s = 2\pi l_c$. The full spectral width is $|\Delta\bar{\omega}|_{\rm FW} \simeq 2$. From (2.235)

$$\frac{\Delta\lambda}{\lambda_r} = 2\rho\bar{\omega} \tag{2.236}$$

therefore for the pulse shown $(\Delta\lambda/\lambda_r)_{\rm FW} \simeq 4\rho$ in agreement with (2.210) and similarly $|\Delta\bar{\omega}|_{\rm FWHM} \simeq 1$ giving $(\Delta\lambda/\lambda_r)_{\rm FWHM} \simeq 2\rho$.

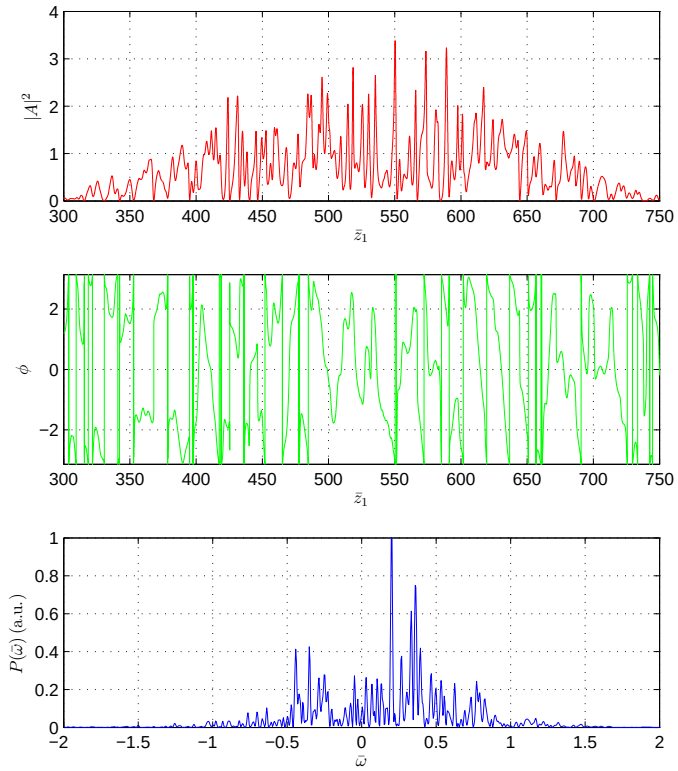

(a)

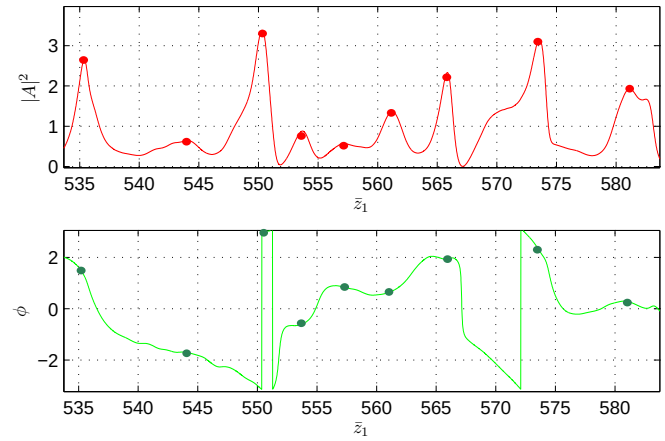

(b)

Figure 2.5: Typical SASE output in scaled units. (a) Scaled power $|A|^2$ and radiation phase ϕ vs position $\bar{z}_1$ and normalised spectral power $P(\bar{\omega})$ vs scaled frequency $\bar{\omega}$. (b) Scaled power and phase for an enlarged section of the pulse, with the peaks of the SASE spikes marked in red dots and the corresponding radiation phases ϕ marked in green dots.

Chapter 3

High-Brightness SASE

3.1 Introduction

The original aim of the work presented in this thesis was to explore alternatives to existing schemes for the improvement of longitudinal coherence in SASE FELs. As discussed in the previous chapter the development of longitudinal coherence in the SASE FEL is driven by the relative slippage between radiation and electron bunch. The temporal spikes in the FEL output are individually longitudinally coherent. The SASE coherence length is about half the spike spacing, because $l_{\mathrm{coh}} \simeq 3l_c$ and the spike spacing $\Delta s \simeq 2\pi l_c$. Each SASE spike has evolved independently with the coherence length dependent on the slippage—there is no causal mechanism to establish a common radiation and bunching phase between regions of the system separated by $\gg l_c$.

The proposal was therefore very simple: *if the slippage is enhanced artificially it may be possible to extend the radiation coherence length.* As it is not practical to change the velocity of light the only option is to slow down the electrons. The mechanism for this was inspired by an earlier proposal to stimulate harmonic lasing in an FEL amplifier by introducing regular phase shifts between electron bunch and co-propagating radiation using a series of small electron beam delay chicanes inserted between the sub-sections (or modules) of a long FEL undulator [30]. In this scheme the required delay s was sub-wavelength, $s \leq \lambda_r$, and could in fact be provided by the standard phase shifters included between modules of some FEL amplifiers for phase-matching, which is the process of compensating for the phase drift between electron bunch and radiation that would otherwise occur in the gap due to the fact that the electron velocity $v < c$. To improve

the coherence much stronger chicanes would be required in order to delay the electron bunch $s \gg \lambda_r$.

3.2 Numerical Implementation

The scheme was modelled using a one-dimensional FEL code which was adapted from a code FELO which was originally written to model oscillator FELs [47]. The code solves the Equations (2.133–2.135) by numerically integrating the system with the standard 4th order Runge-Kutta method. After each undulator period the field is shifted forward in $\bar{z}_1$ with respect to the electrons by one wavelength. This process continues until the end of one undulator module. In the original FELO code the field was then shifted longitudinally again (in $\pm\bar{z}_1$) to account for the appropriate detuning (lengthening or shortening with respect to the synchronous value) of the FEL cavity length, before the amplitude was scaled to account for cavity losses and outcoupling and a new electron bunch was created. In the revised code the field amplitude remains unchanged and the electron bunch is retained, but the field is shifted longitudinally forward with respect to the electron bunch to represent the relative delay given to the electrons.

The chicanes delay the electrons due to the extra path length compared to the radiation. The simplest configuration for such a chicane is a series of four dipole magnets with on-axis field B with magnetic length L_B, separated by drift lengths L_D. The path length for an electron in such a chicane depends on the electron energy, as more energetic particles are deflected less and follow a shorter path. This effect is referred to as longitudinal dispersion and is parameterised by the R_{56} term of the linear transfer matrix for the chicane which is defined as

$$R_{56} = \int \frac{\eta(s)}{\rho_c}\,\mathrm{d}s \tag{3.1}$$

where η is the dispersion, ρ_c is the bend radius and s is the longitudinal coordinate along the trajectory of the reference electron. In the universally scaled system the longitudinal dispersion of the chicane is parameterised via the $\bar{D}$ parameter [40][1] and the dispersive effect is applied to the particle phase using the mapping

$$\theta_i \to \theta_i + \bar{D}\bar{p}_i. \tag{3.2}$$

[1]Note the parameter is notated D without bar in [40].

The $\bar{D}$ parameter is related to R_{56} by

$$\bar{D} = \frac{2\pi\rho}{\lambda_r} R_{56}. \tag{3.3}$$

The R_{56} term for the specific case of a four-dipole chicane of equal dipole and drift lengths, $L_B = L_D = L$, is given for small deflection angle θ by

$$R_{56} = \frac{10}{3} L\theta^2. \tag{3.4}$$

The delay δ due to the chicane can be shown by simple geometry to be

$$\delta = \frac{5}{3} L\theta^2 \tag{3.5}$$

for small θ. Equations (3.3-3.5), combined with the conversion of δ into $\bar{z}_1$ units enable the dispersion parameter $\bar{D}$ for a 4-dipole chicane to be expressed in terms of the delay $\bar{\delta}_1$ as

$$\bar{D} = \bar{\delta}_1. \tag{3.6}$$

This enables the dispersive effect appropriate to the delay to be conveniently applied in the code via the mapping of equation (3.2).

In order to model more complex chicanes with variable longitudinal dispersion, a scaled dispersion parameter D is introduced,

$$D = \frac{\bar{D}}{(5\bar{\delta}_1/3)}. \tag{3.7}$$

D is therefore $\bar{D}$ rescaled relative to 5/3 times the dispersion in a standard four-dipole chicane, so that for a four-dipole chicane $D = 0.6$ and for a true isochronous chicane where the longitudinal dispersion is zero, $D = 0$.

In the universal scaling of the simulation code, the delay imparted by the chicane is notated $\bar{\delta}_1$. The slippage in the undulator, of length $\bar{l}$, is notated $\bar{l}_1$ and it is noted that because of the relative scalings of the two frames of reference, $\bar{l}$ is numerically equal to $\bar{l}_1$. The total slippage between electrons and radiation, in one undulator module and one chicane, is therefore

$$\bar{s}_1 = \bar{l}_1 + \bar{\delta}_1. \tag{3.8}$$

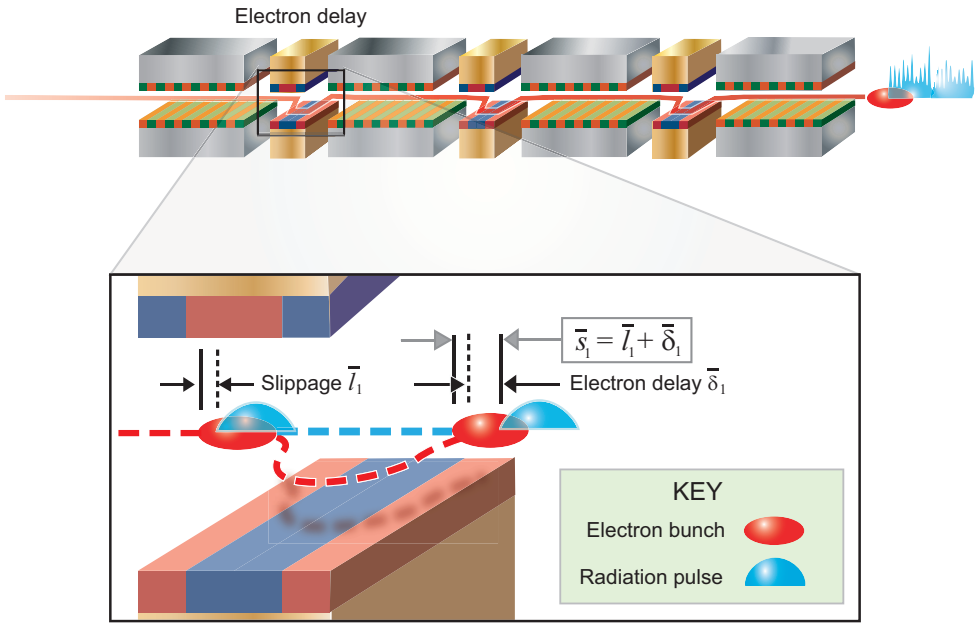

Figure 3.1: Schematic representation of the High Brightness SASE system. Chicanes are introduced between the undulator modules to delay the electron bunch with respect to the co-propagating radiation pulse.

It also useful to define a slippage enhancement factor

$$S_e \equiv \frac{\bar{s}_1}{\bar{l}_1} \tag{3.9}$$

to parameterise the system. For conventional SASE, where the delay $\bar{\delta}_1 = 0$, it is seen from (3.8) and (3.9) that $S_e = 1$.

The system is shown schematically in Figure 3.1. It should be noted that the delay chicane is represented here by four dipoles—more complex magnetic systems would be needed to implement delays with a reduced R_{56} [48, 49].

3.3 First Numerical Results

The first published simulations [50] used the following parameters: the undulator module length was $\bar{l} = 0.5$, with electron bunch length $\bar{l}_b = 250$. The delays were set to be isochronous, so $D = 0$, and slippage enhancement from $S_e = 1$ to $S_e = 4$ was used. Figure 3.2 shows the pulses and spectra at saturation for increasing S_e. The features observed are as follows:

- As S_e increases the spacing of the SASE spikes increases.

- As S_e increases the radiation bandwidth around the resonance at $\bar{\omega} = 0$ decreases.
- For $S_e \geq 2.0$ a small scale modulation is visible on the radiation envelope, and this becomes more pronounced as S_e increases.
- For $S_e \geq 2.5$ sidebands are observed in the spectra, and as S_e increases these sidebands occur at frequencies closer to $\bar{\omega} = 0$.

Clearly the technique appears to have the desired effect, as indicated by the reduction in bandwidth as S_e increases. Figure 3.3 (left) shows Δs, the mean distance between the SASE *envelope* spikes as a function of S_e (red squares), indicating good agreement with the function $\Delta s = 2\pi l_c S_e$ (black dotted line). Figure 3.3 (right) shows the full radiation bandwidth around $\bar{\omega}$, *ignoring the sidebands*, normalised to the bandwidth for the $S_e = 1$ case, as a function of S_e. Here the black dashed line represents the function $\Delta\bar{\omega}/\Delta\bar{\omega}_{S_e=1} = 1/S_e$. The important results demonstrated here are therefore

- The SASE spike spacing is proportional to S_e.
- The bandwidth *around resonance* is inversely proportionally to S_e.

The unexpected results seen here were the appearance of the modulation in the SASE envelope and the sideband frequencies. In the chronology of the research undertaken for this thesis, further investigation of these phenomena led to the development of the Mode-Locked Amplifier FEL, which is the subject of Chapter 4. However some of the insight gained in this process is now applied anachronistically to develop further the concept of High-Brightness SASE, which is the subject of this chapter.

In the next section a simple numerical experiment is presented which can be used to understand the appearance of the modulations in the SASE envelope.

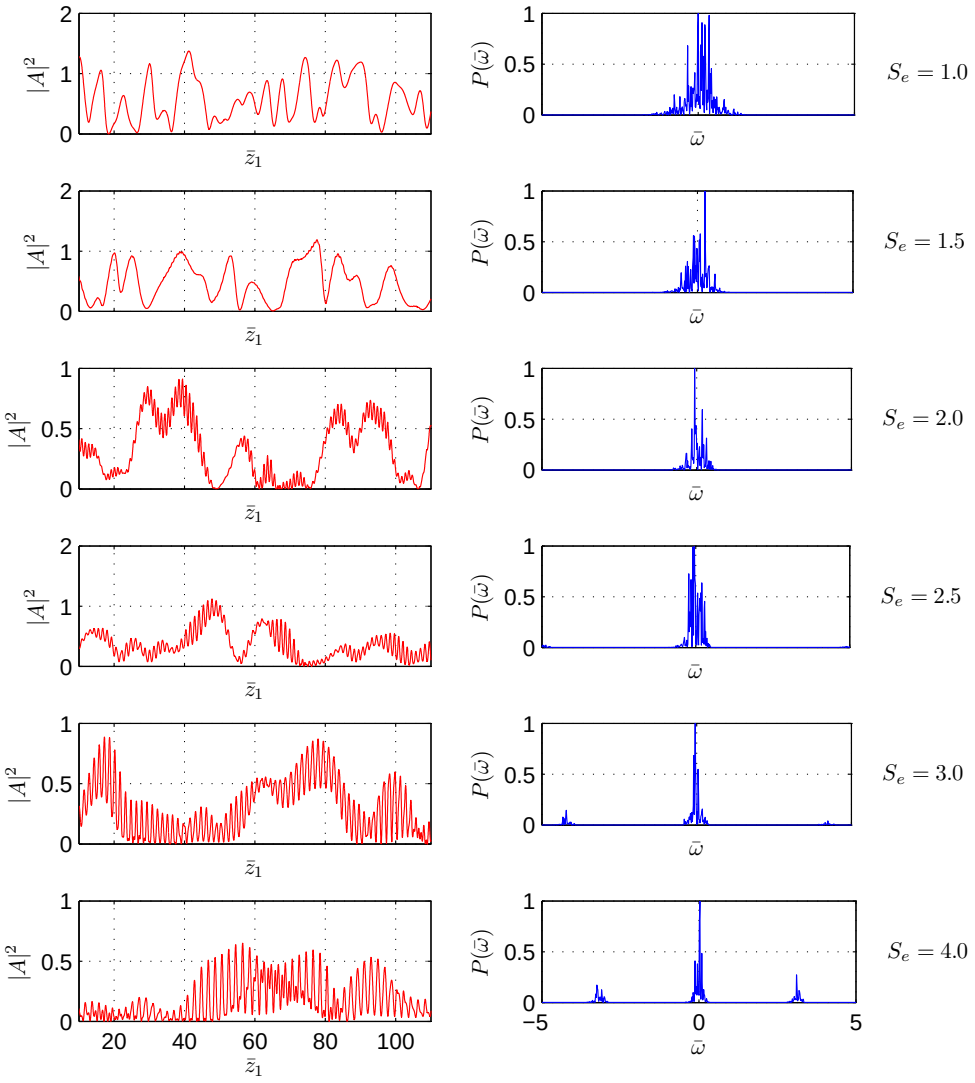

Figure 3.2: Pulse profiles of scaled power $|A|^2$ *vs* position $\bar{z}_1$ and normalised spectra $P(\bar{\omega})$ *vs* scaled frequency $\bar{\omega}$.

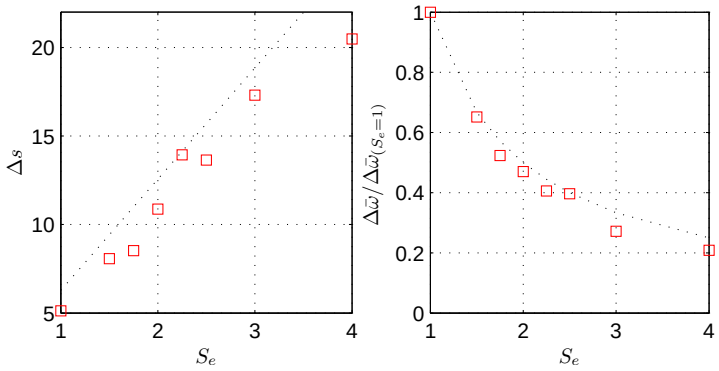

Figure 3.3: Spacing of SASE spikes Δs *vs* slippage enhancement factor S_e, and full bandwidth around resonance $\Delta\bar{\omega}$ normalised to $\Delta\bar{\omega}$ at $S_e = 1.0$.

3.4 A Numerical Experiment with Random Numbers

As an illustrative aside, we consider in this section a simple numerical experiment which gives insight to the unexpected observations (at least to the author) made in the previous section. We start with a sequence A of N random numbers uniformly distributed between 0 and 1:

$$A = [A_1, A_2, A_3, \ldots, A_N] \quad A_p \in [0, 1] \; \forall \, p. \tag{3.10}$$

We now make a copy A' of the sequence A, circularly shift all the elements in this A' by some amount $s \ll N$, so that $A_p \to A_{p+s}$, then add A' to the original sequence A. This process is performed X times and then the resulting sequence renormalised so that $\sum_{p=1}^{N} A_p$ is unchanged from its initial value.

We then examine the new sequence. One would expect that as we have simply taken a list of random numbers, shifted it and added it to itself a few times we would still have a list of random numbers. Anecdotally, this is what most people think if you ask them this question. However, *this is not the case*. What is observed is that there is now a *periodic modulation* in the values of the elements in the sequence. Out of noise, some order has been created.

An example of this numerical experiment is shown in Figure 3.4. The top row, in red, shows (left to right) the original sequence A, an FFT of the sequence to examine any periodicity, and a histogram of the values of A. The sequence used has 400 elements, but for easier visibility only the first 100 elements are shown. It is clear that the number sequence looks random with no evidence of dominant periodicity. The manipulations described above are then applied, with $s = 10$ and $X = 20$, and the results shown on the bottom row, in blue. There is an obvious modulation with period $\tau = 10$. This is picked out clearly in the FFT. It is also seen that there are modulations with period $\tau = s/2, s/3, \ldots$. Figure 3.5 shows the FFT expressed in terms of frequency $\nu = 1/\tau$. The periodic modulation in the sequence is seen to correspond to a set of frequencies equally spaced by $\Delta\nu = 1/s$.

This numerical example is analogous to the FEL system described so far. The random number sequence would represent the noisy spontaneous emission from the electron bunch in a single undulator module. In the chicane, the electron

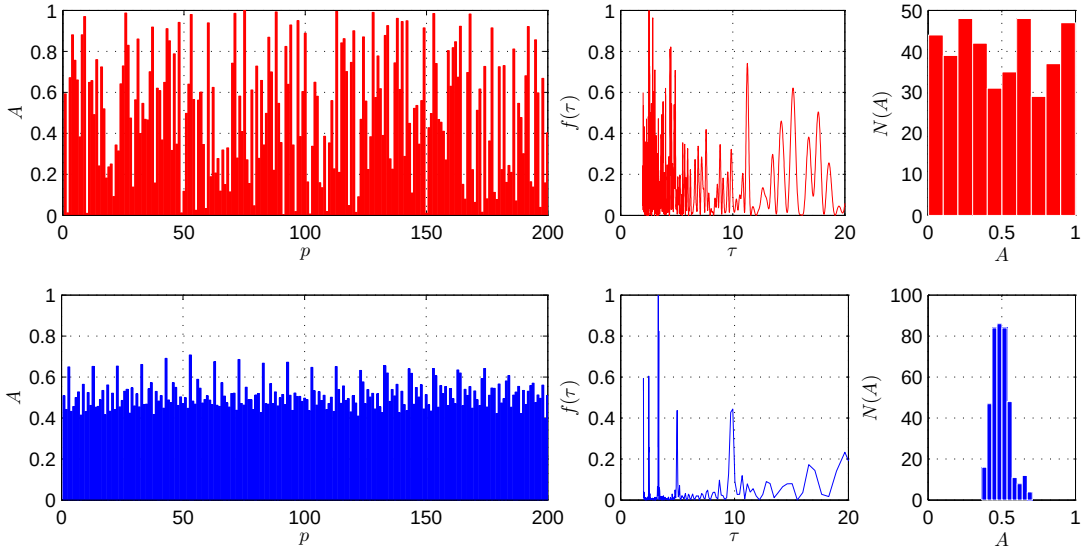

Figure 3.4: A numerical experiment with shifting, copying and adding random numbers. Top: the original random sequence, FFT and histogram. Bottom: the new sequence.

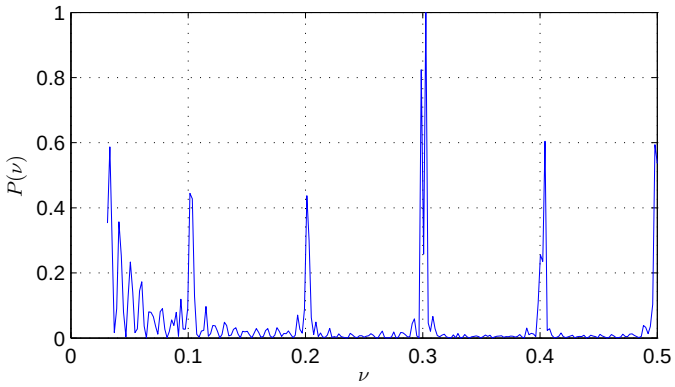

Figure 3.5: A numerical experiment: frequency spectrum of the new sequence.

beam is delayed by s, then re-emits another pulse of spontaneous emission which is shifted in time relative to, and overlays, the emission from the first undulator module. Because each undulator module is short, the shot noise structure in the electron bunch is not changed very much by propagation or emission, so the emitted field from the second undulator module is similar to the pulse emitted in the first undulator module. In this way, the total field comprises a sequence of similar, but shifted, noisy spontaneous emission pulses and has temporal and spectral properties analagous to the simple numerical example presented here— a

modulation of the envelope with period s and a frequency spectrum with sideband frequencies evenly spaced by $1/s$.

In the next section a proper mathematical model of this process is given by deriving the spontaneous emission spectrum of the FEL system with equal delays.

3.5 Theoretical Model Spectra

3.5.1 Spontaneous Emission Spectrum

It is possible to derive a simple expression for the spontaneous spectrum, i.e. in the absence of FEL gain, by considering the emission due to a small source term. Equation (2.135) can be simplified to

$$\frac{\partial A}{\partial \bar{z}} + \frac{\partial A}{\partial \bar{z}_1} = b_0(\bar{z}_1) \tag{3.11}$$

by assuming a constant current and a source term $b_0(\bar{z}_1)$ that does not evolve with $\bar{z}$. Taking the Fourier transform with respect to $\bar{z}_1$,

$$\mathbb{F}\left[X(\bar{z},\bar{z}_1)\right] \equiv \tilde{X}(\bar{z},\bar{\omega}) = \frac{1}{\sqrt{2\pi}} \int_{-\infty}^{\infty} X(\bar{z},\bar{z}_1) e^{-i\bar{\omega}\bar{z}_1} \mathrm{d}\bar{z}_1 \tag{3.12}$$

and using the Fourier transform property

$$\mathbb{F}\left[\frac{\mathrm{d}X(\bar{z},\bar{z}_1)}{\mathrm{d}\bar{z}_1}\right] = i\bar{\omega}\tilde{X}(\bar{z},\bar{\omega}) \tag{3.13}$$

gives

$$\frac{\mathrm{d}\tilde{A}}{\mathrm{d}\bar{z}} + i\bar{\omega}\tilde{A} = \tilde{b} \tag{3.14}$$

where dependence on $\bar{\omega}$ and $\bar{z}$ is assumed. The transform variable $\bar{\omega}$ is a scaled frequency defined earlier in (2.235). Multiplying both sides of this equation by $e^{i\bar{\omega}\bar{z}}$ gives

$$\frac{\mathrm{d}\tilde{A}}{\mathrm{d}\bar{z}} e^{i\bar{\omega}\bar{z}} + i\bar{\omega}\tilde{A}e^{i\bar{\omega}\bar{z}} = \tilde{b}e^{i\bar{\omega}\bar{z}} \tag{3.15}$$

the LHS of which is simply the differential of the product $\tilde{A}e^{i\bar{\omega}\bar{z}}$ so

$$\frac{\mathrm{d}}{\mathrm{d}\bar{z}}\left(\tilde{A}e^{i\bar{\omega}\bar{z}}\right) = \tilde{b}e^{i\bar{\omega}\bar{z}} \tag{3.16}$$

which can be integrated to give

$$\tilde{A}e^{i\bar{\omega}z} = \frac{\tilde{b}}{i\bar{\omega}}e^{i\bar{\omega}z} + C \tag{3.17}$$

and hence

$$\tilde{A} = \frac{\tilde{b}}{i\bar{\omega}} + Ce^{-i\bar{\omega}z}. \tag{3.18}$$

With intitial condition $\tilde{A}(0) = 0$ the integration constant is found to be

$$C = -\frac{\tilde{b}}{i\bar{\omega}} \tag{3.19}$$

so the general solution is

$$\tilde{A} = \frac{\tilde{b}}{i\bar{\omega}}\left(1 - e^{-i\bar{\omega}\bar{z}}\right). \tag{3.20}$$

Multiplying the first term by $e^{-i\bar{\omega}\bar{z}/2}$ and the terms in the brackets by $e^{i\bar{\omega}\bar{z}/2}$ gives

$$\begin{aligned}
\tilde{A} &= \frac{2\tilde{b}}{\bar{\omega}}e^{-i\bar{\omega}\bar{z}/2}\left(\frac{e^{i\bar{\omega}\bar{z}/2} - e^{-i\bar{\omega}\bar{z}/2}}{2i}\right) && (3.21)\\
&= \frac{2\tilde{b}}{\bar{\omega}}e^{-i\bar{\omega}\bar{z}/2}\sin\left(\frac{\bar{\omega}\bar{z}}{2}\right) && (3.22)\\
&= \frac{\tilde{b}\bar{z}}{(\bar{\omega}\bar{z}/2)}e^{-i\bar{\omega}\bar{z}/2}\sin\left(\frac{\bar{\omega}\bar{z}}{2}\right) && (3.23)\\
&= \tilde{b}\bar{z}e^{-i\bar{\omega}\bar{z}/2}\mathrm{sinc}\left(\frac{\bar{\omega}\bar{z}}{2}\right). && (3.24)
\end{aligned}$$

For a single undulator of length $\bar{l}$ the spectrum is therefore

$$\tilde{A}(\bar{\omega}) = \tilde{b}\bar{l}e^{-i\bar{\omega}\bar{l}/2}\mathrm{sinc}\left(\frac{\bar{\omega}\bar{l}}{2}\right). \tag{3.25}$$

In the frame of reference of the electrons, by the end of the undulator chain the total field will comprise the field from the last module, added to the field from the penultimate module but shifted by $\bar{s}_1$, plus the field from the module before that, but shifted by $2\bar{s}_1$, and so on. With A_m the field from a single undulator module, the total field due to the sum of N modules is

$$A(\bar{z},\bar{z}_1) = A_m + A_m(\bar{z},\bar{z}_1 - \bar{s}_1) + A_m(\bar{z},\bar{z}_1 - 2\bar{s}_1)\cdots + A_m(\bar{z},\bar{z}_1 - (N-1)\bar{s}_1). \tag{3.26}$$

Using the Fourier transform time-shifting relation

$$\mathbb{F}\left[X(\bar{z},\bar{z}_1-a)\right]=e^{-ia\bar{\omega}}\tilde{X}(\bar{z},\bar{\omega}) \tag{3.27}$$

the transform of the total field $A(\bar{z},\bar{z}_1)$ is

$$\begin{aligned}\tilde{A} &= \tilde{A}_m+e^{-i\bar{\omega}\bar{s}_1}\tilde{A}_m+e^{-i\bar{\omega}2\bar{s}_1}\tilde{A}_m+\ldots+e^{-i\bar{\omega}(N-1)\bar{s}_1}\tilde{A}_m &(3.28)\\ &= \tilde{A}_m\left(1+e^{-i\bar{\omega}\bar{s}_1}+e^{-i\bar{\omega}2\bar{s}_1}+\ldots+e^{-i\bar{\omega}(N-1)\bar{s}_1}\right) &(3.29)\\ &= \tilde{A}_m\left(\frac{1-e^{-i\bar{\omega}N\bar{s}_1}}{1-e^{-i\bar{\omega}\bar{s}_1}}\right) &(3.30)\end{aligned}$$

where in the final step the standard expression for the sum of a geometric series has been applied. Substituting from (3.25), the spontaneous emission spectrum is therefore

$$\tilde{A}(\bar{\omega})=\tilde{b}\bar{l}\mathrm{sinc}\left(\frac{\bar{\omega}\bar{l}}{2}\right)e^{-i\bar{\omega}\bar{l}/2}\left(\frac{1-e^{-i\bar{\omega}N\bar{s}_1}}{1-e^{-i\bar{\omega}\bar{s}_1}}\right) \tag{3.31}$$

and the power spectral density

$$\begin{aligned}|\tilde{A}(\bar{\omega})|^2 &= |\tilde{b}|^2\bar{l}^2\mathrm{sinc}^2\left(\frac{\bar{\omega}\bar{l}}{2}\right)\frac{2-(e^{i\bar{\omega}N\bar{s}_1}+e^{-i\bar{\omega}N\bar{s}_1})}{2-(e^{i\bar{\omega}\bar{s}_1}+e^{-i\bar{\omega}\bar{s}_1})} &(3.32)\\ &= |\tilde{b}|^2\bar{l}^2\mathrm{sinc}^2\left(\frac{\bar{\omega}\bar{l}}{2}\right)\frac{1-\cos(N\bar{\omega}\bar{s}_1)}{1-\cos(\bar{\omega}\bar{s}_1)}. &(3.33)\end{aligned}$$

which is the single undulator module spontaneous emission spectrum multiplied by an 'interference' term responsible for the sidebands observed in the spectra of the simulation results. The normalised function (3.33) is plotted in Figure 3.6 for parameters $\bar{l}=0.5$, $\bar{s}_1=2.0$ and $N=5$. In this figure the dotted green line shows the interference term, normalised to peak value unity. The red dashed line shows the normalised sinc^2 term and the solid black line shows the normalised full function.

The Sinc^2 Term

The sinc^2 term reaches its first minimum away from $\bar{\omega}=0$ when $\bar{\omega}\bar{l}/2=\pm\pi$ or when $\bar{\omega}=\pm 2\pi/\bar{l}$ so for the example plotted in Figure 3.6 this occurs at $\bar{\omega}=\pm 4\pi$. The full bandwidth is thus $\Delta\bar{\omega}=4\pi/\bar{l}$. This can be converted into non-scaled

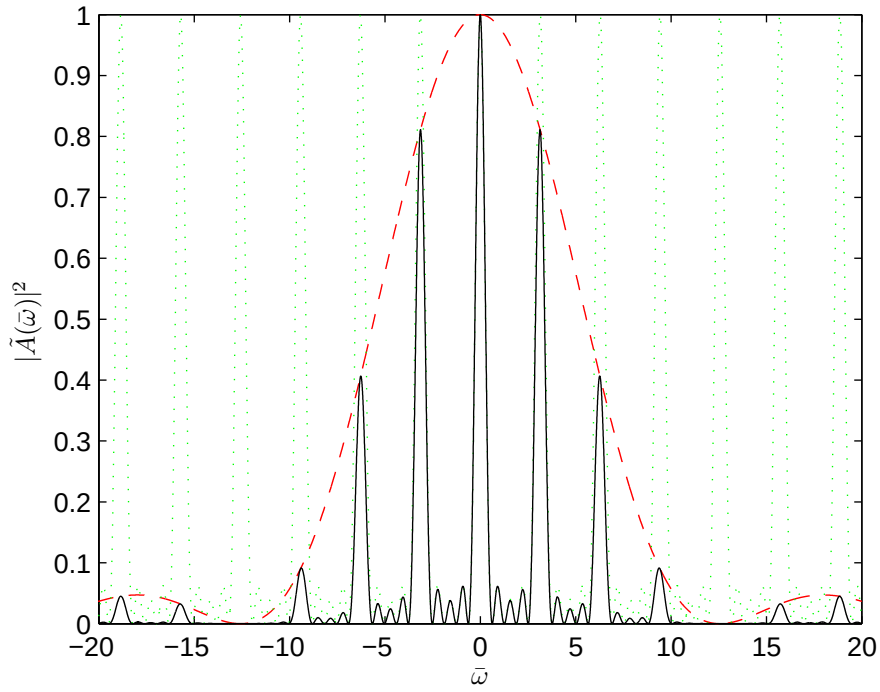

Figure 3.6: Normalised spontaneous emission spectrum (3.33) for parameters $\bar{l} = 0.5$, $\bar{s}_1 = 2.0$ and $N = 5$.

units

$$\Delta\bar{\omega} = \frac{4\pi}{\bar{l}} \tag{3.34}$$

$$\therefore \frac{1}{2\rho}\frac{\Delta\lambda}{\lambda} = 4\pi\frac{l_g}{L_w} = 4\pi\frac{\lambda_w}{4\pi\rho L_w} \tag{3.35}$$

$$\frac{\Delta\lambda}{\lambda} = \frac{2}{N_w} \tag{3.36}$$

so the FWHM bandwidth for the single undulator module is in agreement with the normal expression

$$\left|\frac{\Delta\lambda}{\lambda}\right|_{\text{FWHM}} \simeq \frac{1}{N_w}. \tag{3.37}$$

The Interference Term

The interference term is most easy to interpret by looking at the equation for the field rather than the intensity. The numerator is a phasor of amplitude unity rotating in the complex plane around +1 and the denominator is a phasor of amplitude unity rotating in the complex plane N times more slowly around +1.

The peak of the interference term corresponds to the denominator tending to zero, which will happen whenever $e^{-i\bar{\omega}\bar{s}_1} = 1$, giving the frequencies of the sidebands to be

$$\bar{\omega} = \frac{2\pi n}{\bar{s}_1} \tag{3.38}$$

with n an integer, and the spacing of the sidebands is therefore

$$\Delta\bar{\omega} = \frac{2\pi}{\bar{s}_1}. \tag{3.39}$$

For the example shown in Figure 3.6 this gives $\Delta\bar{\omega} = \pi$. Destructive interference will occur whenever the numerator is zero, which occurs whenever $e^{-iN\bar{\omega}\bar{s}_1} = 1$ giving destructive interference at

$$\bar{\omega} = \pm\frac{2\pi n}{N\bar{s}_1}. \tag{3.40}$$

The exception to this is the case $\bar{\omega} = 0$ because here the interference term is undetermined. Examination of the term

$$\frac{1 - \cos(N\bar{\omega}\bar{s}_1)}{1 - \cos(\bar{\omega}\bar{s}_1)} \tag{3.41}$$

in the intensity spectrum (3.33) shows that this is also undetermined at $\bar{\omega} = 0$ but it can be shown using using L'Hopital's rule that it tends to N^2 as $\bar{\omega} \to 0$, indicating that $\bar{\omega} = 0$ corresponds to constructive interference, not destructive.

The number of sidebands N_s is approximately the full width of the sinc function divided by the mode spacing,

$$N_s \simeq \frac{4\pi/\bar{l}}{2\pi/\bar{s}_1} = \frac{2\bar{s}_1}{\bar{l}} = 2S_e \tag{3.42}$$

The dependence of the full spectrum function on the length of the undulator module $\bar{l}$, the number of modules N and the slippage enhancement $S_e = \bar{s}_1/\bar{l}$ is shown in Figure 3.7, where $N = 2$, and Figure 3.8, where $N = 8$. From these two figures a number of observations can be made:

- For $S_e = 1$, there are no sidebands and the spectrum is the normal undulator spectrum. The width of this spectrum depends only on the total propagation distance through the undulator system $\bar{z} = N\bar{l}$. For example, for $N = 2$, $\bar{l} = 2$ the spectrum is identical to that for $N = 8$, $\bar{l} = 0.5$,

because in each case $\bar{z} = 4$.

- For $S_e > 1$, and for a fixed S_e, as $\bar{l}$ increases the sinc^2 envelope decreases as does the sideband spacing and the width of the individual sidebands.
- For $S_e > 1$, and for a fixed S_e, as N increases the sinc^2 remains constant as does the sideband spacing, but the width of the individual sidebands decreases.
- For fixed $\bar{l}$, as S_e increases the sideband spacing decreases and therefore the number of sidebands within the envelope increases. The width of each sideband also decreases.

From the above, it appears that in order to minimise the spectral width about resonance, thus providing the potential to improve the longitudinal coherence, it is necessary to increase the slippage enhancement as much as possible. Of course, this analysis is based only on an examination of the spontaneous emission spectrum, in the absence of any FEL gain. In the next section, the derivation of the spontaneous emission spectrum is amended to include a simple frequency-independent field gain term.

3.5.2 Emission Spectrum with Gain Term

A simple frequency-independent gain term can be included to investigate the effect of field amplification. The field amplification in a single undulator module can be represented by e^{α}, with α an arbitrary gain coeeficient, so the transform of the total field (3.28) can be rewritten

$$\tilde{A} = \tilde{A}_m + e^{\alpha}e^{-i\bar{\omega}\bar{s}_1}\tilde{A}_m + e^{2\alpha}e^{-i\bar{\omega}2\bar{s}_1}\tilde{A}_m + \ldots + e^{(N-1)\alpha}e^{-i\bar{\omega}(N-1)\bar{s}_1}\tilde{A}_m \qquad (3.43)$$

and following through the same steps as before the spectrum is found to be

$$\tilde{A} = \tilde{b}\bar{l}\mathrm{sinc}\left(\frac{\bar{\omega}\bar{z}}{2}\right)\left(\frac{1 - e^{-i\bar{\omega}N\bar{s}_1}e^{N\alpha}}{1 - e^{-i\bar{\omega}\bar{s}_1}e^{\alpha}}\right)e^{-i\bar{\omega}\bar{l}/2} \qquad (3.44)$$

with power spectral density

$$|\tilde{A}(\bar{\omega}, \alpha)|^2 = |\tilde{b}|^2\bar{l}^2\mathrm{sinc}^2\left(\frac{\bar{\omega}\bar{l}}{2}\right)\frac{1 + e^{2N\alpha} - 2e^{N\alpha}\cos(N\bar{\omega}\bar{s}_1)}{1 + e^{2\alpha} - 2e^{\alpha}\cos(\bar{\omega}\bar{s}_1)} \qquad (3.45)$$

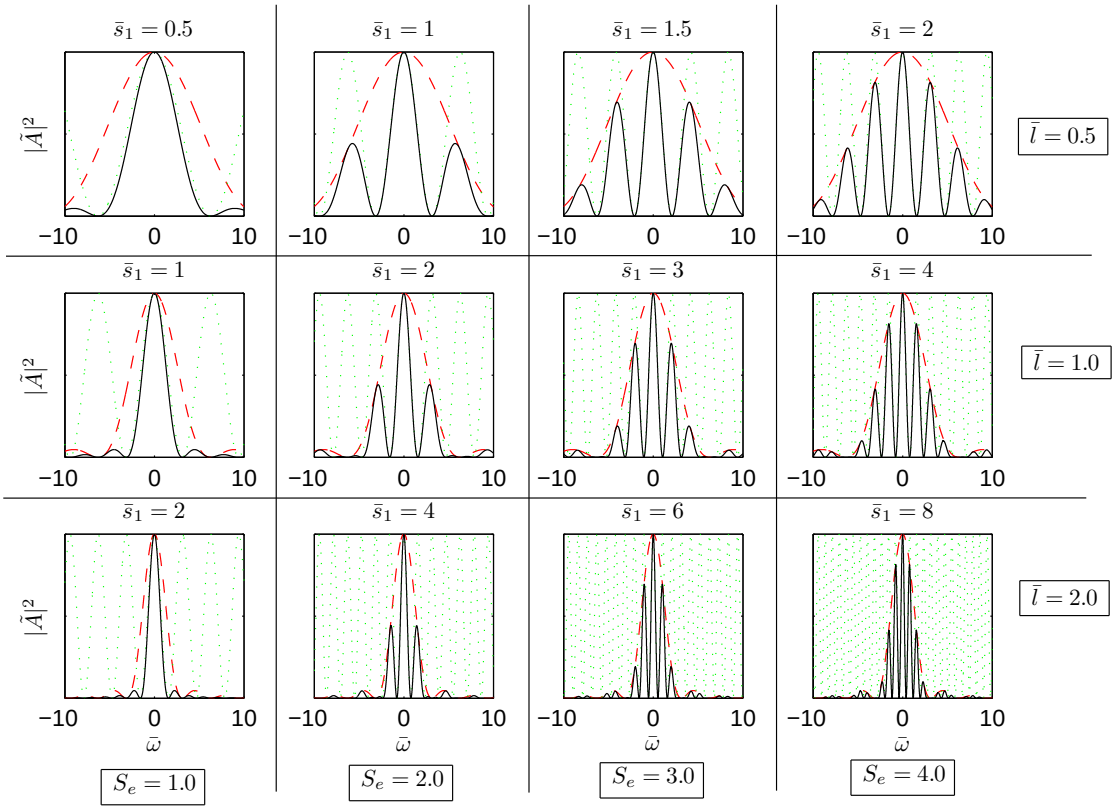

Figure 3.7: Spontaneous emission spectra, $N = 2$.

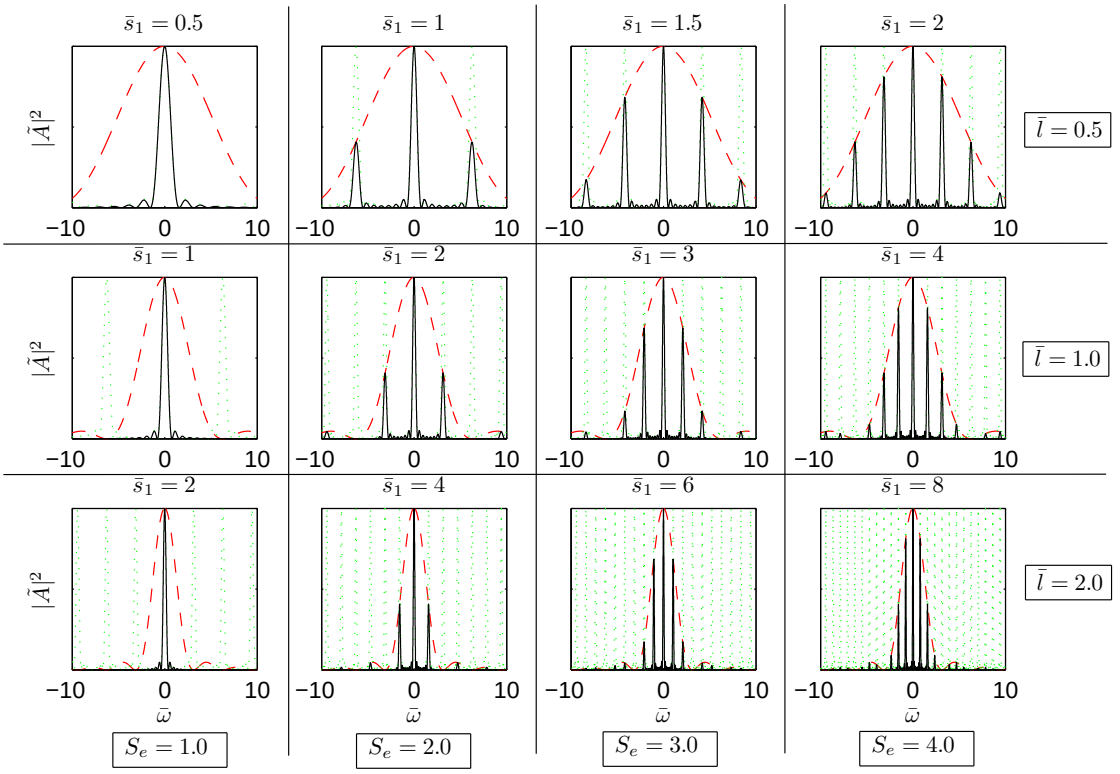

Figure 3.8: Spontaneous emission spectra, $N = 8$.

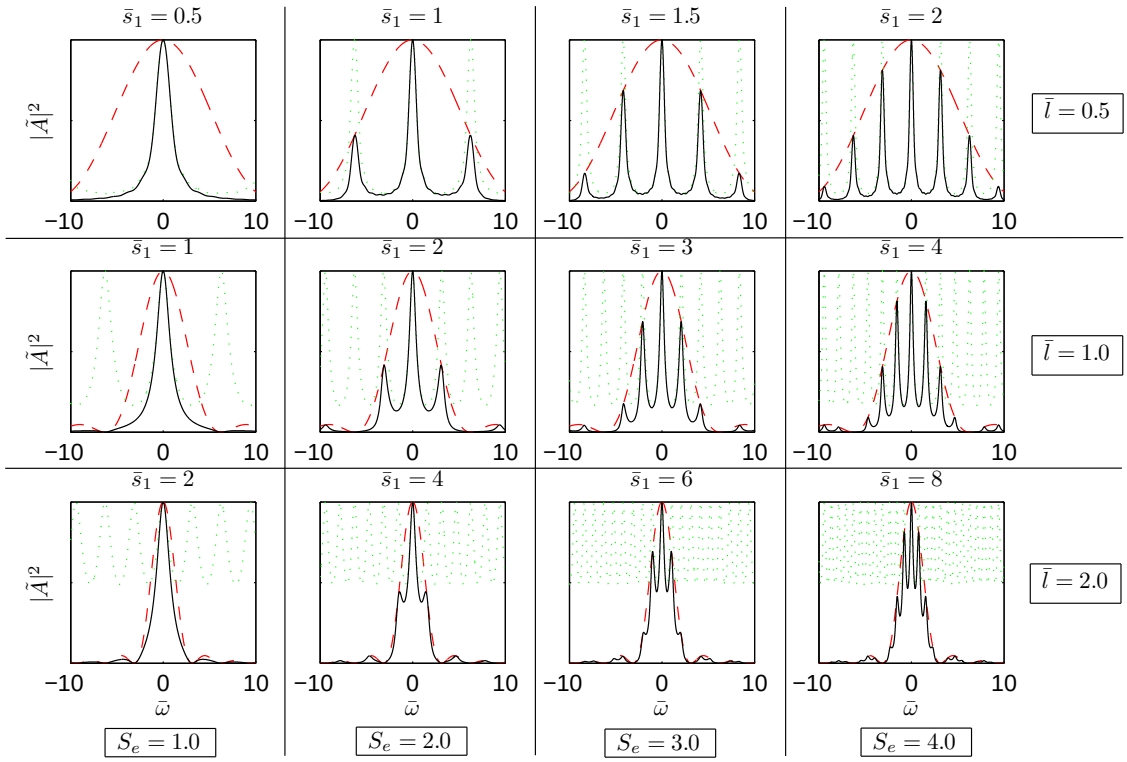

Figure 3.9: Emission spectra with gain term included, $N = 8$.

which for $\alpha = 0$ reduces to (3.33). From examination of the interference term of (3.44) it can be seen that the numerator is now a phasor of amplitude $e^{N\alpha}$ rotating about $+1$ so for $\alpha > 0$ the amplitude of this phasor is always greater than unity and hence destructive interference can never be total. Similarly, for $\alpha > 0$ the denominator can never equal zero, damping the constructive interference. Therefore the term e^{α} responsible for field amplification also acts to damp the interference and hence the visibility of the sidebands.

Recalling equation (2.193), in the linear regime field grows as $e^{\sqrt{3}\bar{z}/2}$ so the gain coefficient α can be substituted by $\alpha = \sqrt{3}\bar{l}/2$. The resulting normalised spectra, for the same parameters as shown in Figure 3.8, are shown in Figure 3.9, where it is seen that the inclusion of the gain term acts to reduce the visibility of the sidebands and increase the bandwidth around resonance, with the effect becoming more pronounced as $\bar{l}$ increases. The interference effect can be quantified in terms of the sideband visibility by examining the interference term

$$I = \frac{1 + e^{2N\alpha} - 2e^{N\alpha}\cos(N\bar{\omega}\bar{s}_1)}{1 + e^{2\alpha} - 2e^{\alpha}\cos(\bar{\omega}\bar{s}_1)} \tag{3.46}$$

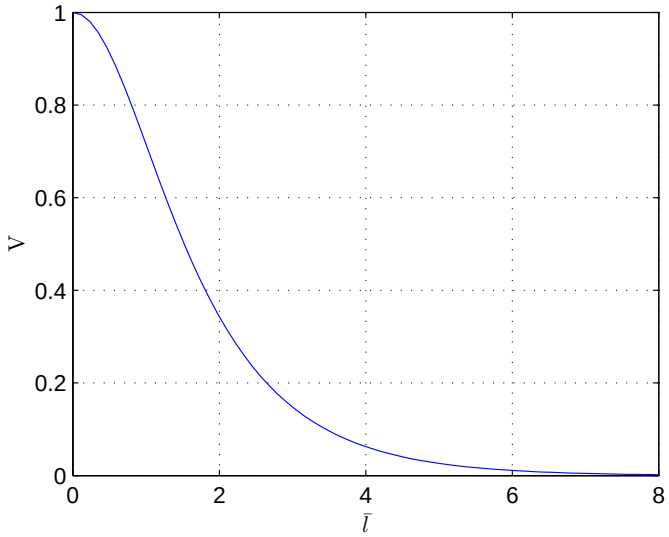

Figure 3.10: Sideband visibility V *vs* module length $\bar{l}$.

with $\alpha = \sqrt{3}\bar{l}/2$ and calculating the visibility

$$V = \frac{\max(I) - \min(I)}{\max(I) + \min(I)} \tag{3.47}$$

This has been done as a function of module length $\bar{l}$, N and $\bar{s}_1$. It is found that in fact V only depends on $\bar{l}$ and the dependency is shown in Figure 3.10. The sideband visibility is seen to decay below $1/e$ at $\bar{l} \simeq 2$.

The limitation of this analysis is that it is not based on a full solution of the coupled FEL equations. This means, for example, that the dependence on field gain as a function of frequency $\bar{\omega}$ is omitted. Also, the assumption is made that the gain is taken from the linear regime which is only valid if the FEL has risen above the lethargy regime, that is for $\bar{l} \geq 2$. Therefore the analysis can only be treated as an approximation and cannot claim to give an absolute upper limit on the acceptable undulator module length. The conclusion that can be drawn however is that the bandwidth around resonance of the output may be reduced, and hence the longitudinal coherence increased, by using short rather than long undulator modules. In subsequent sections a method to remove the sideband frequencies while maintaining a narrow bandwidth about the resonance is described.

3.5.3 Discussion

It has been shown that for equal delays the spectrum of the modular undulator-chicane system comprises sidebands with spacing $\Delta\bar{\omega} = 2\pi/\bar{s}_1$, and that by applying the delays the bandwidth around the resonance at $\bar{\omega} = 0$ continually narrows. It has also been shown that by keeping the undulator modules relatively short the sideband structure is not damped by the field gain and thus the central frequency does not overlap the sidebands, i.e. the sideband frequencies and resonance frequency are all distinct and the bandwidth at resonance is minimised. Consideration is now given to minimising the total bandwidth. To do this it is necessary to remove the sideband frequencies in a way that does not broaden the bandwidth at resonance. The idea implemented was to make each delay different such that the sideband frequencies supported by each delay (not removed by destructive interference) were unique for each delay. In this way the central frequency at $\bar{\omega} = 0$ would continue to narrow while the radiation pulse envelope would be smoothed.

3.6 Numerical Results

In this section the simulation results are presented. Initially the results from a set of ordinary SASE simulations are shown as a 'control' case then simulations with equal chicane delays, followed by the results using randomised delays. A more methodical approach was then adopted and the final section shows results using delays based on a prime number sequence. The basic simulation parameters were the same for each case to demonstrate the principle and allow a cross-comparison of the results. The parameters used were as follows: monoenergetic electron bunch with rectangular current distribution and scaled bunch length $\bar{l}_b = 3000$; undulator module length $\bar{l} = 0.5$; dispersion parameter $D = 0$; for the calculation of the correct shot noise only—electron bunch charge $Q = 1$ nC and $\rho = 2 \times 10^{-3}$.

3.6.1 SASE Control

A SASE control case was simulated initially. Figure 3.11 shows the evolution with $\bar{z}$ of the scaled radiation power $|A|^2$ (top left), the radiation coherence length $\bar{l}_{\mathrm{coh}}$ (top right), the rms radiation bandwidth $\sigma_{\bar{\omega}}$ (bottom left) and the electron beam

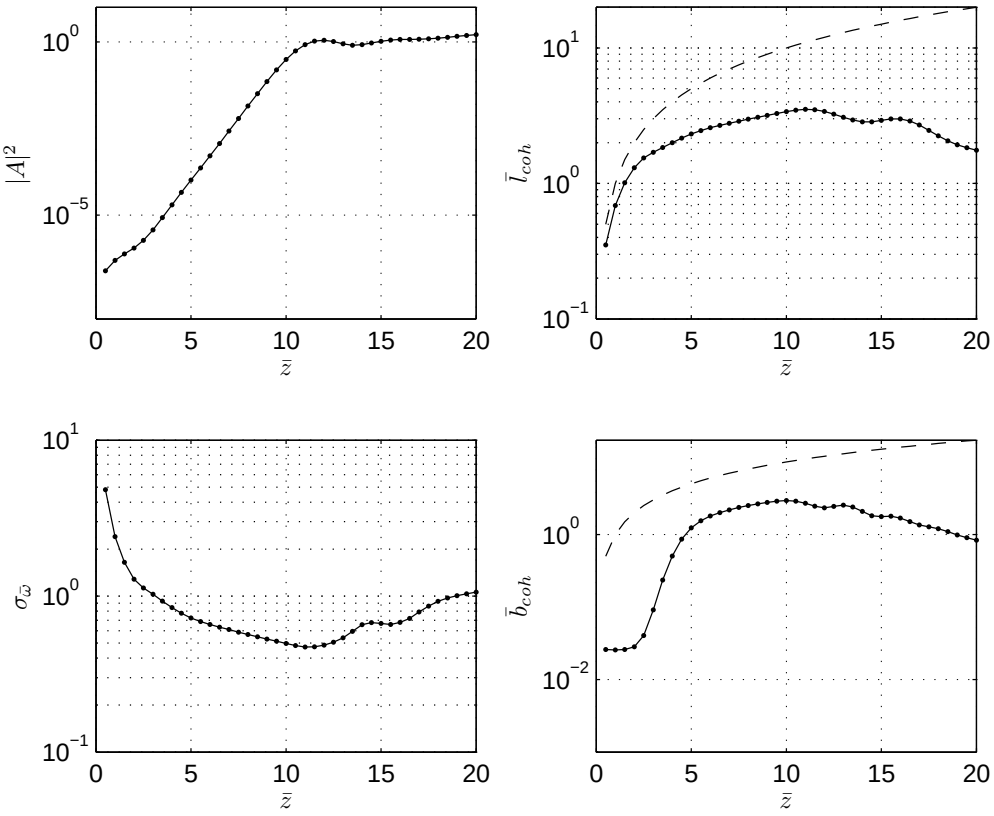

Figure 3.11: Summary data for SASE control simulations, showing scaled power $|A|^2$, radiation coherence length $\bar{l}_{\rm coh}$, radiation rms spectral width $\sigma_{\bar{\omega}}$ in units of scaled frequency $\bar{\omega}$ and bunching parameter coherence length $b_{\rm coh}$ as a function of scaled propagation distance $\bar{z}$. The dashed black lines on the plots of $\bar{l}_{\rm coh}$ and $\bar{b}_{\rm coh}$ indicate the total accumulated slippage due to the undulators as a function of propagation distance $\bar{z}$.

bunching coherence length $\bar{b}_{\rm coh}$ (bottom right), where

$$\bar{b}_{\rm coh} = \int_{-\infty}^{+\infty} |g(\bar{\tau}_1)|^2 d\bar{\tau}_1 \tag{3.48}$$

and

$$g(\bar{\tau}_1) = \frac{\langle b^*(\bar{z}_1) b(\bar{z}_1 + \bar{\tau}_1)\rangle}{\langle b^*(\bar{z}_1) b(\bar{z}_1)\rangle}. \tag{3.49}$$

so that $\bar{b}_{\rm coh}$ can be calculated using the same code as used for $\bar{l}_{\rm coh}$. The dashed black lines on the plots of $\bar{l}_{\rm coh}$ and $\bar{b}_{\rm coh}$ indicate the total accumulated slippage $\bar{S}$ as a function of propagation distance $\bar{z}$. The radiation intensity is the mean

value over the whole pulse. The intensity saturates at $|A|^2 = 1.1$ at $\bar{z} = 12$. At saturation the radiation coherence length is $\bar{l}_{\rm coh} = 3.4$ in agreement with (2.232) and the bunching coherence length is $\bar{b}_{\rm coh} = 2.3$. The rms bandwidth at saturation is $\sigma_{\bar{\omega}} = 0.48$, so from the definition of the scaled frequency (2.235) the rms bandwidth $\sigma_\lambda/\lambda \simeq \rho$ in agreement with (2.214).

The evolution of the radiation intensity profile, radiation phase and spectrum are shown in Figure 3.12, Figure 3.13 and Figure 3.14 and are seen to be typical of SASE. In each figure the output is shown columnwise in steps of $\bar{z} = 0.5$ from $\bar{z} = 0.5$ to $\bar{z} = 15.0$. For clarity the scales on the y-axes are omitted, but the convention adopted for these plots, and all subsequent equivalent plots (unless stated otherwise) is that: the scaled power $|A|^2$ is shown normalised to the peak over the whole pulse, but only a small section of the whole pulse is displayed, so the scale runs from $|A|^2 = 0$ to $|A|^2_{max}$; the phase is from $-\pi$ to π and the spectra are normalised to their peak values.

A Note on the Calculation of Coherence Length

The radiation and bunching coherence lengths are calculated using (2.223) and ((3.48)) where the integration limits are not taken to $-\infty < \bar{\tau}_1 < \infty$ but restricted to $-2\bar{S} < \bar{\tau}_1 < 2\bar{S}$ where $\bar{S} = \sum_n \bar{s}_{1,n}$ is the total accumulated slippage. The reason for this is to include only the phase correlations between sections of the radiation pulse which are causally related through the FEL interaction. An example is shown in Figure 3.15 of the coherence function $|g(\bar{\tau}_1)|^2$ for the FEL radiation output at $\bar{z} = 12$. There is a peak with maximum value $|g(\bar{\tau}_1)|^2 = 1$ at $\bar{\tau}_1 = 0$ then rapid decay to $|g(\bar{\tau}_1)|^2 \sim 10^{-4}$ at $\bar{\tau}_1 \simeq \pm 10$ so most of the contribution to the integral falls in this range. Outside this range the function is small but non-zero so if the integration is performed over $-\infty < \bar{\tau}_1 < \infty$ there is a small contribution to the integral. The total slippage to saturation is $\bar{S} = 12$ so any non-zero value in the coherence function for $|\bar{\tau}_1| > 12$ cannot be caused by the FEL interaction and must be due to a random phase correlation. Figure 3.16 shows how the calculated coherence length $\bar{l}_{\rm coh}$ depends on the integration limits $\pm\bar{R}$. It is seen that $\bar{l}_{\rm coh} \simeq 3.4$ for $5 < \bar{R} < 30$ but for $\bar{R} > 30$ the calculated $\bar{l}_{\rm coh}$ continues to increase. If $\bar{R}$ is chosen to be approximately twice the slippage the calculated value of $\bar{l}_{\rm coh}$ is unsensitive to $\bar{R}$ and close to the expected theoretical value. This choice has been made for all the calculations in this thesis.

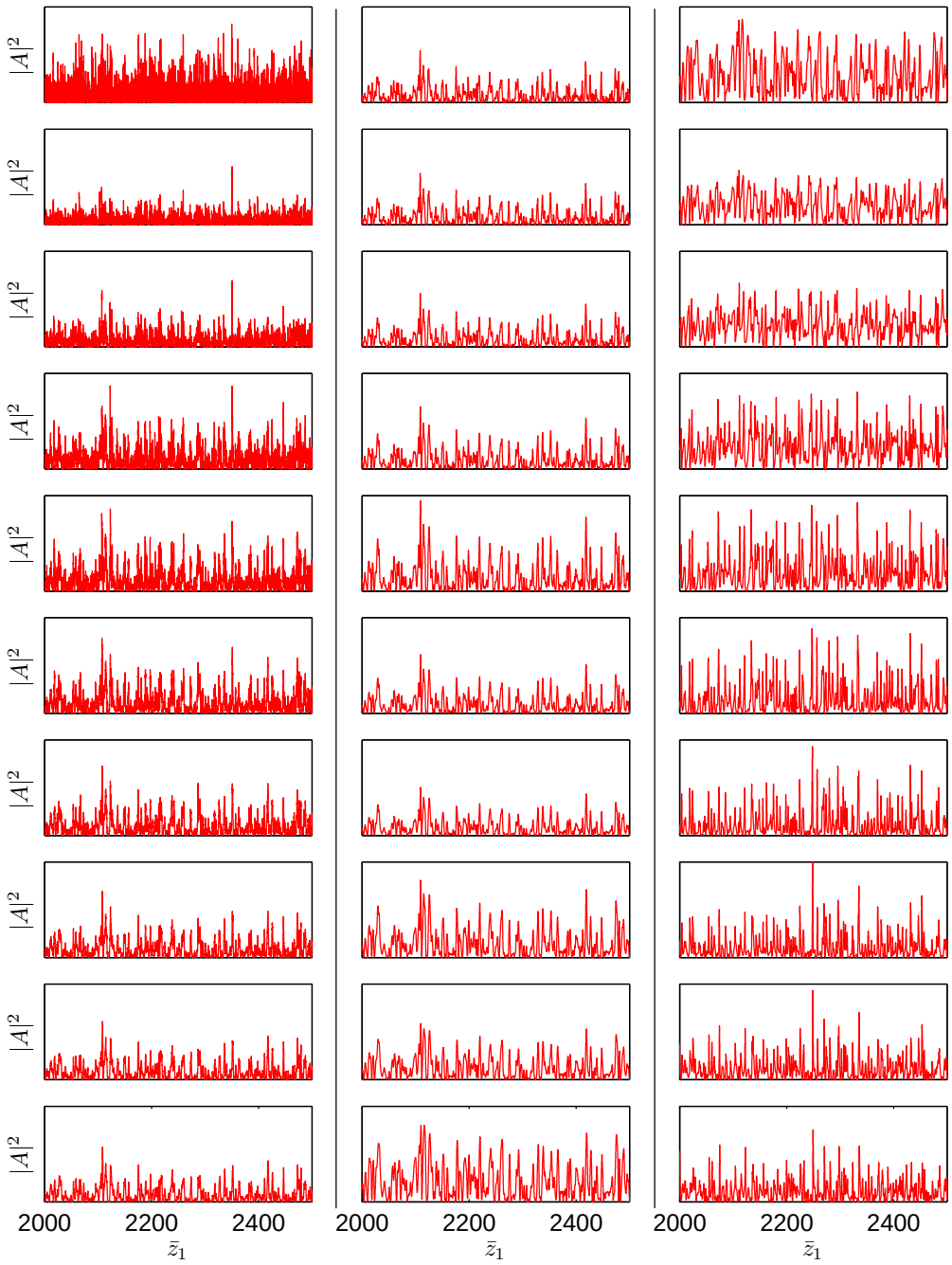

Figure 3.12: SASE control: sub-sections of the normalised intensity profiles in steps of $\bar{z} = 0.5$ from $\bar{z} = 0.5$ to $\bar{z} = 15.0$. For clarity the scale on the $|A|^2$-axis is omitted, but the convention adopted for this plot, and all subsequent equivalent plots (unless stated otherwise), is that the range of the scaled power $|A|^2$ displayed is $|A|^2 = 0$ to $|A|^2_{max}$ where $|A|^2_{max}$ is the maximum over the whole simulated pulse.

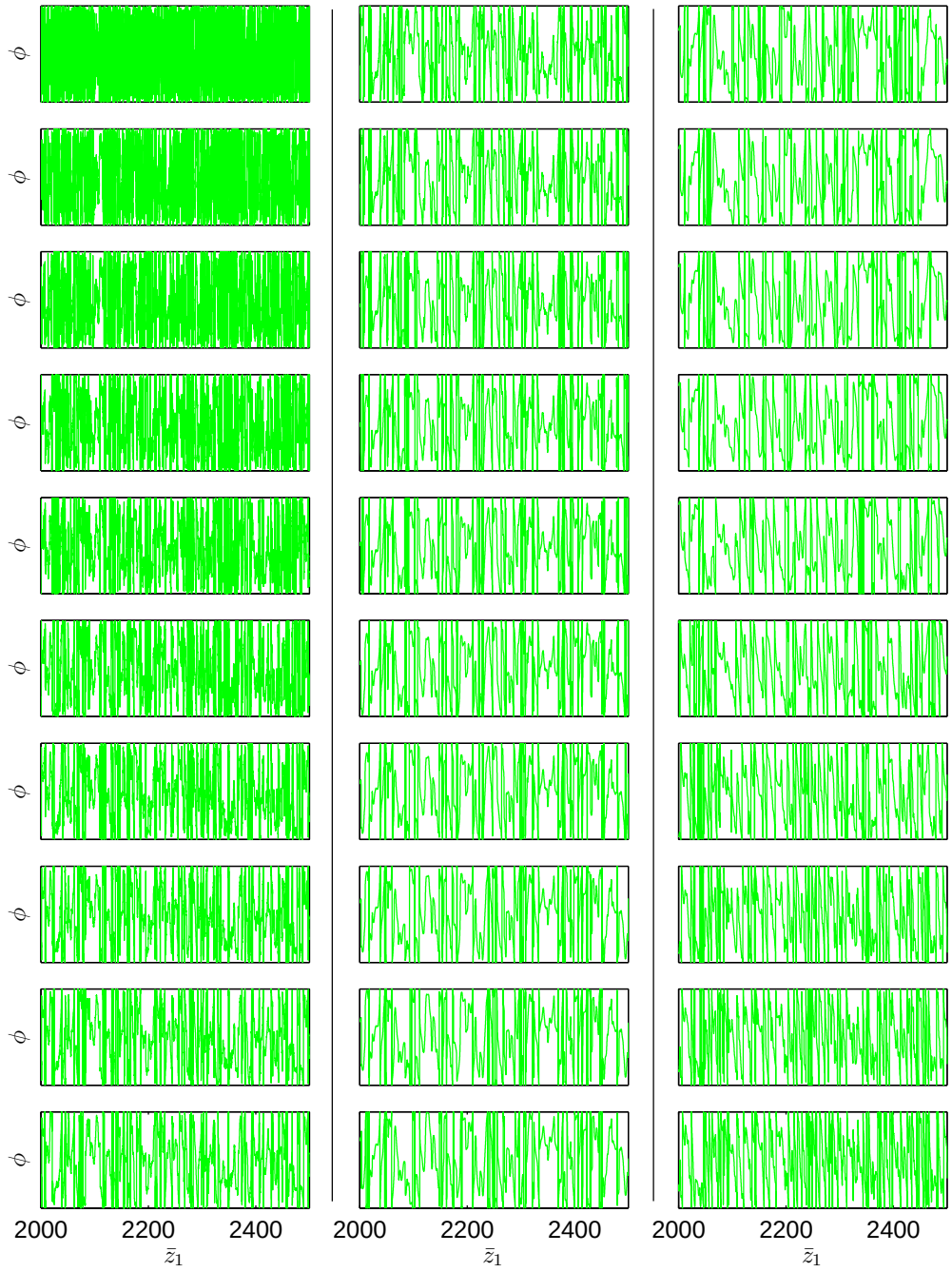

Figure 3.13: SASE control: normalised phase profiles in steps of $\bar{z} = 0.5$ in steps of $\bar{z} = 0.5$ from $\bar{z} = 0.5$ to $\bar{z} = 15.0$. The ϕ scale is omitted for clarity, but the convention adopted in this plot, and all subsequent equivalent plots, is that the scale of the ϕ axis is from $-\pi$ to π.

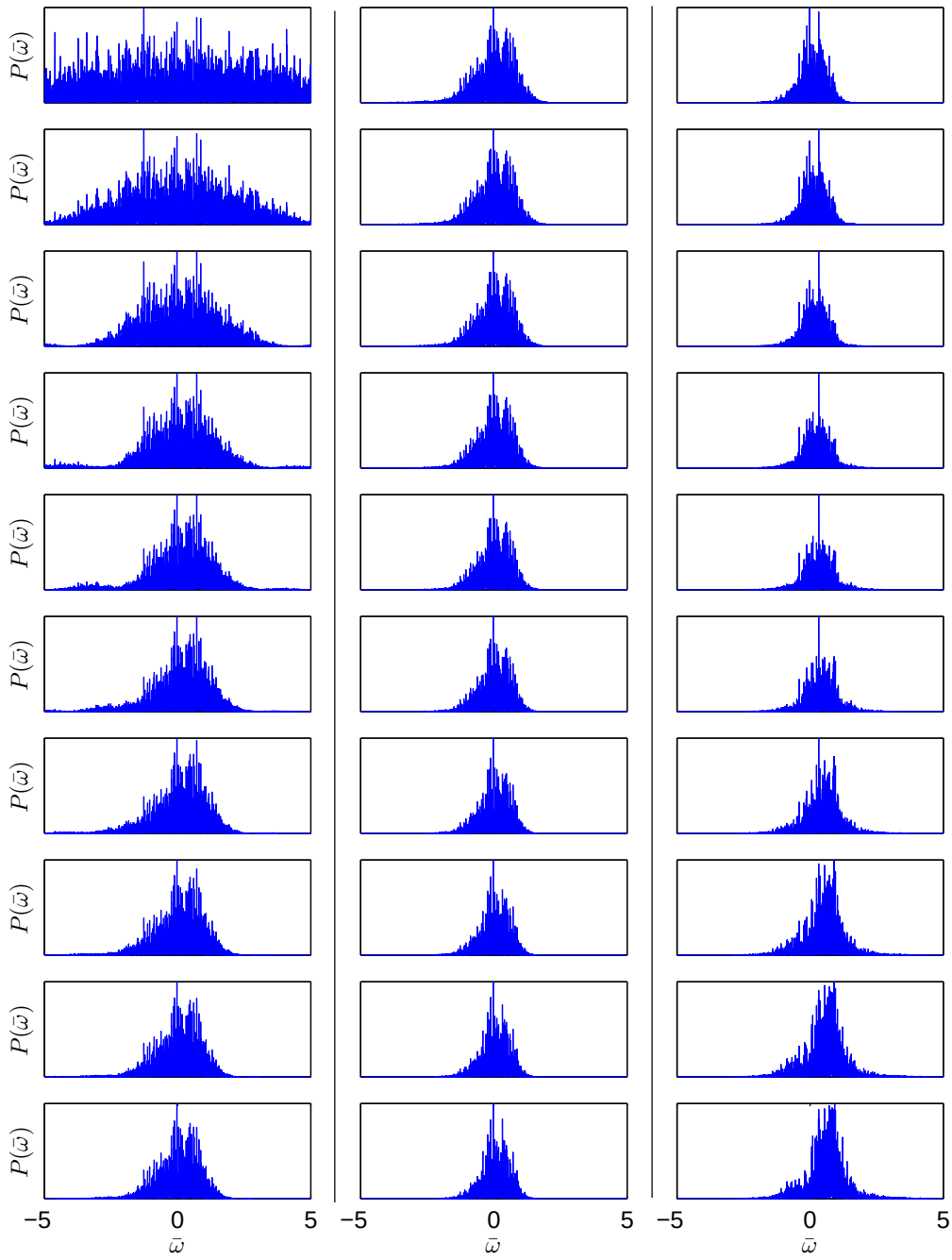

Figure 3.14: SASE control: normalised spectra in steps of $\bar{z} = 0.5$ from $\bar{z} = 0.5$ to $\bar{z} = 15.0$.

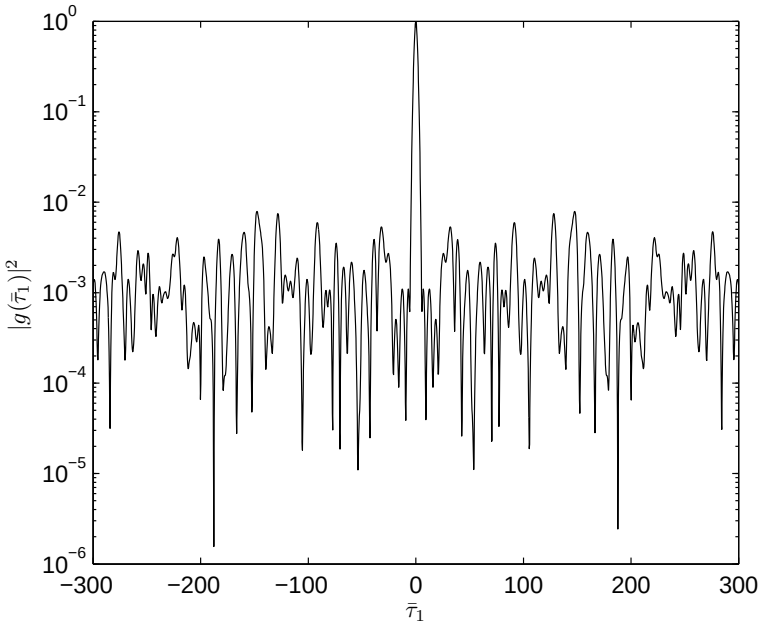

Figure 3.15: Coherence function $|g(\bar{\tau}_1)|^2$ *vs* $\bar{\tau}_1$ for the SASE control case pulse at saturation.

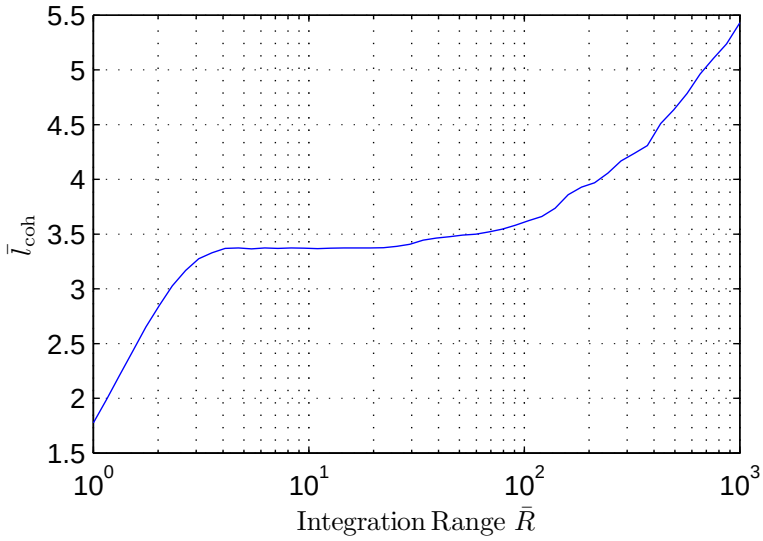

Figure 3.16: Calculated coherence length $\bar{l}_{\mathrm{coh}}$ *vs* range of integration $\bar{R}$.

3.6.2 Equal Chicane Delays

Next, equal chicane delays were applied between the undulator modules. The dispersion parameter was set to $D = 0$ to represent isochronous chicanes. This is the 'ideal' case to illustrate the concept and simplify the analysis of the results. Isochronous chicanes can be built but the challenge is to build chicanes that are also compact and variable. This has not been studied in this thesis, although designs for compact chicanes with very low dispersion have already been published [48, 49]. Section 3.7.2 presents an analysis of the performance of an HB-SASE system for $D > 0$ and shows that in fact absolute isochronicity is not required.

A number of simulations were performed with the delay $\bar{\delta}$ increasing for each simulation. The values used were $\bar{\delta}$ =[5.1, 8.9, 11.2, 17.35, 23.46, 48.0]. Figure 3.17 shows the evolution in $\bar{z}$ of the radiation intensity $|A|^2$ averaged over the pulse (top left), the radiation coherence length $\bar{l}_{\rm coh}$ (top right), the rms radiation bandwidth $\sigma_{\bar{\omega}}$ (bottom left) and the electron beam bunching coherence length $\bar{b}_{\rm coh}$ (bottom right). The dashed lines on the plots of $\bar{l}_{\rm coh}$ and $\bar{b}_{\rm coh}$ indicate the total accumulated slippage $\bar{S}$ as a function of propagation distance $\bar{z}$. For the analysis in each case the region at the back of the pulse of length equal to the total slippage up to saturation is trimmed so any effects due to radiation slipping into the pulse are excluded. Each plot also shows the results from the SASE control case of Section 3.6.1 to allow the effects of adding the delays to be clear. It is seen that the radiation intensity growth differs little from SASE. The radiation coherence length is improved over SASE by at most a factor of 3.3. For chicane delay $\bar{\delta} = 8.9$ it is seen that the coherence length $\bar{l}_{\rm coh} = 11.2$ compared to $\bar{l}_{\rm coh} = 3.4$ for SASE and in fact $\bar{l}_{\rm coh}$ differs little with $\bar{\delta}$. The radiation bandwidth at saturation is $\sigma_{\bar{\omega}} \approx 2$, a factor of four broader than SASE and again has very little dependence on $\bar{\delta}$.

The evolution of the radiation intensity profile, radiation phase and spectrum, for $\bar{\delta} = 48.0$, are shown in Figure 3.19, Figure 3.20 and Figure 3.21. As for the SASE control case, in each figure the output is shown columnwise in steps of $\bar{z} = 0.5$. The intensities are shown normalised to the peak over the whole pulse, but only a small section of the whole pulse is displayed. The phase is from $-\pi$ to π and the spectra are normalised. The pulse intensity shows clear repeated temporal structure with a period of 48.5. Whereas the SASE spectra of Figure 3.14 were clearly chaotic the spectra for equal delays show the equally spaced sidebands—an enlarged spectrum for $\bar{\delta}$, at a distance of $\bar{z} = 12$, is shown in

Figure 3.18.

To conclude, the effect of adding equal delays is a moderate increase in coherence length, which quickly saturates as the delays are made larger, the generation of periodic structure in the temporal pulse profile and very broad bandwidth output composed of multiple equally spaced frequency lines. These results indicate that just increasing the slippage is not in itself sufficient to give a significant increase in coherence length.

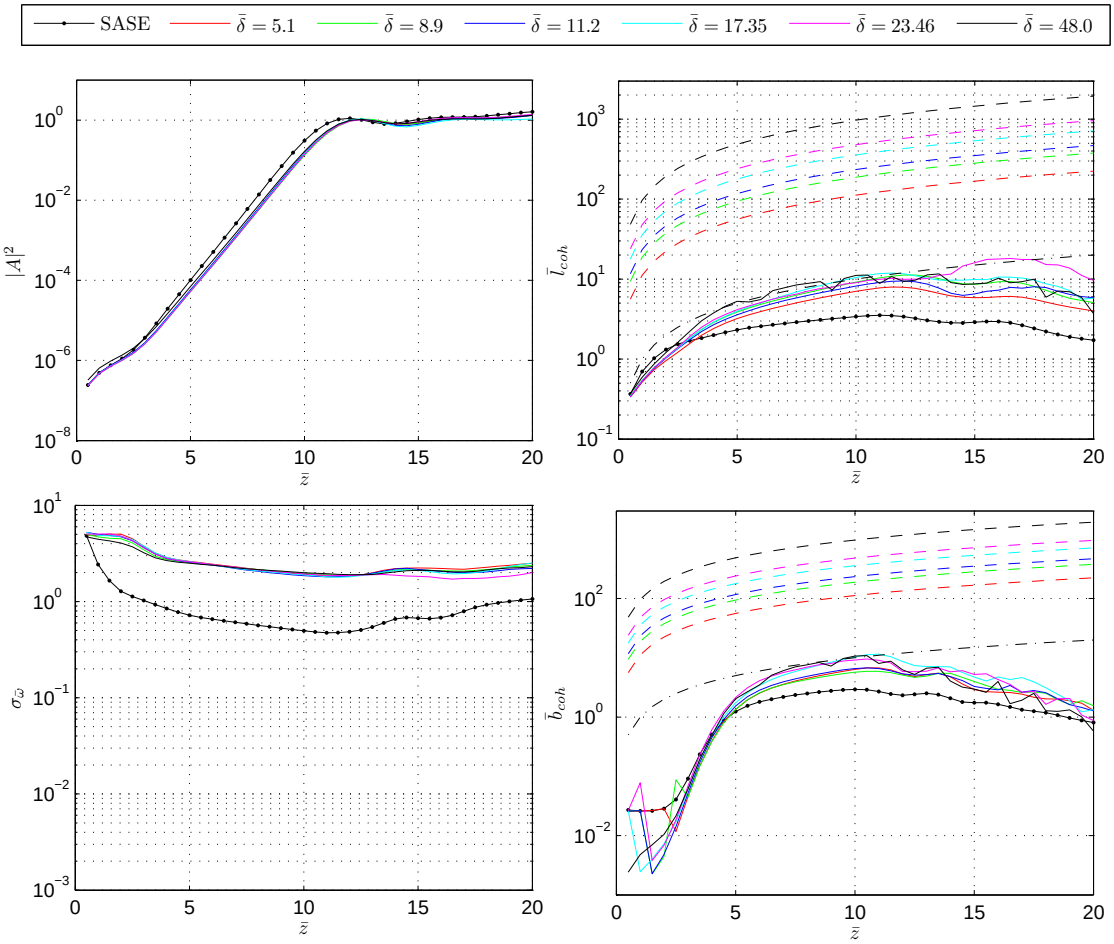

Figure 3.17: Equal chicane delays. The evolution in $\bar{z}$ of the radiation intensity $|A|^2$ averaged over the pulse (top left), the radiation coherence length $\bar{l}_{\rm coh}$ (top right), the rms radiation bandwidth $\sigma_{\bar{\omega}}$ (bottom left) and the electron beam bunching coherence length $\bar{b}_{\rm coh}$ (bottom right). The dashed lines on the plots of $\bar{l}_{\rm coh}$ and $\bar{b}_{\rm coh}$ indicate the total accumulated slippage $\bar{S}$.

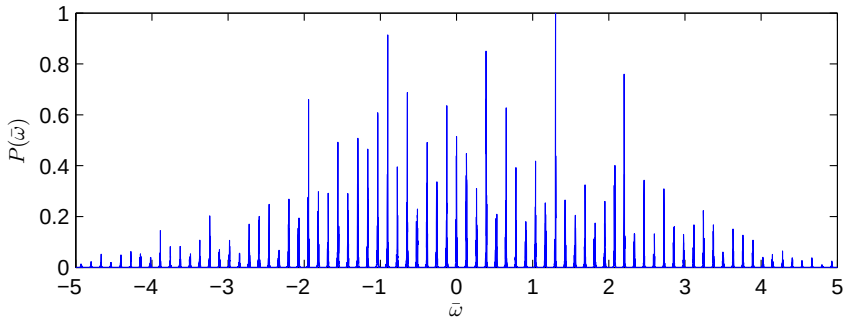

Figure 3.18: Equal chicane delays of $\bar{\delta} = 48$: normalised spectrum at $\bar{z} = 12$ showing the evenly spaced sidebands.

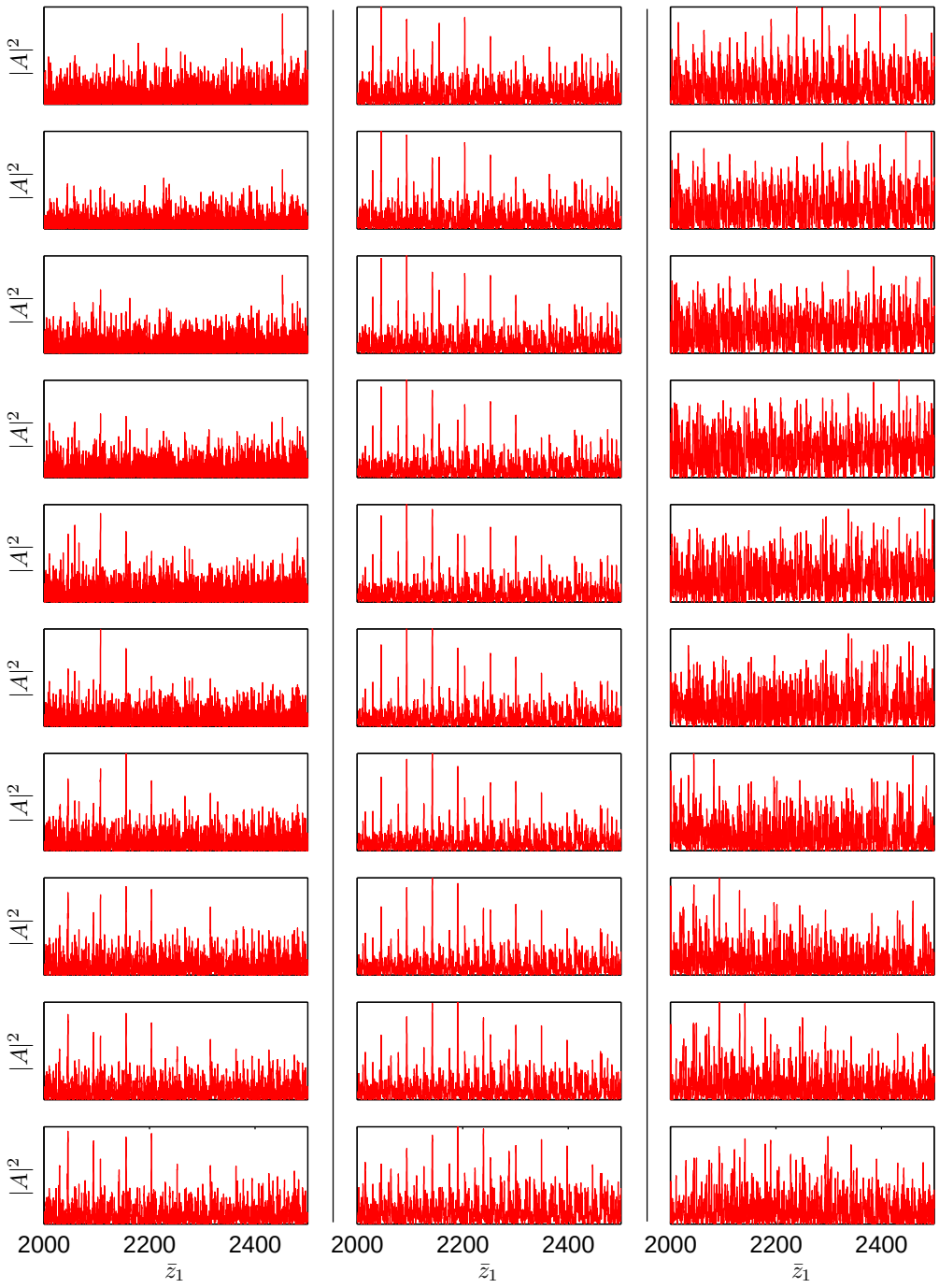

Figure 3.19: Equal chicane delays of $\bar{\delta} = 48$: normalised intensity profiles in steps of $\bar{z} = 0.5$ from $\bar{z} = 0.5$ to $\bar{z} = 15.0$. Structure with a period of $\tau = 48.5$ is evident.

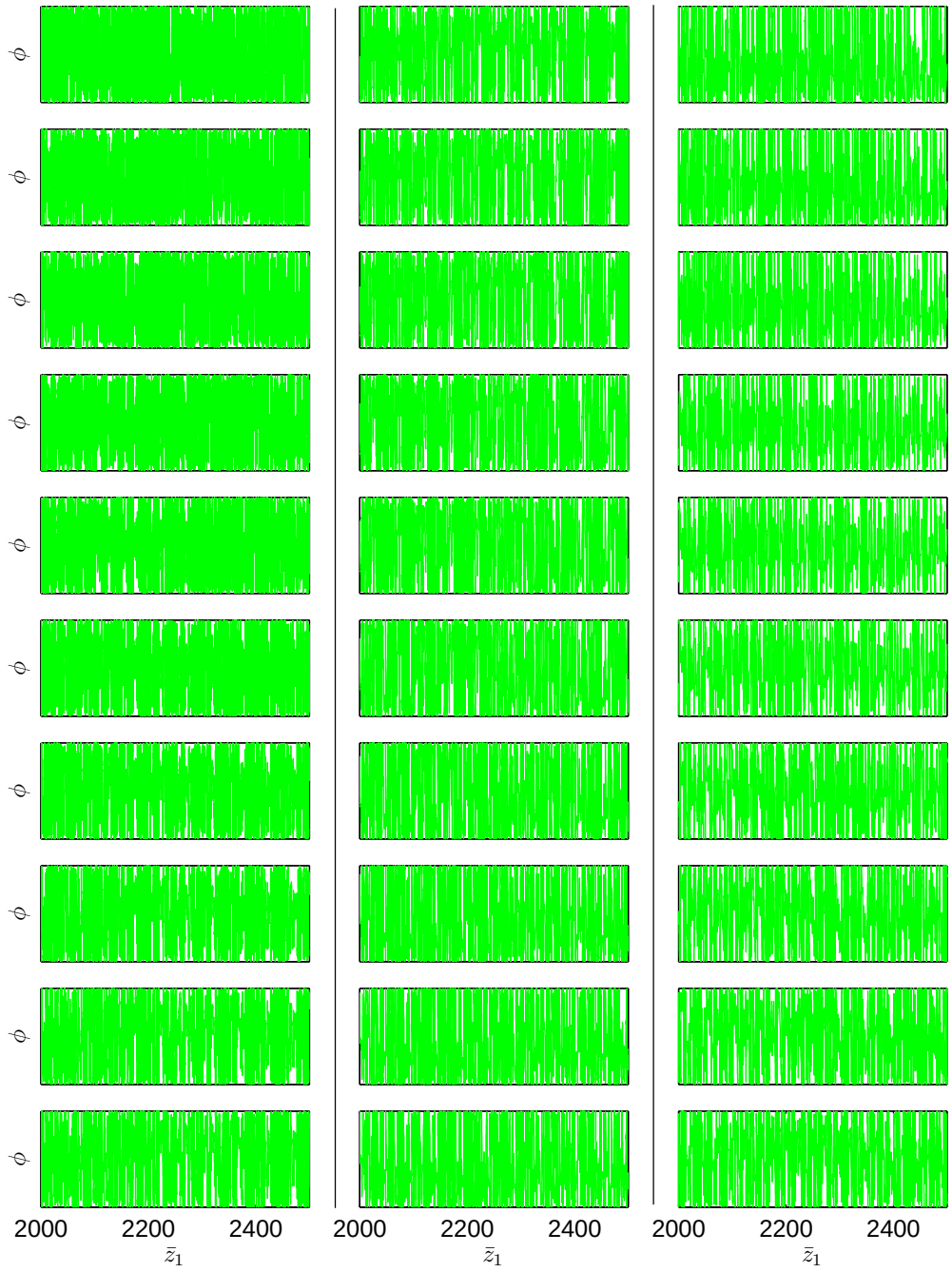

Figure 3.20: Equal chicane delays of $\bar{\delta} = 48$: normalised phase profiles in steps of $\bar{z} = 0.5$ from $\bar{z} = 0.5$ to $\bar{z} = 15.0$. The rate of phase variation appears qualitatively much more rapid than in the SASE results in Figure 3.13.

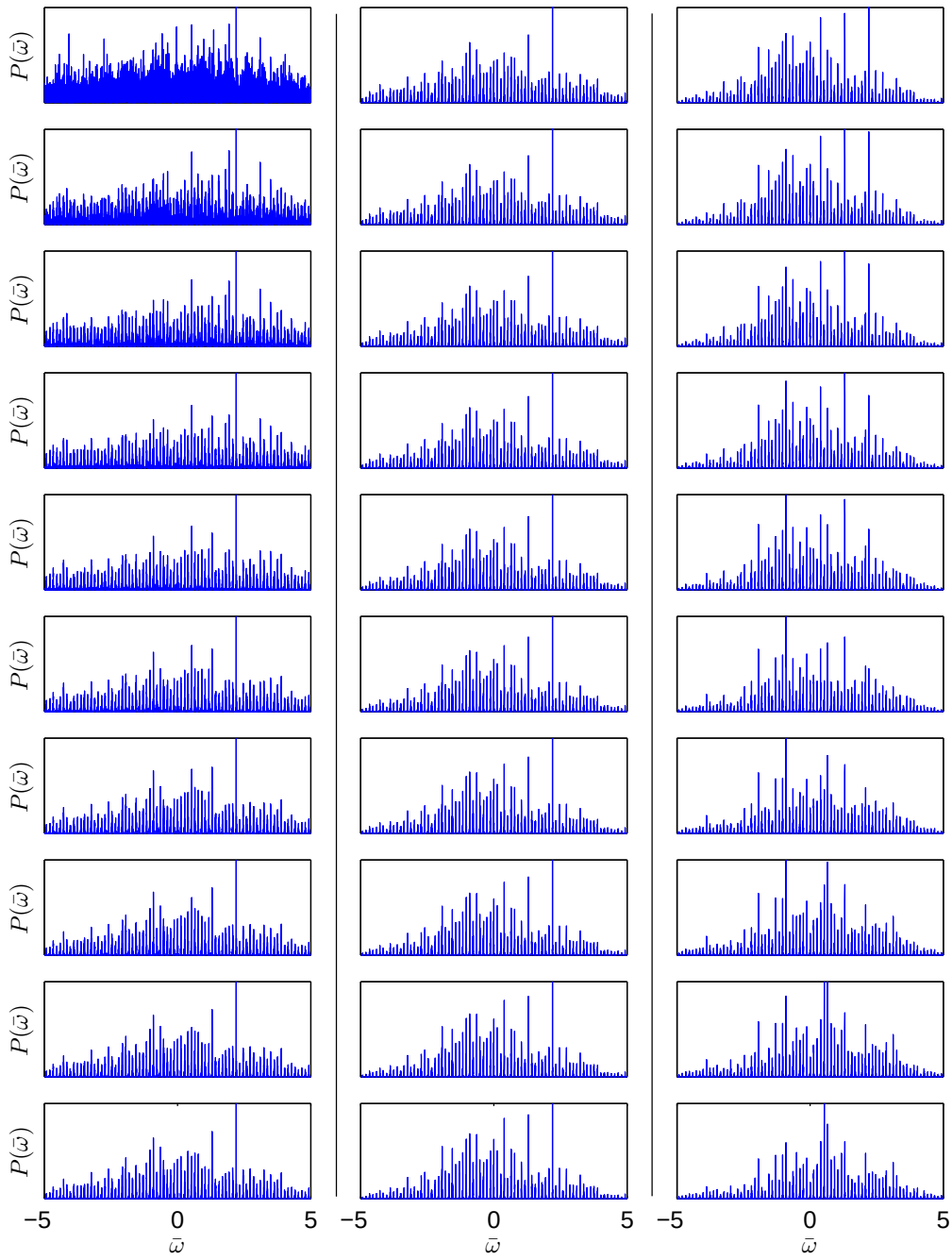

Figure 3.21: Equal chicane delays of $\bar{\delta} = 48$: normalised spectra in steps of $\bar{z} = 0.5$ from $\bar{z} = 0.5$ to $\bar{z} = 15.0$.

3.6.3 Random Chicane Delays

As motivated in Section 3.5.3 the delays were then randomised in a uniform distribution $\bar{\delta}_n = [0, 2\langle\bar{\delta}\rangle]$ about the mean delay $\langle\bar{\delta}\rangle$, with the mean delays set to match the equal delays used in the previous section. Figure 3.22 shows the evolution with $\bar{z}$ of $|A|^2$, $\bar{l}_{\mathrm{coh}}$, $\sigma_{\bar{\omega}}$ and $\bar{b}_{\mathrm{coh}}$. Figures 3.23–3.25 show the radiation intensity profile, radiation phase and spectra for $\langle\bar{\delta}\rangle = 48.0$.

The behaviour is now quite different. The radiation intensity growth rate is slightly reduced from SASE, reaching saturation at $\bar{z} = 14$ rather then $\bar{z} = 12$, but the pulse saturates at the same intensity. The coherence length is up to two orders of magnitude longer than SASE, depending on the delay applied. The longest coherence length corresponds to the largest mean delay $\langle\bar{\delta}\rangle = 48.0$ where $\bar{l}_{\mathrm{coh}} = 398$ at $\bar{z} = 14$, 117 times longer than the SASE value at saturation. The total accumulated slippage in this case is $\bar{S} = 1267$. In all cases it is seen that $\bar{l}_{\mathrm{coh}}$ never exceeds $\bar{S}$. The evolution of the radiation bandwidth with $\bar{z}$ is qualitatively different from SASE—it decreases initially much more slowly, but at saturation is reduced by a factor of up to two orders of magnitude. For $\langle\bar{\delta}\rangle = 48.0$ the bandwidth at saturation is $\sigma_{\bar{\omega}} = 6.5 \times 10^{-3}$. The pulse power profiles show a slowly varying envelope developing out of the noise, and the phase profiles show similar characteristics, with the smoothly varying phase slowly evolving out of the initial noise. As the spectrum evolves with $\bar{z}$ the sidebands away from resonance gradually decay relative to the clear developing spike at resonance. The spectra for the SASE control and for random chicane delays with $\langle\bar{\delta}\rangle = 48.0$ are compared in Figure 3.26, on both a linear and a logarithmic scale, with each spectrum independently normalised. On a linear scale the spectrum for random delays appears as a single sharp line compared to the broad noisy SASE spectrum. Viewed on the logarithmic scale the spectrum for random chicane delays shows some residual sidebands but with an intensity two orders of magnitude less than the intensity at resonance.

A Note on Bandwidth Calculation

The sudden reduction in bandwidth seen between $\bar{z} = 13.5$ and $\bar{z} = 14$ is an artefact of the numerical calculation of the bandwidth. The spectrum of the system is very broad at small $\bar{z}$ then becomes very narrow towards saturation, as shown in Figure 3.25. The rms calculation is very sensitive to low levels of spectral power at frequencies a long way from the mean weighted frequency

which increase the calculated width 'disproportionately'. The solution is either to artificially restrict the calculation to some window around the feature of interest, or to threshold the power before making the calculation. It was more convenient for these simulations, where the bandwidth changes by orders of magnitude, to apply a threshold. The threshold was set to be 1% of the peak intensity by studying the SASE control case to determine the threshold at which the calculated bandwidth was independent of the frequency window width and agreed with the theoretical value. The same threshold was used for all calculations of different delay sequences and therefore gives a fair comparison between different schemes.

For the case discussed here, $\langle\bar{\delta}\rangle = 48.0$, at $\bar{z} = 13.5$ there is a residual sideband at $\bar{\omega} = -2.64$ with peak normalised power level 0.012 which is then contributing to the rms calculation, but after the next undulator module this sideband has dropped below the threshold and is excluded, and the rms changes significantly because the excluded sideband frequency is far from resonance.

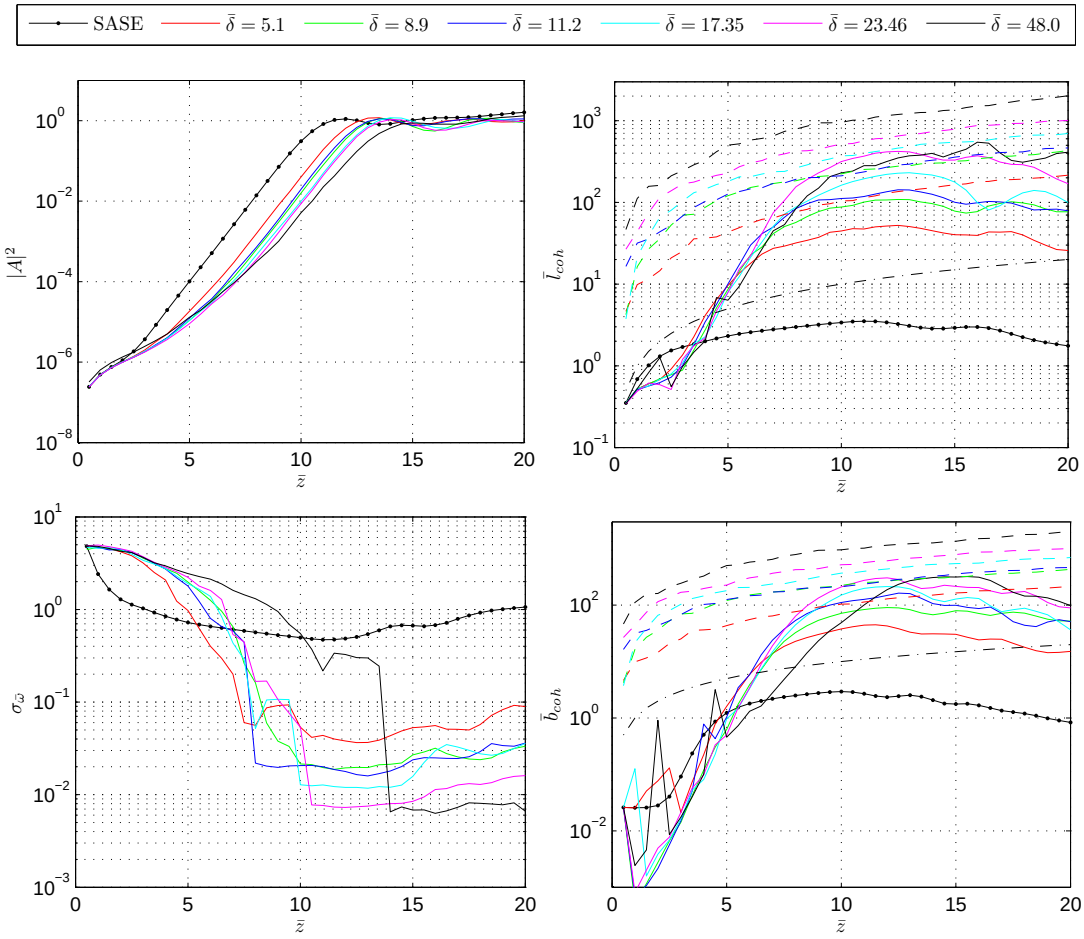

Figure 3.22: Random chicane delays. The evolution in $\bar{z}$ of scaled power $|A|^2$, radiation coherence length $\bar{l}_{\rm coh}$, rms bandwidth $\sigma_{\bar{\omega}}$ and bunching coherence length $\bar{b}_{\rm coh}$. The radiation and bunching coherence lengths at saturation exceed that of the SASE control case by up to two orders of magnitude, with a corresponding reduction in bandwidth.

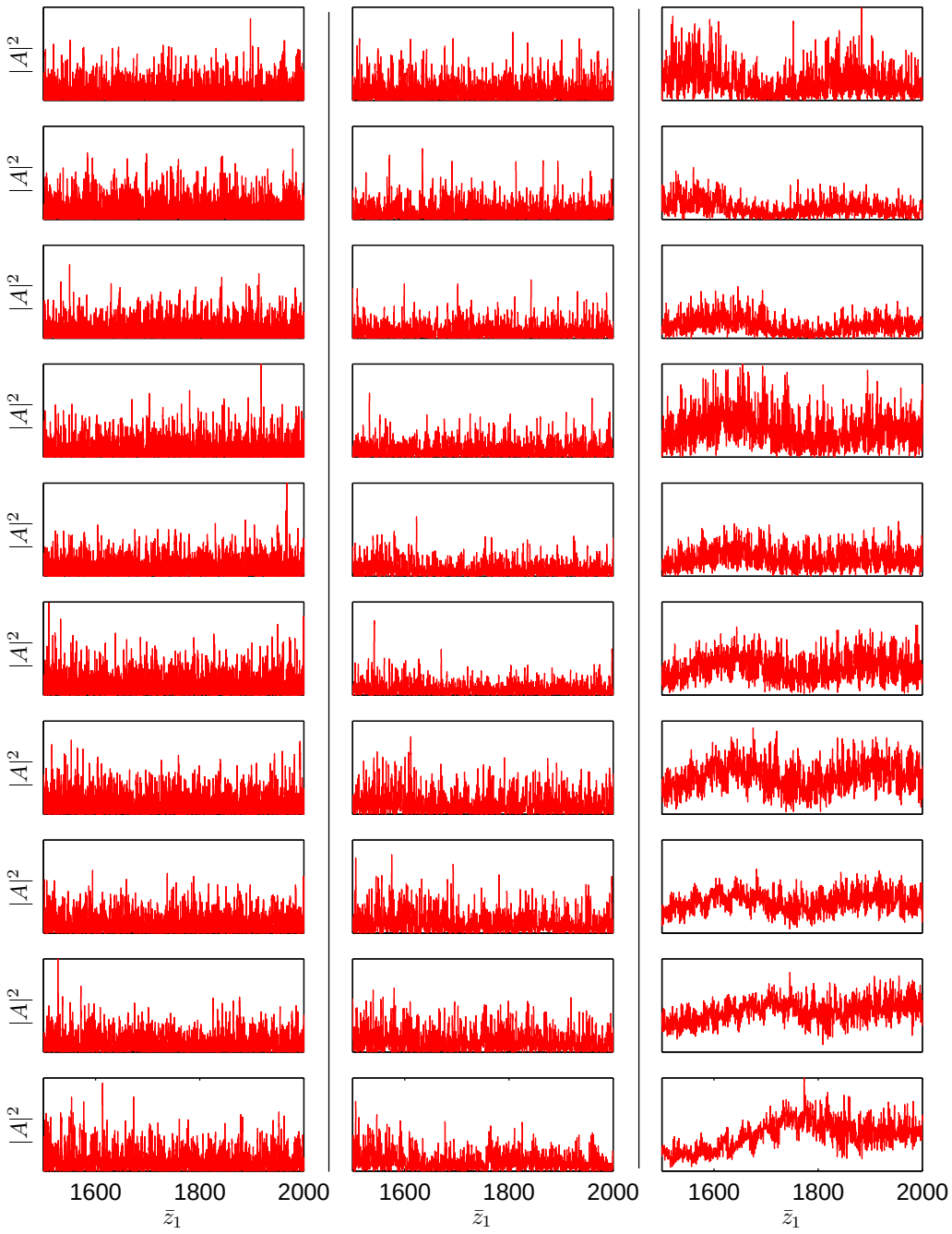

Figure 3.23: Random chicane delays of $\langle\bar{\delta}\rangle = 48.0$: normalised intensity profiles in steps of $\bar{z} = 0.5$ from $\bar{z} = 0.5$ to $\bar{z} = 15.0$. By saturation at $\bar{z} = 14.0$ the pulse profile has become a slowly varying, but noisy, envelope.

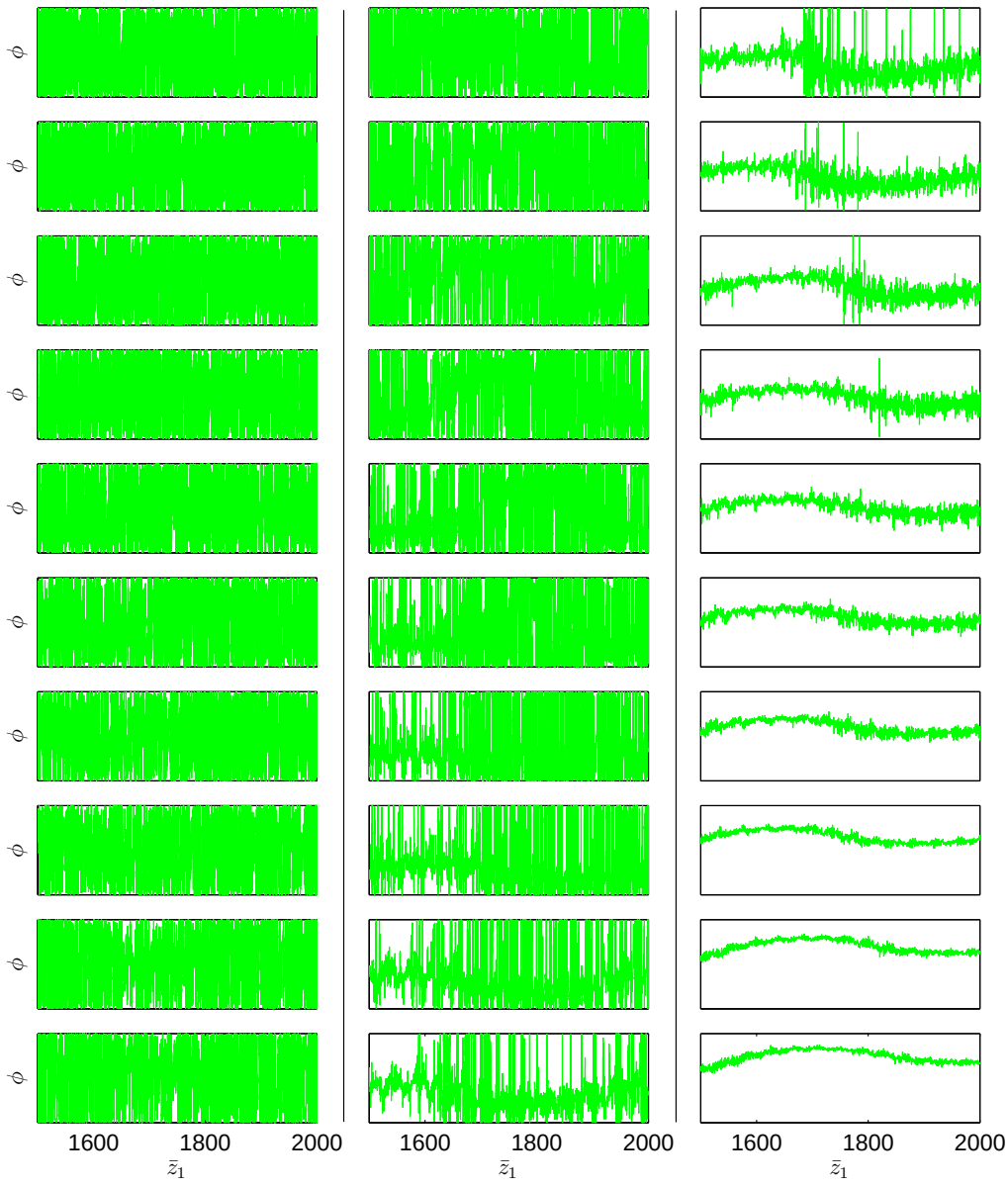

Figure 3.24: Random chicane delays of $\langle\bar{\delta}\rangle = 48.0$: normalised phase profiles in steps of $\bar{z} = 0.5$ from $\bar{z} = 0.5$ to $\bar{z} = 15.0$. By saturation a smoothly varying phase has evolved from the initial noise, indicating good longitudinal coherence.

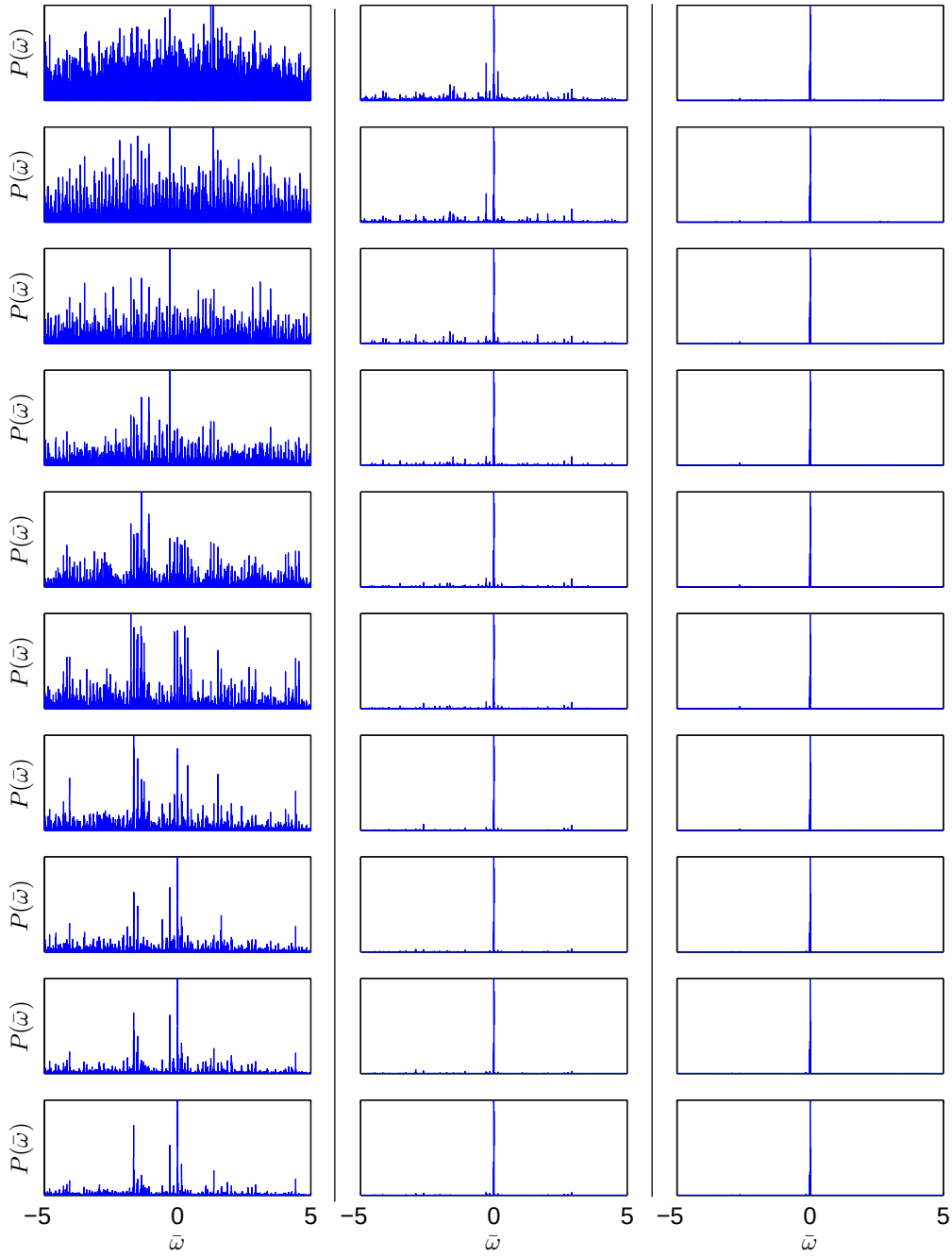

Figure 3.25: Random chicane delays of $\langle\bar{\delta}\rangle = 48.0$: normalised spectra in steps of $\bar{z} = 0.5$ from $\bar{z} = 0.5$ to $\bar{z} = 15.0$. As the spectrum evolves with $\bar{z}$ the sidebands away from resonance gradually decay relative to the clear developing spike at resonance.

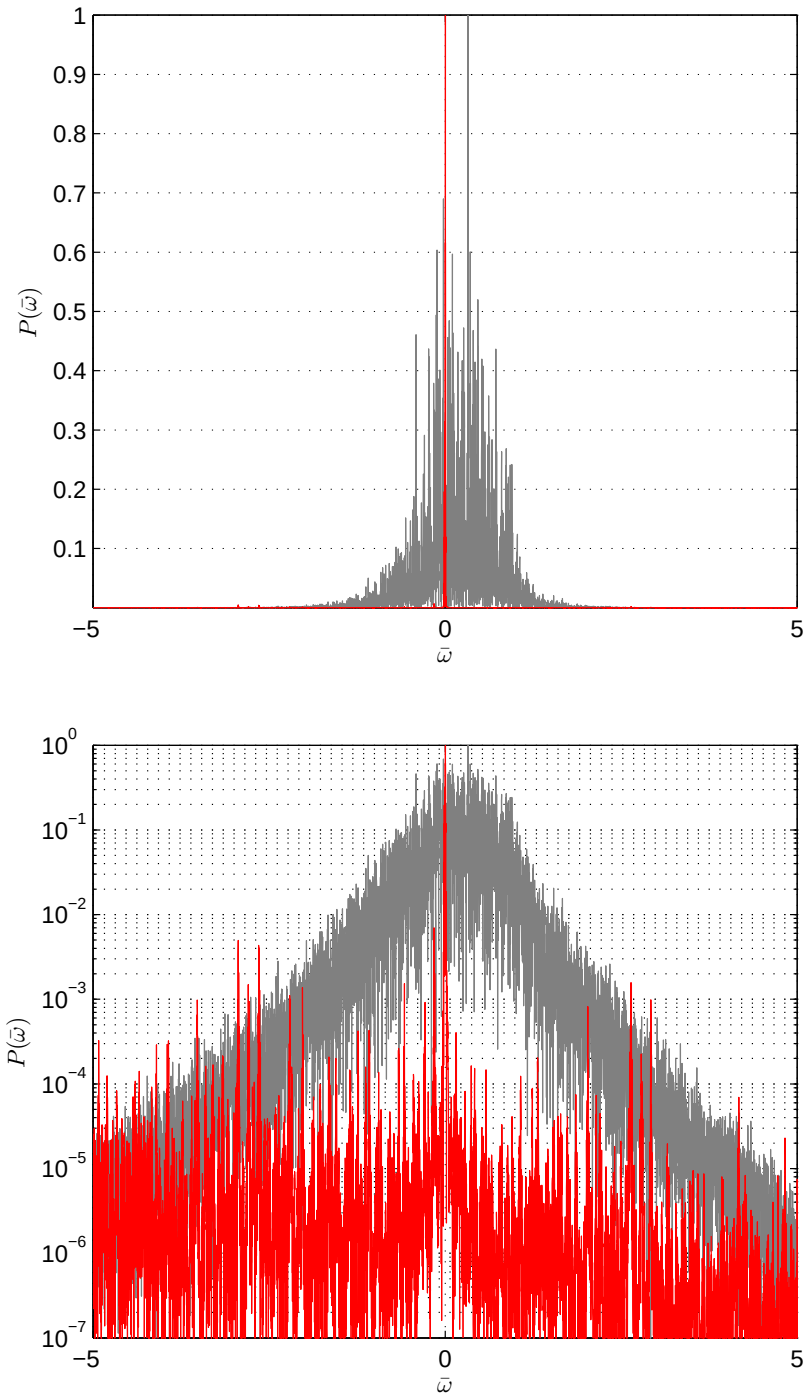

Figure 3.26: Comparison of normalised spectra at saturation, for SASE control (grey) and random delays with $\langle\bar{\delta}\rangle = 48.0$ (red). On a linear scale the spectrum for random delays appears as a single sharp line compared to the broad noisy SASE spectrum. Viewed on the logarithmic scale the spectrum for random chicane delays shows some residual sidebands but with an intensity two orders of magnitude less than the intensity at resonance.

		n						
i	$\mathbb{P}_i$	**1**	**2**	**3**	**4**	**5**	**6**	**7**
1	**2**	$\frac{1}{2}$	$\boxed{\frac{2}{2}}$	$\frac{3}{2}$	$\frac{4}{2}$	$\frac{5}{2}$	$\frac{6}{2}$	$\frac{7}{2}$
2	**3**	$\frac{1}{3}$	$\frac{2}{3}$	$\boxed{\frac{3}{3}}$	$\frac{4}{3}$	$\frac{5}{3}$	$\frac{6}{3}$	$\frac{7}{3}$
3	**5**	$\frac{1}{5}$	$\frac{2}{5}$	$\frac{3}{5}$	$\frac{4}{5}$	$\boxed{\frac{5}{5}}$	$\frac{6}{5}$	$\frac{7}{5}$
4	**7**	$\frac{1}{7}$	$\frac{2}{7}$	$\frac{3}{7}$	$\frac{4}{7}$	$\frac{5}{7}$	$\frac{6}{7}$	$\boxed{\frac{7}{7}}$
5	**11**	$\frac{1}{11}$	$\frac{2}{11}$	$\frac{3}{11}$	$\frac{4}{11}$	$\frac{5}{11}$	$\frac{6}{11}$	$\frac{7}{11}$

Table 3.1: Sideband frequencies $\bar{\omega}_{i,n}/(4\pi/\bar{l}F)$. The boxes highlight the common frequencies.

3.6.4 Prime Number Delays

A more methodical technique to ensure cancellation of the sidebands was adopted. To avoid common supported sideband frequencies between any two delays in the series a sequence based on prime number increases was used. The combined delay $\bar{s}_i = \bar{l} + \bar{\delta}_i$ for the ith undulator/chicane is given by

$$\bar{s}_i = \frac{\mathbb{P}_i \bar{l} F}{2} \tag{3.50}$$

where $\mathbb{P}$=[2, 3, 5, 7, 11, 13...] is the sequence of prime numbers. F is a factor which scales the whole sequence to change the total slippage. This definition for $\bar{s}_i$ is chosen such that

$$\bar{s}_1 = \frac{\mathbb{P}_1 \bar{l} F}{2} = \bar{l} F \tag{3.51}$$

and hence

$$F = \frac{\bar{s}_1}{\bar{l}} \tag{3.52}$$

so F is also the slippage enhancement factor *but for the first undulator/chicane module only*. Note also that for $F < 1$ then $\bar{s}_1 < \bar{l}$ which is unphysical because it implies a negative delay $\bar{\delta}$ in the chicane, or electrons moving faster than light. The simulation code checks this condition and sets $\bar{\delta} = 0$ in this situation.

The sideband frequencies supported by the ith delay occur at

$$\bar{\omega}_{i,n} = n\frac{2\pi}{\bar{s}_i} = \frac{n}{\mathbb{P}_i}\left(\frac{4\pi}{\bar{l}F}\right) \tag{3.53}$$

where (3.50) has been substituted. Table 3.1 shows $\bar{\omega}_{i,n}/(4\pi/\bar{l}F)$. In this table each row represents the sideband frequencies $\bar{\omega}_n$ supported by the ith delay. As the delays increase according to the prime number sequence the frequencies supported become more closely spaced. It is seen that there is in fact a common frequency $\bar{\omega}_c$ supported over all the delays which occurs whenever $n = \mathbb{P}_i$ giving

$$\bar{\omega}_c = \frac{4\pi}{\bar{l}F}. \tag{3.54}$$

It has already been seen that the full gain bandwidth is given by the width of the sinc^2 envelope function which reaches its first zero at $\bar{\omega} = 2\pi/\bar{l}$. It is therefore necessary that for no common frequencies to exist within the gain envelope

$$\bar{\omega}_c = \frac{4\pi}{\bar{l}F} > \frac{2\pi}{\bar{l}} \tag{3.55}$$

which gives a constraint on the value of the scaling factor for efficient cancelation of the sideband frequencies

$$F < 2. \tag{3.56}$$

No attempt has been made to circumvent this limit in the work in this thesis, and simulations using prime delays have been performed up to a scaling of $F = 4$. To increase the total slippage while satisfying $F < 2$ it would only be necessary to start the prime number sequence at a higher prime number than 2.

A number of simulations were done with the scale factor F set so that the total slippage to saturation in each case approximately matched that of the set of simulations with random delays. The values used were F=[0.5, 0.81, 1.0, 1.5, 2.0, 4.0]. Figure 3.27 shows the evolution with $\bar{z}$ of $|A|^2$, $\bar{l}_{\text{coh}}$, $\sigma_{\bar{\omega}}$ and $\bar{b}_{\text{coh}}$. Figures 3.28–3.30 show the radiation intensity profile, radiation phase and spectra for $F = 4.0$ then Figures 3.31 and 3.32 show the spectra with the $\bar{\omega}$ axis expanded by factors of 10 and 100 respectively.

It is observed that the radiation growth rate is very similar to the cases with random delays, with the power reaching saturation at $\bar{z} = 14$ in all cases. The coherence length at saturation increases with F as the delay sequence is scaled up increasing the total slippage. The maximum is $\bar{l}_{\text{coh}} = 514$ for $F = 4.0$, a factor of 150 increase over the SASE value. The minimum bandwidth at saturation is $\sigma_\omega = 4.2 \times 10^{-3}$, a reduction of 115 compared to SASE. The evolution of the power profiles and phases profiles are qualitatively similar to the case with

random chicane delays, whereas the evolution of the spectrum is different—for small $\bar{z}$ the sideband modes are much wider because in this delay sequence the initial delays are small then increase from one chicane to the next, whereas the random delays can be large at small $\bar{z}$ giving more closely spaced and narrower sidebands. A comparison of normalised spectra at saturation, for SASE control (grey) and prime number delays with $F = 4.0$ (red), is shown in Figure 3.33. Comparison with Figure 3.26 shows that the prime number delays appear more efficient at suppressing the sidebands than the random chicane delays.

It is also noted that for $F = 4.0$ the coherence length grows more slowly initially than for all the smaller values of F, and that the bandwidth decreases more gradually. This is likely because the criteria $F < 2$ is not satisfied, meaning that there exists within the gain bandwidth a sideband frequency common to all the modes at frequency $\bar{\omega}_c = \pm 2\pi$ (using equation (3.54)) and in fact this is clearly visible in Figure 3.34. This figure shows a comparison, on both logarithmic and linear scales (note the expanded y-axis on the linear plot), of normalised spectra at saturation, for random delays with $\langle \bar{\delta} \rangle = 48.0$ and prime delays with $F = 4.0$. It is confirmed on this direct comparison that apart from the residual sidebands at $\bar{\omega}_c = \pm 2\pi$ the prime sequence has been more effective at suppressing the sideband frequencies either side of the resonance.

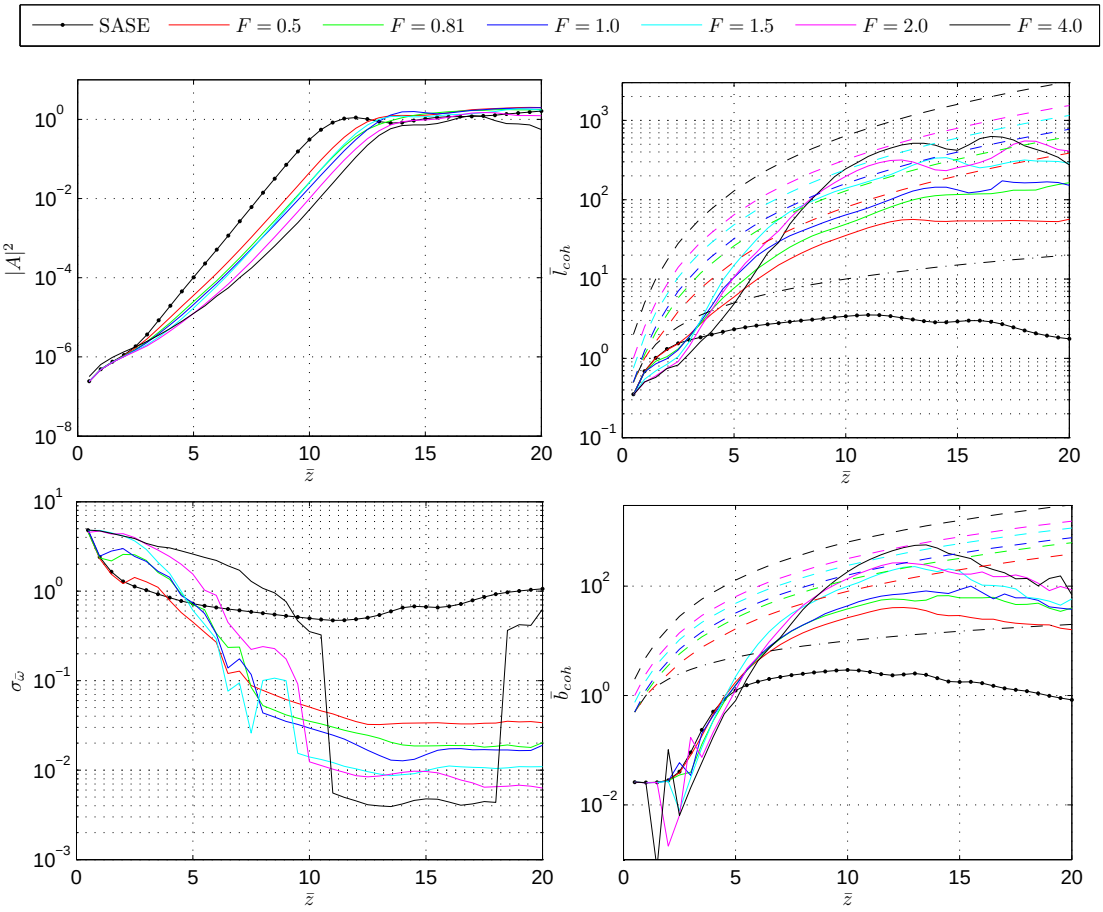

Figure 3.27: Prime number delays. The evolution in $\bar{z}$ of $|A|^2$, $\bar{l}_{\mathrm{coh}}$, $\sigma_{\bar{\omega}}$ and $\bar{b}_{\mathrm{coh}}$. Similarly to the case with random chicane delays, the radiation and bunching coherence lengths at saturation exceed that of the SASE control case by up to two orders of magnitude, with a corresponding reduction in bandwidth.

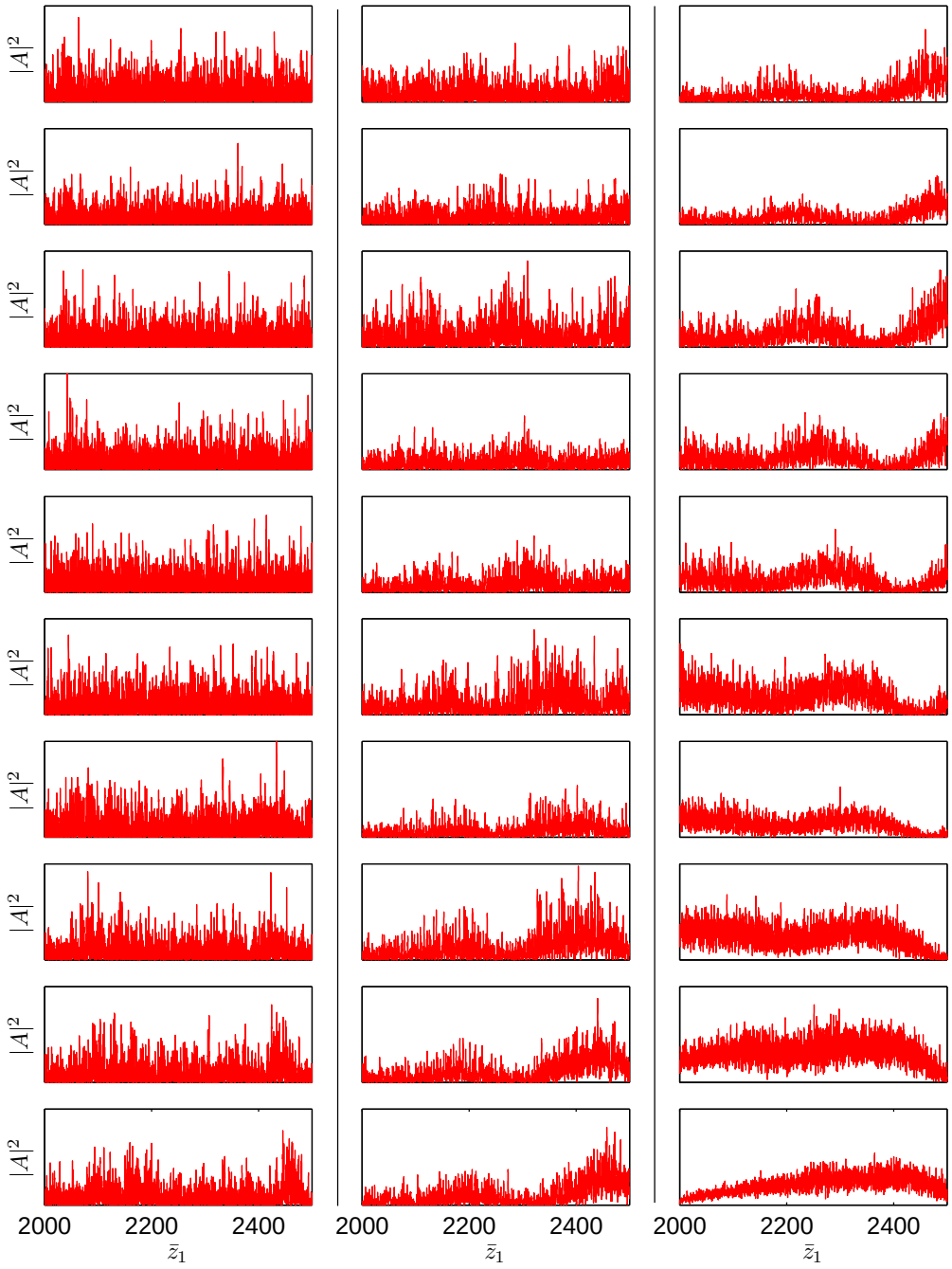

Figure 3.28: Prime number delays with scaling factor $F = 4.0$: normalised intensity profiles in steps of $\bar{z} = 0.5$ from $\bar{z} = 0.5$ to $\bar{z} = 15.0$. Similarly to the case with random chicane delays, by saturation at $\bar{z} = 14.0$ the pulse profile has become a slowly varying envelope with some residual noise.

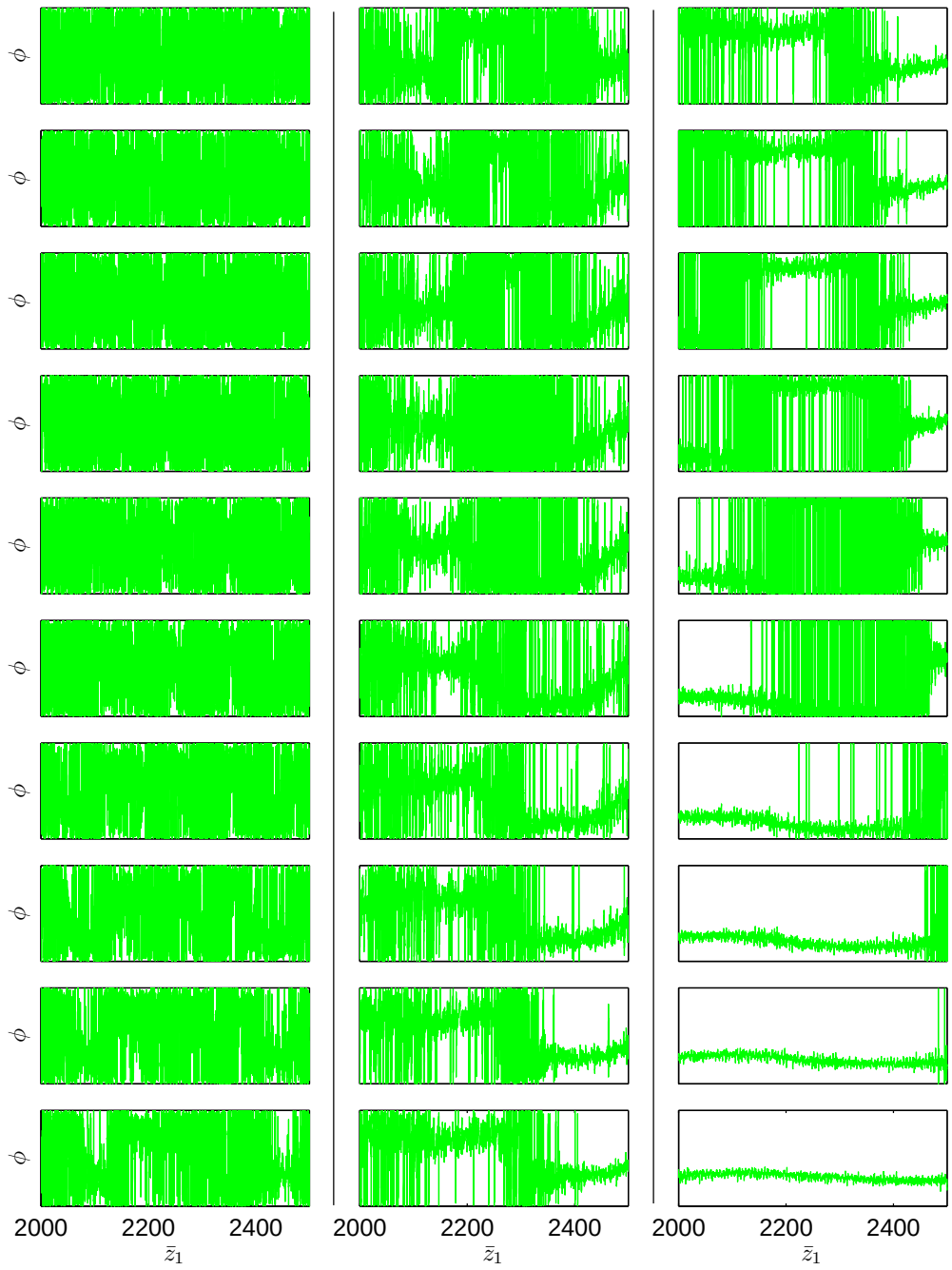

Figure 3.29: Prime number delays with scaling factor $F = 4.0$: normalised phase profiles in steps of $\bar{z} = 0.5$ from $\bar{z} = 0.5$ to $\bar{z} = 15.0$. The results are qualitatively similar to the case with random chicane delays—by saturation a smoothly varying phase has evolved from the initial noise, indicating good longitudinal coherence.

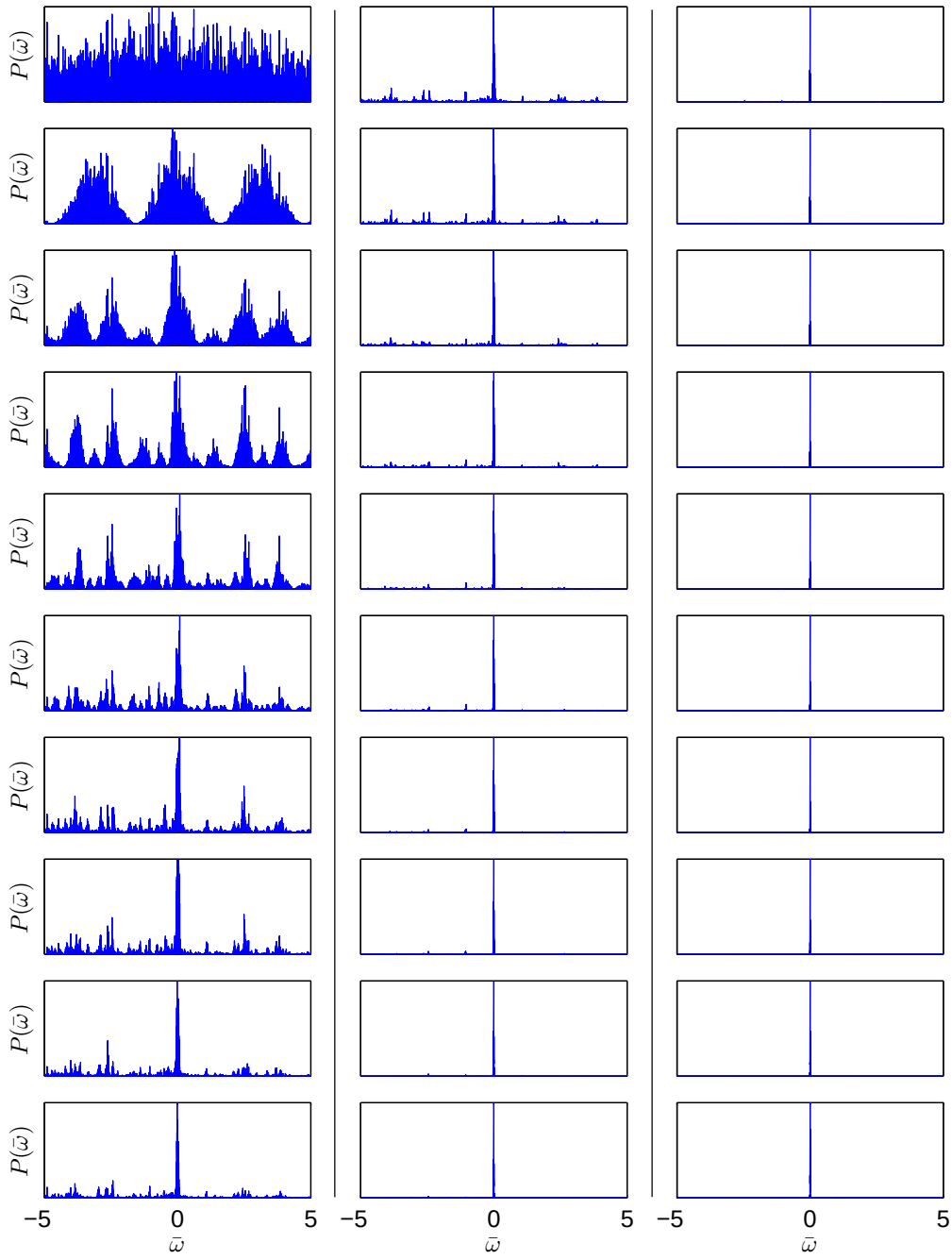

Figure 3.30: Prime number delays with scaling factor $F = 4.0$: normalised spectra in steps of $\bar{z} = 0.5$. The evolution of the spectrum is qualitatively different from the case with random number delays shown in Figure 3.25. For small $\bar{z}$ the sideband modes are much wider becasue in this delay sequence the initial delays are small then increase from one chicane to the next, whereas the random delays can be large at small $\bar{z}$ giving more closely spaced and narrower sidebands.

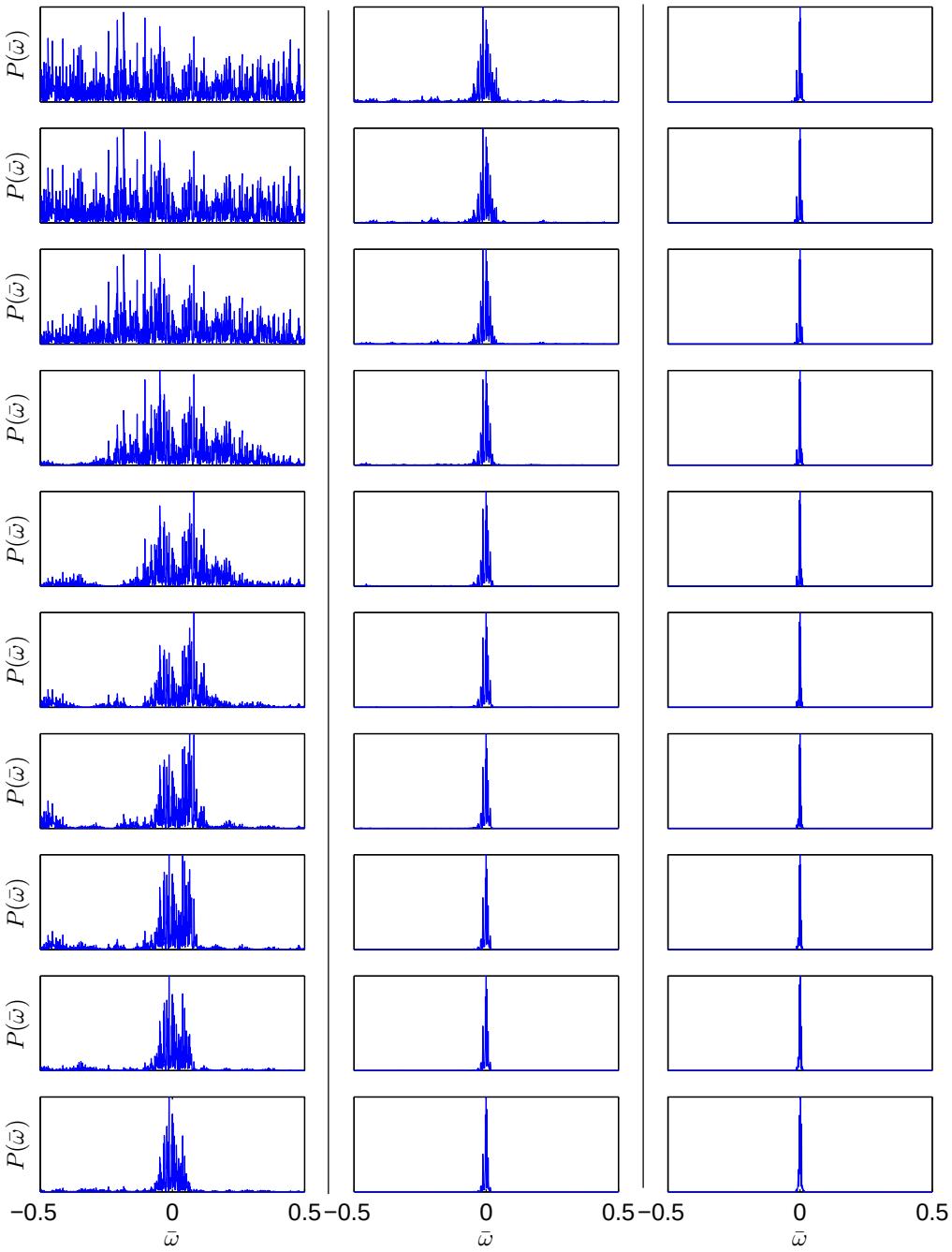

Figure 3.31: Prime delays with scaling factor $F = 4.0$: normalised spectra in steps of $\bar{z} = 0.5$. The $\bar{\omega}$ axis is expanded by a factor of 10 compared to Figure 3.30

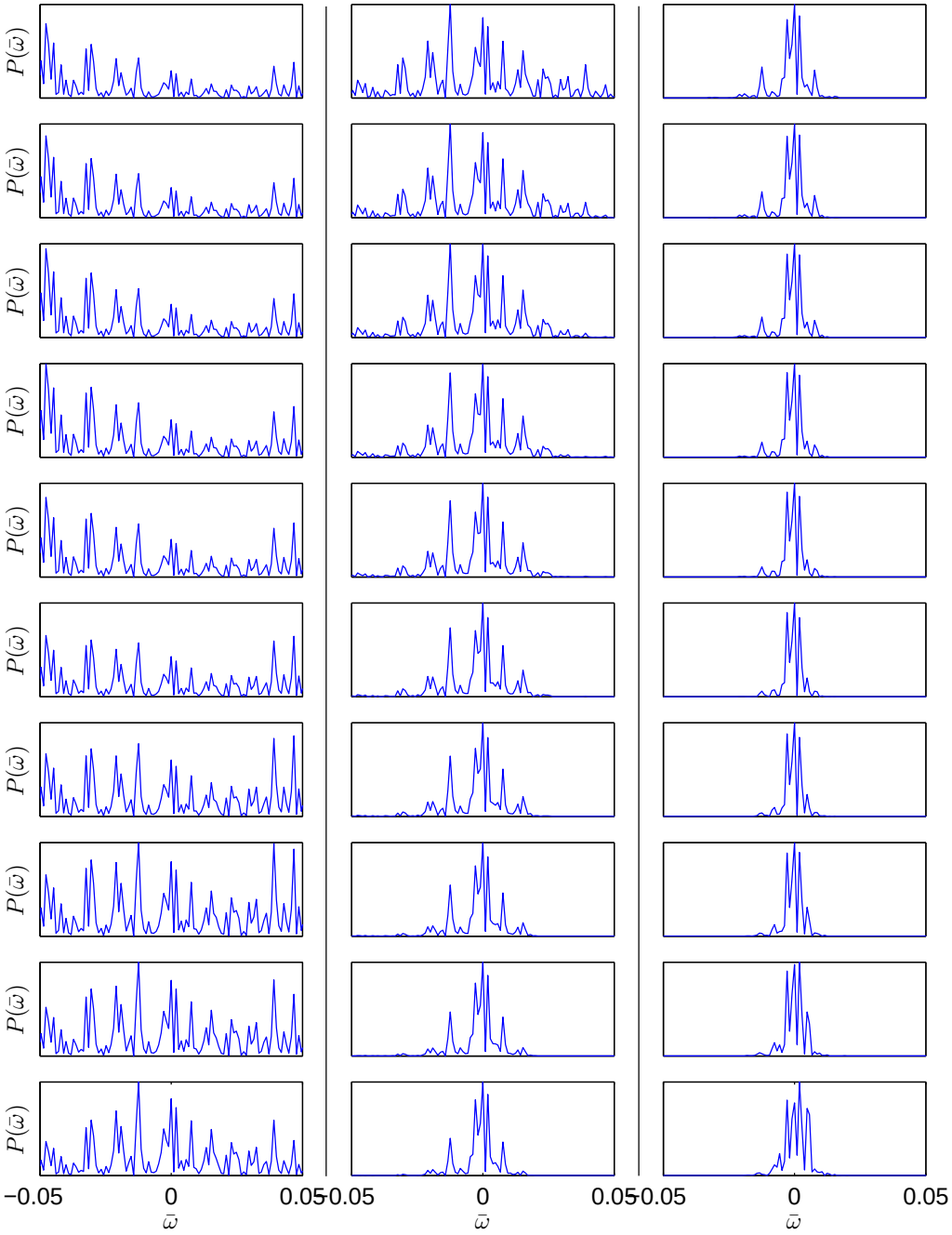

Figure 3.32: Prime delays with scaling factor $F = 4.0$: normalised spectra in steps of $\bar{z} = 0.5$. The $\bar{\omega}$ axis is expanded by a factor of 100 compared to Figure 3.30

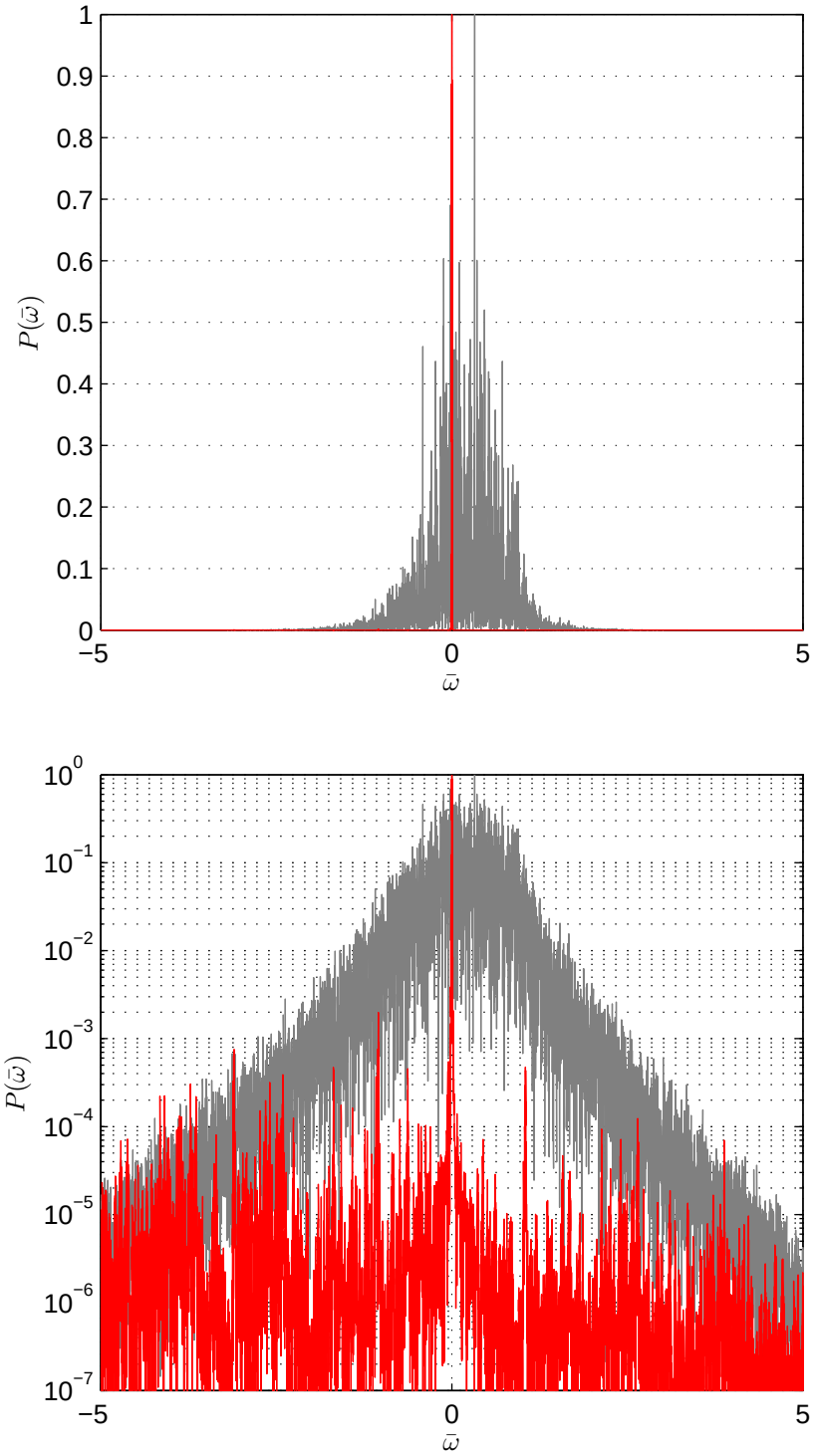

Figure 3.33: Comparison of normalised spectra at saturation, for SASE control (grey) and prime delays with scaling factor $F = 4.0$ (red).

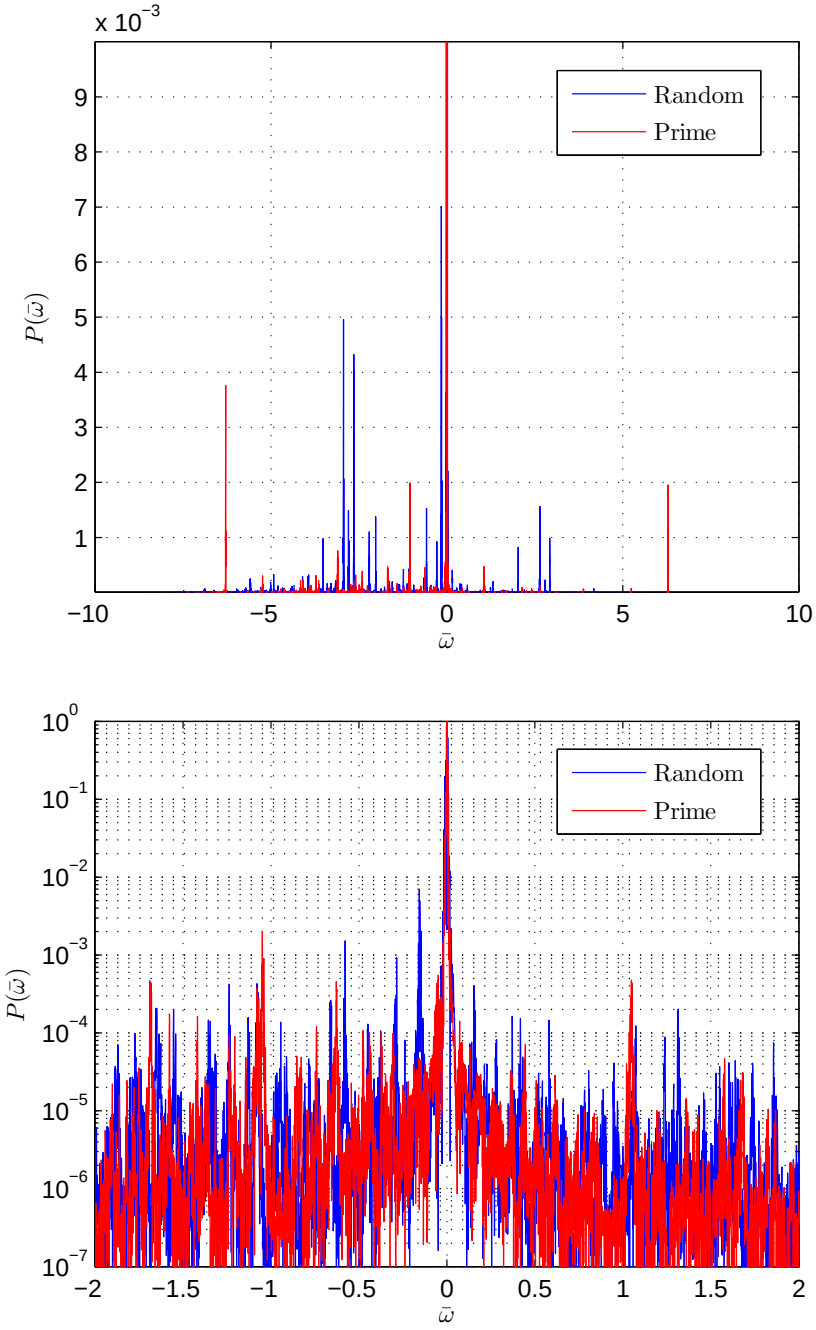

Figure 3.34: Comparison of normalised spectra at saturation, for random delays with $\langle\bar{\delta}\rangle = 48.0$ (blue) and prime delays with $F = 4.0$ (red). Apart from the residual sidebands at $\bar{\omega}_c = \pm 2\pi$ the prime number sequence has been more effective at suppressing the sideband frequencies either side of the resonance.

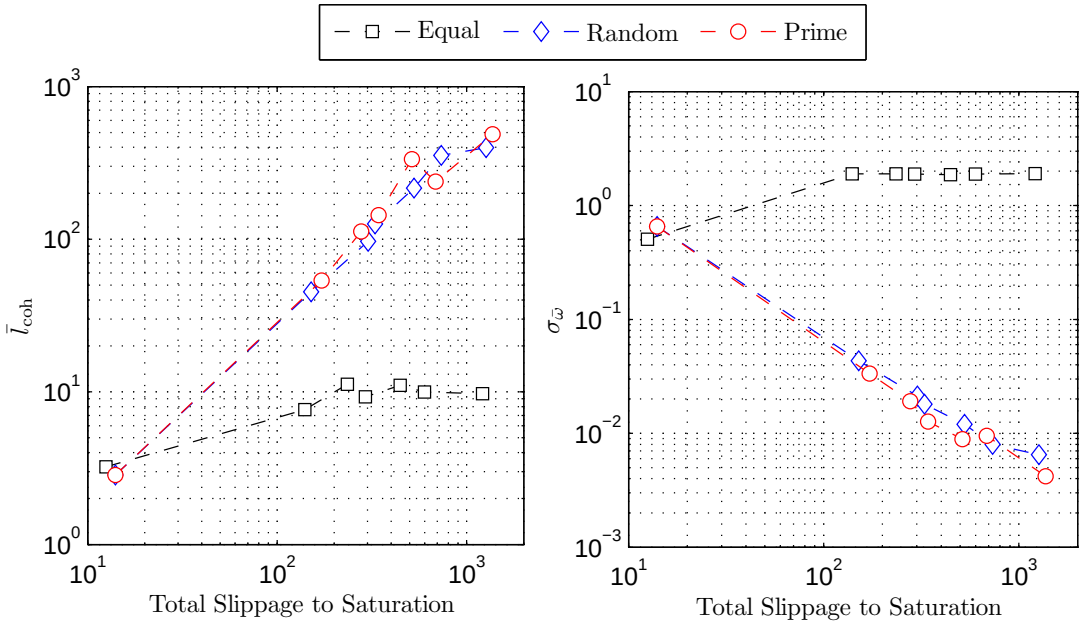

Figure 3.35: Comparison of effect of equal chicane delays, random chicane delays and prime number sequence delays, showing the radiation coherence length $\bar{l}_{\mathrm{coh}}$ and rms bandwidth $\sigma_{\bar{\omega}}$ at intensity saturation as a function of the total applied slippage $\bar{S} = \sum \bar{s}_n$.

3.6.5 Comparison of Chicane Delay Sequences

Three different chicane delay sequences have been applied, equal delays in Section 3.6.2, delays randomised about a mean in Section 3.6.3 and delays based on a prime number sequence in Section 3.6.4. It was seen that the effect of equal delays on the longitudinal coherence was very limited, although this technique might be useful for obtaining a very broad bandwidth FEL output comprising evenly-spaced discrete frequencies. To really improve the longitudinal coherence significantly over SASE, and give a corresponding reduction in bandwidth, it was necessary to make the delays non-constant which in effect filters the radiation by prohibiting the growth of the sideband frequencies. The efficacy of random delays and prime delays is in fact quite similar—Figure 3.35 shows a comparison of effect of equal delays, random delays, or prime number sequence delays, showing the radiation coherence length $\bar{l}_{\mathrm{coh}}$ and rms bandwidth $\sigma_{\bar{\omega}}$ at intensity saturation as a function of the total applied slippage $\bar{S} = \sum \bar{s}_n$. It is seen that for random and prime delays the coherence length increases in proportion to the total slippage. It should be noted that there has also been a proposal for a delay sequence increasing

geometrically in powers of 2 [51]. Although no direct comparison has been made with the delay sequences investigated here, it is postulated by the author that such a sequence may not be as effective since it would support, and not therefore efficiently cancel, some common sideband frequencies.

For the delay sequences using randomised and prime number delays, linear fits to $\bar{l}_{\rm coh}$ vs $\bar{S}$ are

$$\bar{l}_{\rm coh}\,(\text{Random}) = 0.345\,\bar{S} + 13 \tag{3.57}$$

and

$$\bar{l}_{\rm coh}\,(\text{Prime}) = 0.357\,\bar{S} + 24 \tag{3.58}$$

and similarly, linear fits to $1/\sigma_{\bar{\omega}}$ vs $\bar{S}$ give

$$\frac{1}{\sigma_{\bar{\omega}}}(\text{Random}) = 0.126\,\bar{S} + 10 \tag{3.59}$$

and

$$\frac{1}{\sigma_{\bar{\omega}}}(\text{Prime}) = 0.169\,\bar{S} + 7. \tag{3.60}$$

If the intercepts are ignored then the gradients give

$$\bar{l}_{\rm coh}(\text{Random}) \simeq \frac{\bar{S}}{3}, \quad \bar{l}_{\rm coh}(\text{Prime}) \simeq \frac{\bar{S}}{3} \tag{3.61}$$

and

$$\sigma_{\bar{\omega}}(\text{Random}) \simeq \frac{8}{\bar{S}}, \quad \sigma_{\bar{\omega}}(\text{Prime}) \simeq \frac{6}{\bar{S}} \tag{3.62}$$

and combining these to eliminate $\bar{S}$ then gives

$$\bar{l}_{\rm coh}\sigma_{\bar{\omega}}(\text{Random}) \simeq 2.6, \quad \bar{l}_{\rm coh}\sigma_{\bar{\omega}}(\text{Prime}) \simeq 2.0. \tag{3.63}$$

From these results, which are a very limited data set, the prime delay sequence generates a smaller bandwidth than random delays, but the coherence lengths are similar. More simulations are required to improve the statistical significance and confirm this analysis or otherwise. It is interesting to compare these final results to the theory of normal SASE, from which (using (2.214) and (2.235)) $\sigma_{\bar{\omega}} \simeq 0.5$ and (from (2.232)) $\bar{l}_{\rm coh} = 3.2$ giving

$$\bar{l}_{\rm coh}\sigma_{\bar{\omega}}(\text{SASE}) \simeq 1.6 \tag{3.64}$$

3.6.6 The Development of Longitudinal Coherence

In this section the development of longitudinal coherence in the HB-SASE process is discussed and compared with the SASE control case. An example case is used for illustration—prime number delays with $F = 4.0$. This case is chosen as it is the example shown so far with the longest coherence length at saturation. Figure 3.36 shows the development of $\bar{l}_{\rm coh}$ and $\bar{b}_{\rm coh}$ for SASE and HB-SASE (Figure 3.36a), as well as these quantities normalised to the total accumulated slippage (Figure 3.36b). For SASE $\bar{l}_{\rm coh}$ initially develops rapidly, reaching half its saturation value by $\bar{z} = 3$, then increases much more gradually. By comparison, $\bar{l}_{\rm coh}$ for HB-SASE develops more slowly until $\bar{z} = 3$ and thereafter, just at the point where the SASE $\bar{l}_{\rm coh}$ increase slows down, the HB-SASE $\bar{l}_{\rm coh}$ starts to increase rapidly. Over the range $4 \leq \bar{z} \leq 8$ the growth is exponential. A linear fit to a plot of $\ln(\bar{l}_{\rm coh})$ vs $\bar{z}$ gives

$$\bar{l}_{\rm coh} = 0.059\, e^{(0.892\bar{z})} \tag{3.65}$$

and this is shown in Figure 3.37 with the numerical data. Over this range the coherence length increases from $\bar{l}_{\rm coh} = 2$ to $\bar{l}_{\rm coh} = 75$ before the rate starts to slow towards saturation. It should be noted that a similar period of exponential growth in $\bar{l}_{\rm coh}$ is observed in the simulations using random delays, so is not particular to the delay sequence and does not necessarily require delays that progressively increase.

Figure 3.36b shows that for SASE the coherence length is always growing *more slowly* than the slippage is accumulating, as indicated by the negative gradient of $\bar{l}_{\rm coh}/\bar{S}$ vs $\bar{S}$, whereas for HB-SASE and $\bar{z} > 4$ the coherence length is growing *more rapidly* than the accumulating slippage. This fundamental difference indicates that the mechanisms of the two cases are different. For SASE the radiation phase becomes locally defined early in the interaction and $\bar{l}_{\rm coh}$ saturates eventually at a value of $\simeq 3l_c$, just three times the slippage in a gain length. For HB-SASE the effect of the delays is to delocalise the interaction—before the radiation/electron interaction phase becomes fixed a delay of greater than a cooperation length is applied to shift the radiation to interact with a different section of the electron bunch with a different bunching phase, and the interaction starts afresh. This 'delocalises' the interaction. In this way the initial development of phase coherence is more gradual but because of the extended communication distance within the system the final coherence length can be far greater. It can be

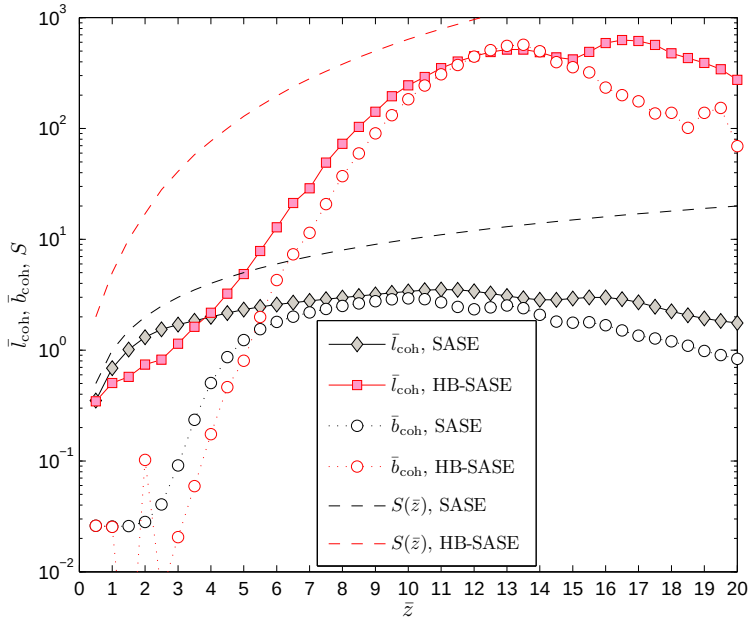

(a) Evolution of $\bar{l}_{\rm coh}$ and $\bar{b}_{\rm coh}$.

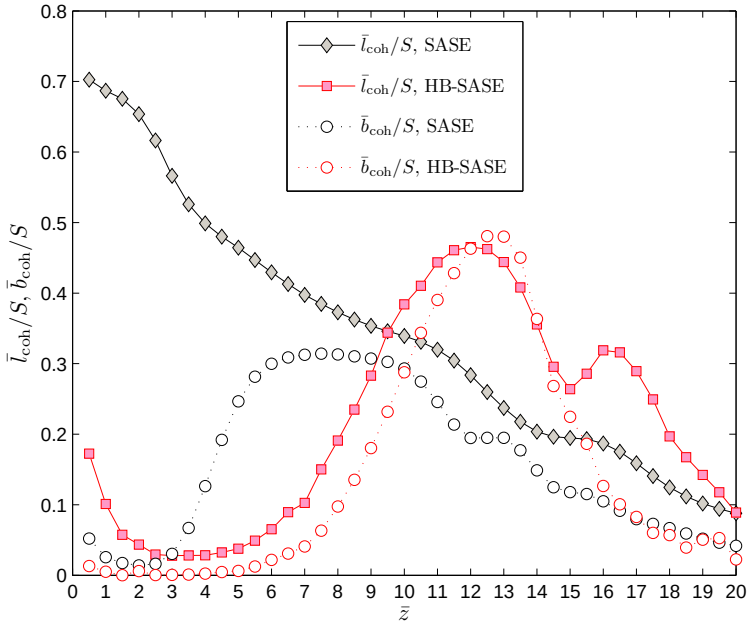

(b) Evolution of $\bar{l}_{\rm coh}$ and $\bar{b}_{\rm coh}$, normalised by the total accumulated slippage $S(\bar{z})$.

Figure 3.36: Comparison of coherence development with $\bar{z}$ for SASE and HB-SASE. For SASE $\bar{l}_{\rm coh}$ grows quickly at first then saturates at $\bar{l}_{\rm coh} \simeq 3$ because the radiation phase becomes fixed in the localised interaction. For HB-SASE the delays delocalise the interaction so the coherence length grows more slowly at first then starts to increase exponentially. The bunching coherence length is always less than the radiation coherence length, suggesting the coherence develops first in the radiation, and implying that the filtering of the radiation through the variable delays is an important driving factor in coherence development.

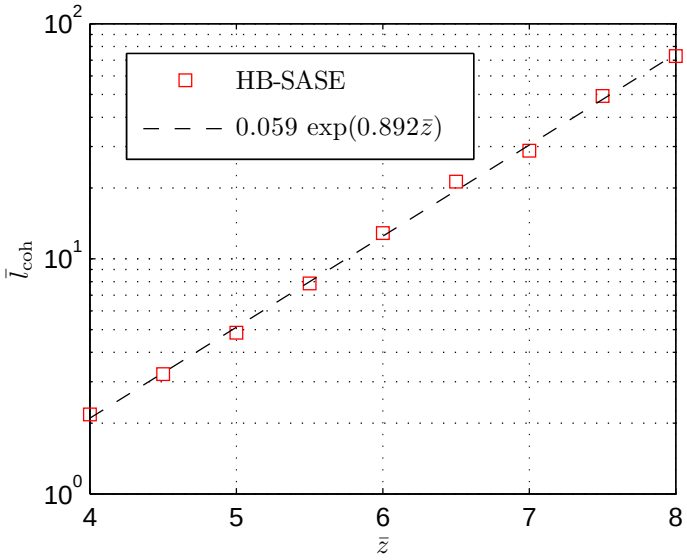

Figure 3.37: Exponential growth of radiation coherence length $\bar{l}_{\rm coh}$ over the range $4 \leq \bar{z} \leq 8$, with prime number delays and scale factor $F = 4.0$.

seen therefore that it is necessary for the undulator modules to be short, of $\bar{l} \leq 1$, so that the interaction can be repeatedly delocalised before the phase coherence of the radiation becomes established. A study is made of the effect of undulator module length in Section 3.7.1.

It is also interesting to look at the development of the longitudinal coherence in the electron beam bunching phase, as quantified by $\bar{b}_{\rm coh}$. For SASE $\bar{b}_{\rm coh}$ has an initial value, after the first undulator module, of much less than $\bar{l}_{\rm coh}$, and doesn't develop significantly for the first two gain lengths. It then increases rapidly but never catches up with $\bar{l}_{\rm coh}$. For HB-SASE the behaviour is qualitatively and quantitatively different—$\bar{b}_{\rm coh}$ develops noisily initially, with a value lower than $\bar{l}_{\rm coh}$, then increases rapidly until $\bar{b}_{\rm coh} > \bar{l}_{\rm coh}$ from $12 \leq \bar{z} \leq 14$. For most of the HB-SASE interaction (and all of the interaction for SASE) $\bar{l}_{\rm coh} > \bar{b}_{\rm coh}$, suggesting that the coherence is developing in the radiation then transferring to the electrons. This implies that the filtering of the radiation through the variable delays is an important driving factor in the development of longitudinal coherence in the complete coupled system, as seen in Section 3.6.2 where equal delays were shown to have a very limited effect in improving the coherence.

3.7 Numerical Parameter Range Study

3.7.1 Effect of Undulator Module Length

In this section the efficacy the HB-SASE as a function of the undulator module length is studied. The delay sequence used is based on prime numbers, as given by (3.50) and the scale factor is set to $F = \bar{s}_1/\bar{l} = 2$ to satisfy criteria (3.56). The shortest undulator module used is $\bar{l} = 0.5$, in common with the results shown in previous sections, and this is increased in steps of $\bar{l} = 0.25$ to maximum $\bar{l} = 2.0$. The number of modules required to reach saturation is inversely proportional to the module length, so to keep the total slippage constant the delays in the chicanes have to be increased accordingly. This is done, while maintaining $F = 2$, by starting the prime number sequence at an appropriately higher prime than $\mathbb{P}_1 = 2$.

Figure 3.38 shows the evolution of $|A|^2$, $\bar{l}_{\rm coh}$, $\bar{b}_{\rm coh}$ and $\sigma_{\bar{\omega}}$ with $\bar{z}$ for the different module lengths $\bar{l}$. Clearly as $\bar{l}$ increases the efficacy of HB-SASE decreases as shown by the decreasing coherence length and increasing bandwidth at saturation. Figure 3.39 shows the radiation spectra at saturation. For $\bar{l} \leq 0.75$ all the spectral power is close to resonance at $\bar{\omega} = 0$ and the sideband frequencies are not visible (on this linear scale). For $\bar{l} = 1.0$ there is a single visible sideband with normalised peak $P(\bar{\omega}) = 0.03$ which increases the calculated rms bandwidth. For $\bar{l} > 1$ the suppression of the sidebands is less effective and hence the bandwidths are significantly broader and the coherence length significantly shorter. Figure 3.40 shows coherence length $\bar{l}_{\rm coh}$ and the rms bandwidth $\sigma_{\bar{\omega}}$ at saturation, with each normalised to its respective SASE saturation value. The conclusion that can be drawn from this figure is that to obtain a two order of magnitude increase in $\bar{l}_{\rm coh}$ and consequent reduction in $\sigma_{\bar{\omega}}$ the undulator length should be $\bar{l} \leq 0.75$. For undulator lengths longer than this, and for this particular total slippage to saturation, the efficacy of HB-SASE is clearly reduced.

The degradation in performance for longer undulators is attributed to two main factors, although there may be others not yet investigated:

1. From the spectral perspective, the suppression of the sidebands becomes ineffective, as shown in the spectra in Figure 3.39. Reasons for this are–

    - As discussed in Section 3.5.2, the sidebands broaden for longer undulators. The delay sequence was scaled by changing the initial prime in

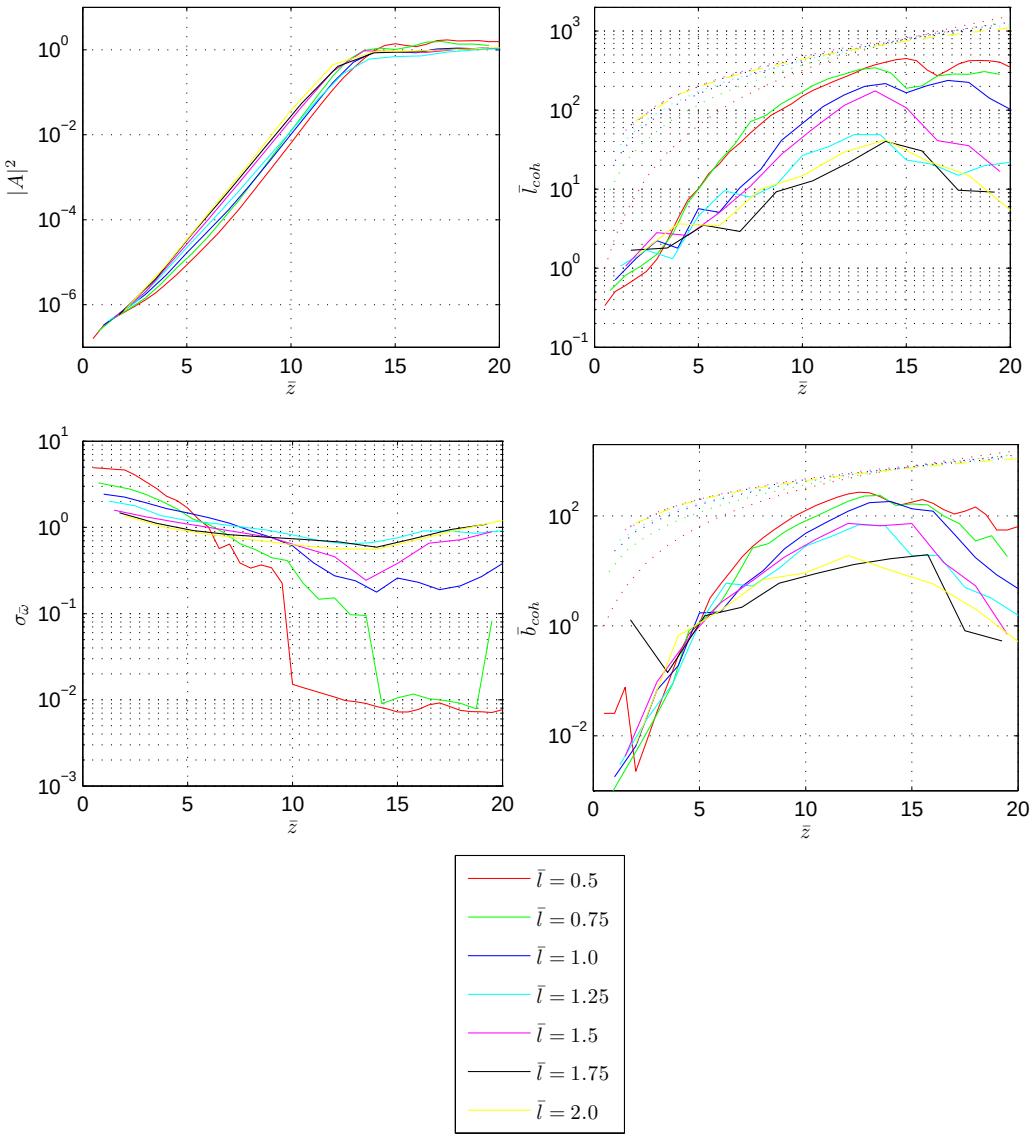

Figure 3.38: Prime delays, $F = 2.0$. Evolution of $|A|^2$, $\bar{l}_{\rm coh}$, $\bar{b}_{\rm coh}$ and $\sigma_{\bar{\omega}}$ with $\bar{z}$ for different module lengths $\bar{l}$. Clearly as $\bar{l}$ increases the efficacy of HB-SASE decreases as shown by the decreasing coherence length and increasing bandwidth at saturation.

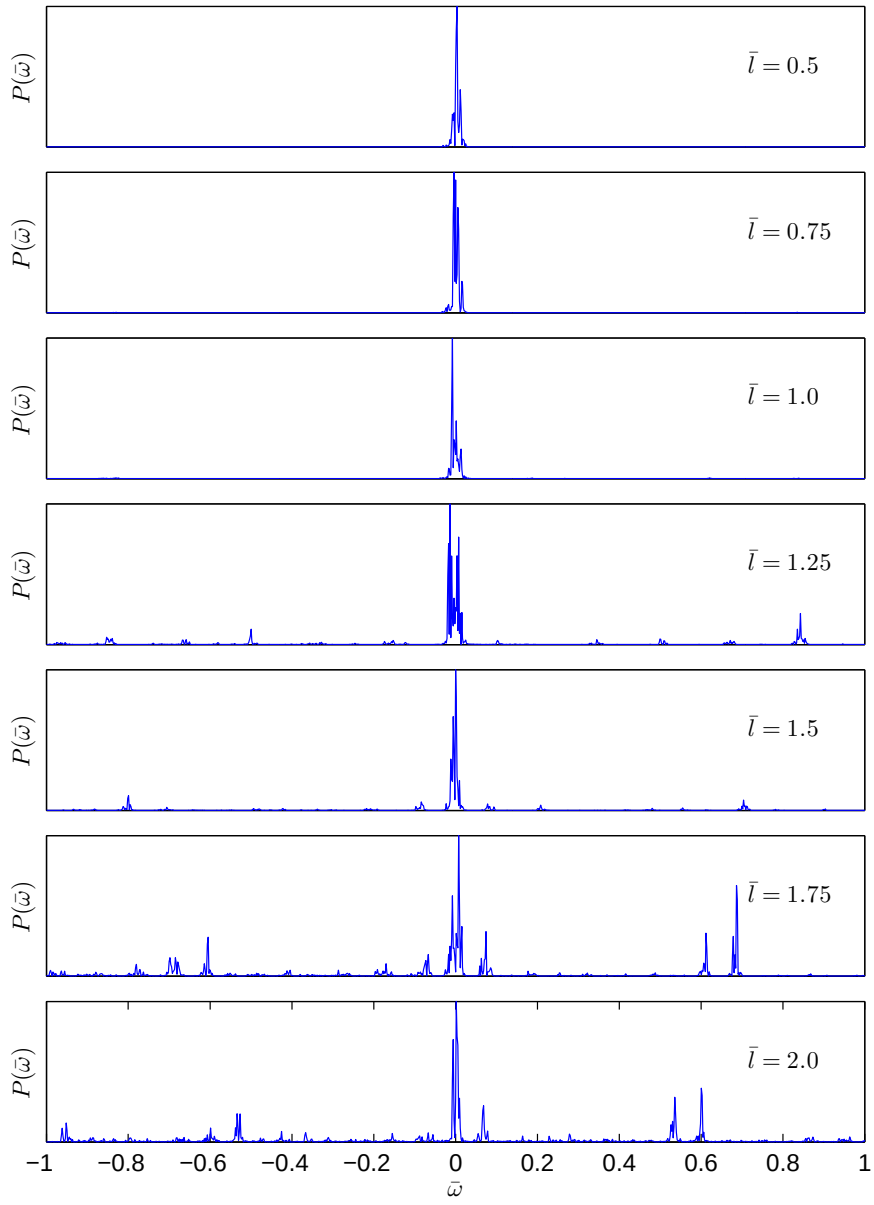

Figure 3.39: Prime delays, $F = 2.0$. Spectra at saturation for different module lengths $\bar{l}$. As the undulator modules become longer the suppression of the sidebands becomes less effective increasing the bandwidth and reducing the radiation coherence length.

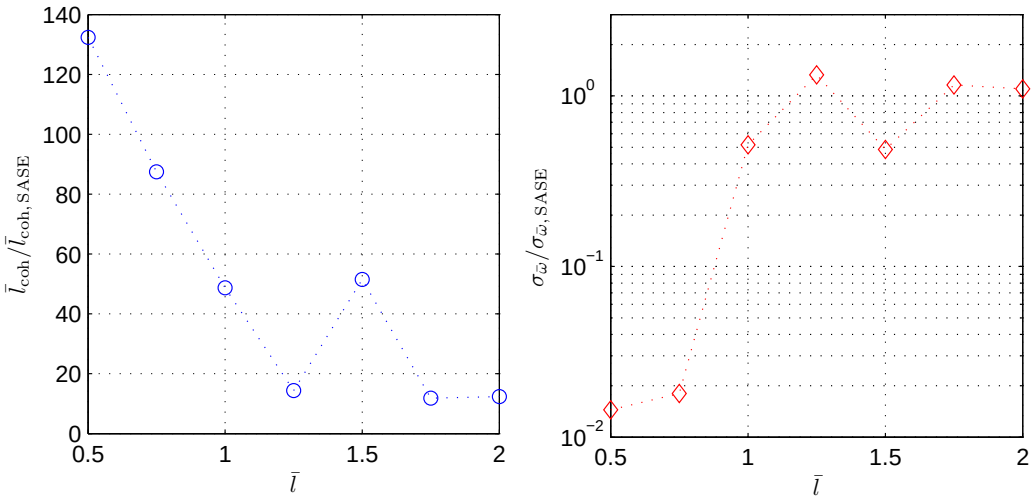

Figure 3.40: Prime delays, $F = 2.0$. Left: coherence length $\bar{l}_{\mathrm{coh}}$ at saturation, normalised to the SASE coherence length at saturation, as a function of module length $\bar{l}$. Right: rms bandwidth $\sigma_{\bar{\omega}}$ at saturation, normalised to the SASE bandwidth at saturation, as a function of module length $\bar{l}$.

the sequence, hence for longer undulators the range of delays becomes compressed so the frequencies of the supported sidebands are closer together. Taken together these two effects degrade the efficiency of the sideband suppression.

- With shorter undulators and more delays the sidebands are amplified less and filtered more frequently.

2. From the temporal perspective, as discussed in Section 3.6.6, it is necessary to delocalise the interaction frequently to prevent the phase of the radiation becoming fixed and allow it to continue to evolve.

Further study is required of this topic and will be important for any practical implementation of HB-SASE.

3.7.2 Effect of Longitudinal Chicane Dispersion

The results presented so far have been for isochronous chicanes with longitudinal dispersion factor $D = 0$. Isochronous chicanes are feasible, but require extra quadrupoles which increase their length. However, compact chicanes with very low dispersion are feasible and can also be designed with the ability to provide a variable delay [48, 49]. In this section an investigation is made of the effect of adding longitudinal dispersion over the range $0 \leq D \leq 1$ where to recap $D = 1$ represents a chicane with 5/3 times the dispersion of a standard 4-dipole chicane as described in Section 3.2.

There is already some longitudinal dispersion in the system, even with $D = 0$, due to the FEL undulators which are just a series of dipole magnets. In fact this dispersion is required by the FEL interaction—as the electron beam becomes modulated in energy within the FEL undulators, the dispersion starts to convert the energy modulation into a density modulation or a bunching at the FEL wavelength. As seen from equation (2.133) the rate of change of phase depends only on the electron energy. The energy modulation grows as the FEL process continues until just prior to saturation the beam becomes fully bunched and emits most strongly. At this point the rms energy spread reaches its maximum of $\sigma_\gamma/\gamma_0 \simeq \rho$.

If the chicanes add additional dispersion the bunching process will be affected by the chicanes—for a small energy modulation at the start of the interaction the bunching process will be enhanced leading to stronger emission and as the energy modulation grows the chicanes may act to 'overbunch' the electrons just prior to saturation, damping somewhat the radiation emission process just at the point it should be strongest.

An estimate can be made of the maximum dispersion parameter such that a single chicane does not overbunch the FEL as the field intensity approaches saturation. Restating equation (3.2), the electron phase evolves in the chicane as

$$\theta_i \rightarrow \theta_i + \bar{D} p_i. \tag{3.66}$$

therefore the relative phase change after the chicane $\Delta\theta$ between two electrons separated in energy by Δp is

$$\Delta\theta = \bar{D}\Delta p \tag{3.67}$$

For the chicane to retain the bunching in the electron beam the requirement is that the relative phase change between the highest and lowest energy electrons

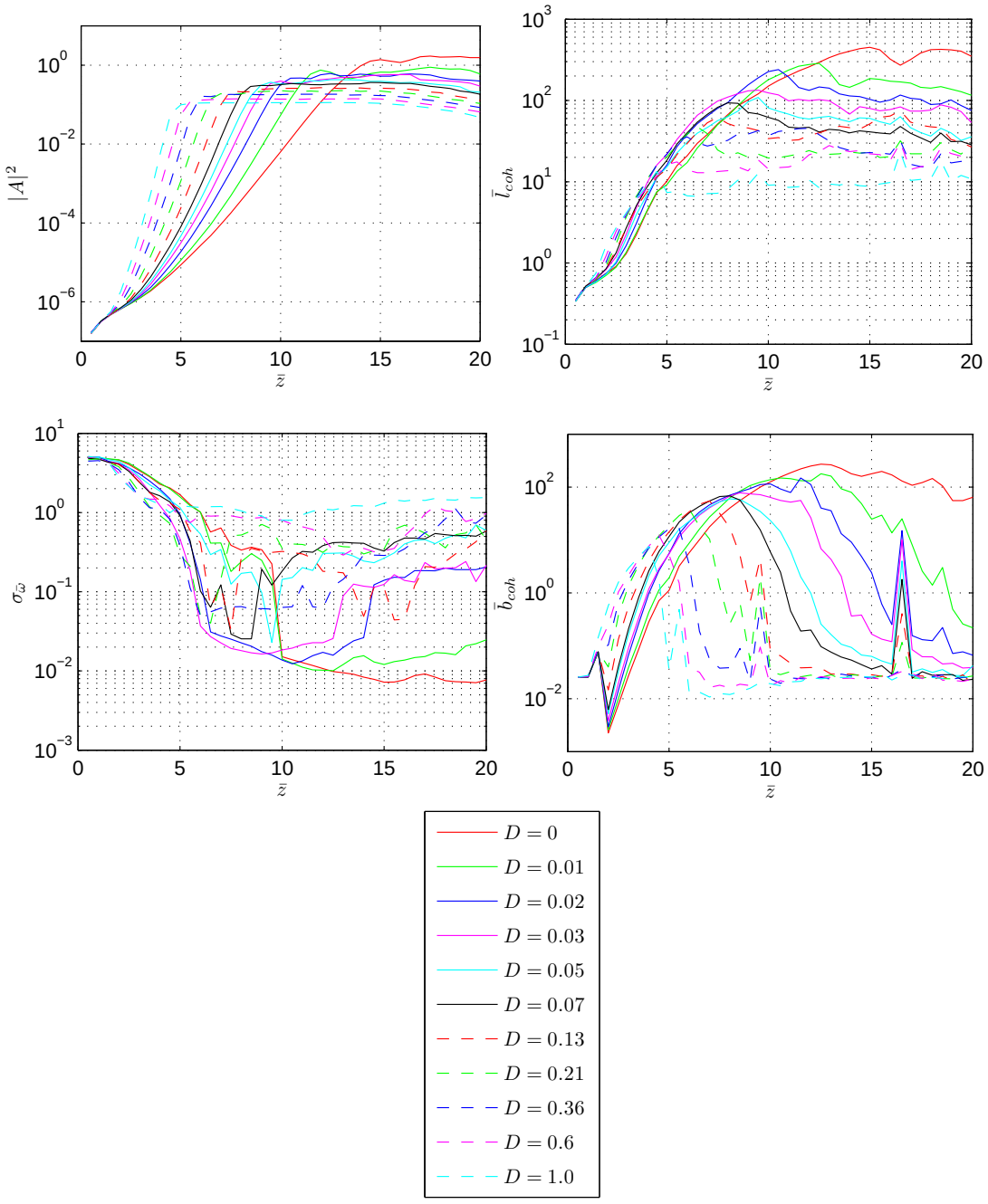

Figure 3.41: Prime delays, $F = 2.0$. Evolution of $|A|^2$, $\bar{l}_{\rm coh}$, $\bar{b}_{\rm coh}$ and $\sigma_{\bar{\omega}}$ with $\bar{z}$ for a range of dispersion parameter D. As D increases the power growth rate increases and the saturation length decreases. The radiation coherence length saturates at the same position as the power—after saturation the chicances debunch the electrons and the radiation/electron system decouples.

should be

$$\Delta\theta \leq \pi \tag{3.68}$$

which gives a limit on $\bar{D}$ of

$$\bar{D} \leq \frac{\pi}{\Delta p} \tag{3.69}$$

and therefore using (3.7)

$$\frac{5}{3}\bar{\delta}_1 D \leq \frac{\pi}{\Delta p} \tag{3.70}$$

giving

$$D \leq \frac{3\pi}{5\Delta p\bar{\delta}_1}. \tag{3.71}$$

At saturation the energy spread induced by the FEL is approximately $\sigma_\gamma/\gamma_0 = \rho$ so from the scaling of p the full energy spread is $\Delta p \simeq 2$. Therefore, the requirement on scaled dispersion parameter D is

$$D \leq \frac{3\pi}{10\bar{\delta}_1} \simeq \frac{1}{\bar{\delta}_1}. \tag{3.72}$$

A set of simulations were performed with the delay sequence based on prime numbers and the scale factor $F = 2$ to satisfy criteria (3.56). The undulator module length was $\bar{l} = 0.5$ and the dispersion parameter was increased approximately logarithmically. Figure 3.41 shows the evolution of $|A|^2$, $\bar{l}_{\rm coh}$, $\bar{b}_{\rm coh}$ and $\sigma_{\bar{\omega}}$ with $\bar{z}$ for the different values of D. From Figure 3.41 it is seen that the growth rate increases as D increases, with saturation for $D = 1$ occurring at $\bar{z} = 5$ compared to $\bar{z} = 15$ for $D = 0$. The saturation power also decreases as D increases. The coherence length $\bar{l}_{\rm coh}$ grows with approximately the same rate independent of D, until approximately $\bar{z} = 5$. For each value of D, as the power saturates the coherence also saturates, and because the saturation length is shorter for increasing D the saturation coherence length is also shorter. At saturation the electron beam is fully bunched, with the coherence length in the bunching at its maximum value. Post saturation the dispersive chicanes start to debunch the electrons which stops the FEL interaction proceeding—the electrons and radiation become decoupled. As the bunching becomes degraded the bunching coherence length decays to its initial value, with a decay rate that is faster for larger D. The evolution of the radiation bandwidth proceeds in a similar way to the evolution of $\bar{l}_{\rm coh}$—it changes (reduces in this case) until the power saturates.

Figure 3.42 shows the radiation spectra at saturation. It is seen that the

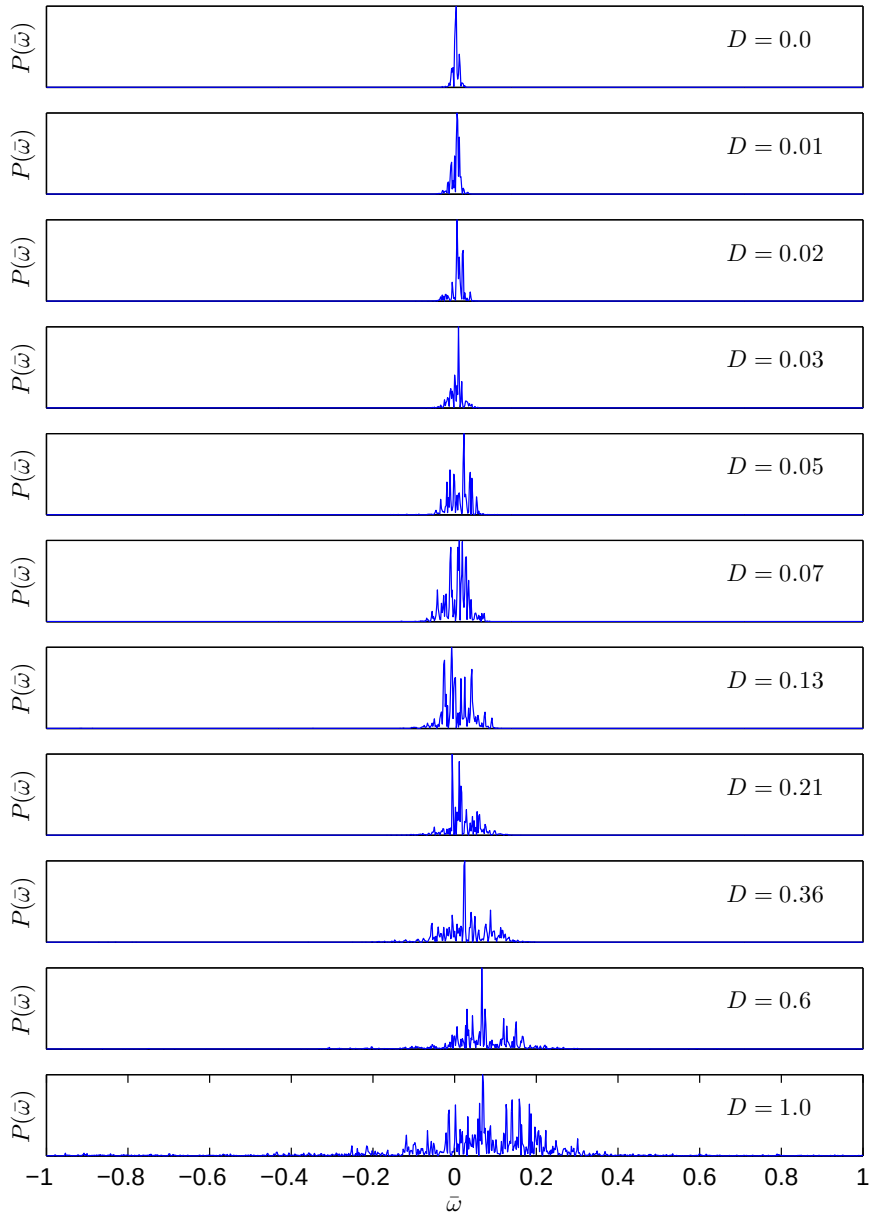

Figure 3.42: Prime delays, $F = 2.0$. Spectra at saturation for dispersion parameter increasing from $D = 0$ (isochronous chicanes) through $D = 0.6$ (standard 4-dipole chicane) to $D = 1$ (5/3 times the dispersion of a standard 4-dipole chicane). The suppression of the sidebands is effective, but the bandwidth around resonance becomes progressively broader as D increases.

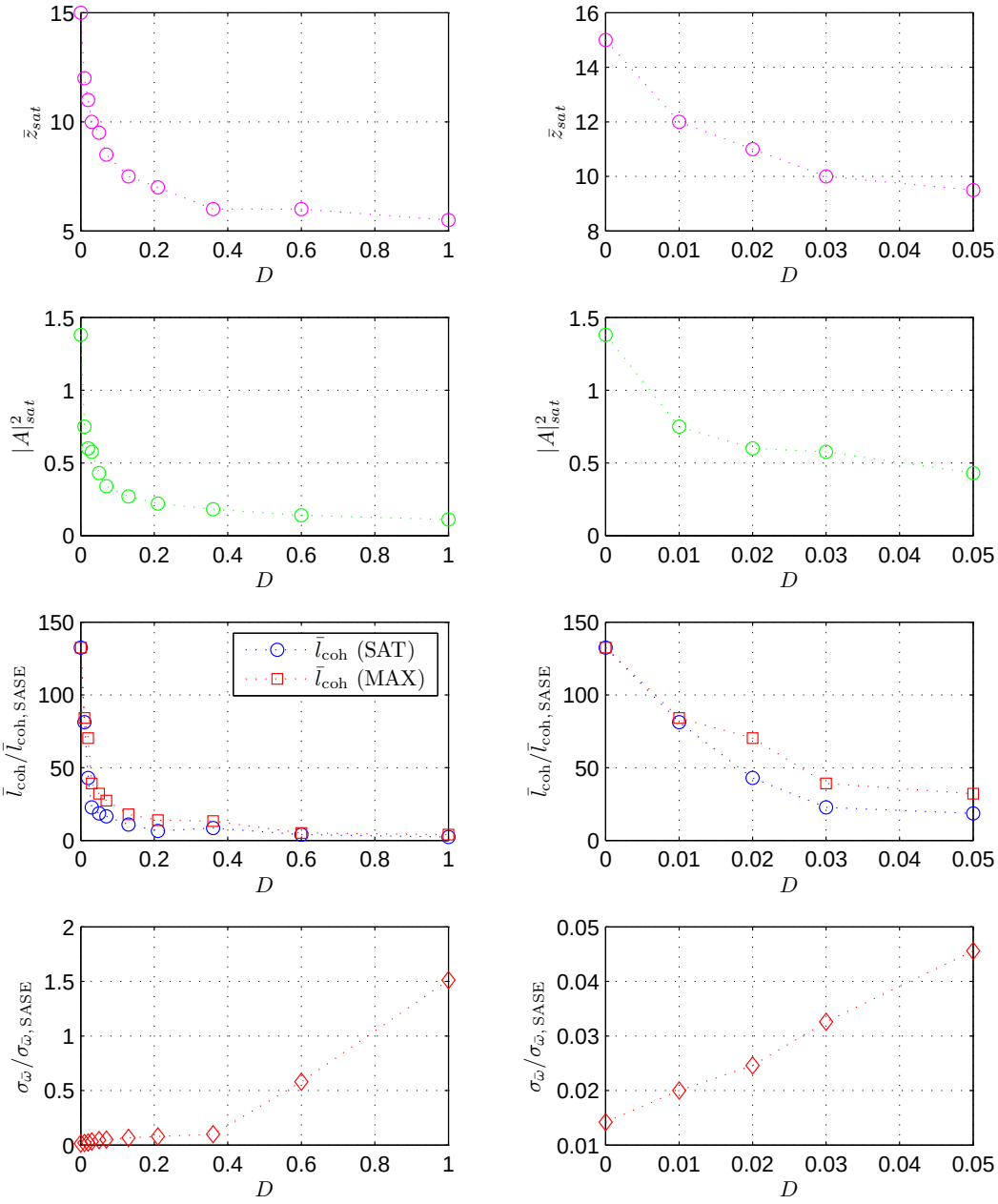

Figure 3.43: Prime delays, $F = 2.0$. Left column from top: saturation length $\bar{z}$ vs D; saturation intensity $|A|^2_{\rm sat}$ vs D; coherence length at $\bar{z}_{\rm sat}$ $\bar{l}_{\rm coh}$ (SAT) and maximum coherence length $\bar{l}_{\rm coh}$ (MAX), both normalised to the SASE coherence length at saturation, vs D; radiation bandwidth $\sigma_{\bar{\omega}}$ at $\bar{z}_{\rm sat}$, normalised to the SASE saturation bandwidth, vs D. Right column from top: same as left column but expanded D axis.

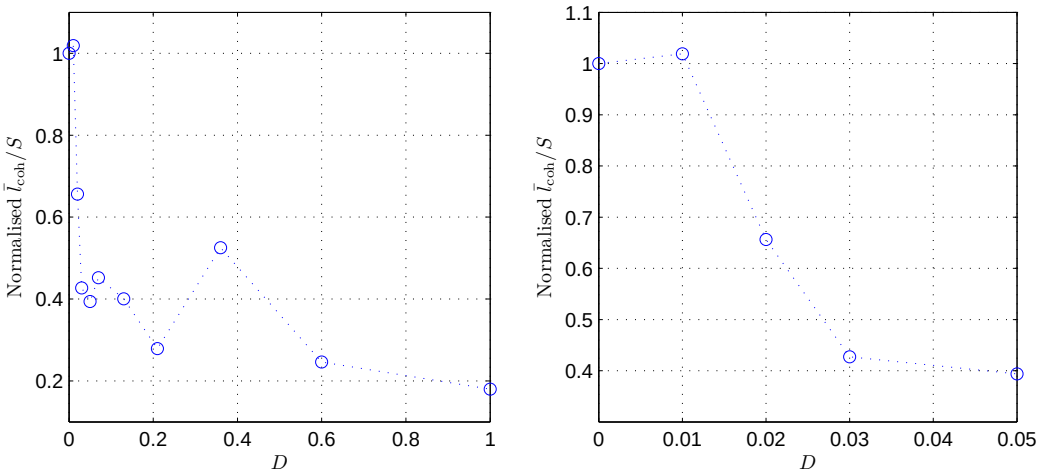

Figure 3.44: Prime delays, $F = 2.0$. Coherence length $\bar{l}_{\rm coh}$ at saturation divided by the total slippage to saturation $\bar{S}$, as a function of dispersion parameter D. The results are normalised to the case for $D = 0$. The right hand plot is the same data as the left hand plot but with the scale for D enlarged.

suppression of the sidebands is effective, but that the bandwidth becomes progressively broader as D increases. Figure 3.43 shows a summary of data extracted from Figure 3.41: the intensity saturation length $\bar{z}_{\rm sat}$ *vs* D; the saturation intensity $|A|^2_{\rm sat}$ *vs* D; the coherence length at $\bar{z}_{\rm sat}$ and the maximum coherence length, both normalised to the SASE coherence length, *vs* D; the radiation bandwidth $\sigma_{\bar{\omega}}$ at $\bar{z}_{\rm sat}$, normalised to the SASE saturation bandwidth, *vs* D. For the simulations shown here the delay imposed at saturation for $D = 0$ is $\bar{\delta}_1 \simeq 60$. The criterion (3.72) that an individual chicane does not overbunch the electrons at saturation gives the requirement $D \leq 0.016$. From Figure 3.43 it can be seen that for $D = 0.01$, compared to $D = 0$, there is already a decrease in saturation power, saturation length and coherence length and an increase in bandwidth, and interpolating to $D = 0.016$ $\bar{z}_{\rm sat}$ has decreased to about 75% of its value for $D = 0$, $|A|^2_{\rm sat}$ has decreased to around 50%, $\bar{l}_{\rm coh}$ has decreased to around 50% and the bandwidth has increased by around 50%. This means the efficacy of HB-SASE with D set to the threshold (3.72) has approximately halved compared to the case with isochronous chicanes.

The degradation is partly because as D increases $\bar{z}_{\rm sat}$ decreases so the total slippage also decreases. If the coherence length is divided by the total slippage to saturation $\bar{S}$ the decay with D is not as rapid. This is shown in Figure 3.44 where the results are normalised to those at $D = 0$. It is seen that for the

threshold $D = 0.016$, $\bar{l}_{\rm coh}/\bar{S}$ is now 80% of its value at $D = 0$ and doesn't decay to 50% until $D \simeq 0.025$. However, the coherence length is reduced more than the reduction in slippage alone can account for because the enhanced growth rate due to the bunching effect of the chicanes increases the *effective* scaled length of each undulator, and as shown in the previous section, this also degrades the HB-SASE performance.

To summarise, longitudinal dispersion enhances the bunching at the start of the FEL interaction, then degrades it approaching saturation so decoupling the electrons and radiation. The dispersion enhances the bunching, decreasing the saturation length and the total slippage hence the coherence length is reduced. The enhanced growth rate may also increase the effective scaled length of each undulator further degrading the performance. Longitudinal dispersion does not appear to affect the process of removing the sideband frequencies which works effectively for all values of D up to $D = 1$.

The fact that longitudinal dispersion ($D > 0$) enhances the bunching at the start of the interaction but degrades the performance close to saturation suggests that D could be varied for different sections of the FEL undulator to optimise the overall performance. This may be an interesting topic for future research.

3.8 Practical Examples

3.8.1 Hard X-Ray HB-SASE

An example is now shown of an HB-SASE simulation of a hard X-ray FEL. The parameters used are typical of current FEL designs: resonant wavelength λ_r=0.13 nm, beam energy E=14.7 GeV, peak current $I_{\rm pk} = 3000$A, bunch charge $Q = 10$ pC, undulator period $\lambda_w = 30$mm and $\rho = 4.17 \times 10^{-4}$. The same simulation code as in the previous sections is used, the parameters converted into the universal scaling, and the results scaled back into S. I. units for plotting. The delay sequence is based on prime numbers and scaled via F such that at saturation the total slippage is the FWHM electron bunch length. This gives $F = 1.08$. The delays are isochronous so that $D = 0$. The undulator modules have length $\bar{l} = 0.5$ equivalent to $L_u = 2.85$m. An equivalent SASE simulation was done to compare the performance of HB-SASE.

Figure 3.45 shows the pulse profiles, phase profiles and spectra of SASE and HB-SASE at saturation. The efficacy of HB-SASE is clearly demonstrated—the SASE pulse is a chaotic sequence of phase uncorrelated spikes whereas the HB-SASE pulse is near single spike with slowly varying phase. For SASE, the coherence time $t_{\rm coh} = l_{\rm coh}/c = 0.27$fs, in excellent agreement with (2.230). The rms bandwidth $\sigma_\lambda/\lambda = 4.3 \times 10^{-4} \simeq \rho$, giving $\sigma_\omega t_{\rm coh} = 1.68$. For HB-SASE, $t_{\rm coh} = 7.0$ fs and $\sigma_\lambda/\lambda = 2.0 \times 10^{-5}$, giving $\sigma_\omega t_{\rm coh} = 2.03$. The FWHM pulse durations and bandwidths at saturation give time-bandwidth products $\Delta\nu\Delta t = (1/\lambda)(\Delta\lambda/\lambda)c\Delta t = 32$ for SASE and $\Delta\nu\Delta t = 0.85$ for HB-SASE. For comparison, a transform limited gaussian pulse has time-bandwidth product $\Delta\nu\Delta t = 0.44$, so it is seen that the HB-SASE output pulse is quite close to transform limited.

3.8.2 Soft X-ray HB-SASE

An example is shown of HB-SASE applied to a soft X-ray FEL. The parameters are resonant wavelength λ_r=1.24 nm, beam energy E=2.25 GeV, peak current $I_{\rm pk} = 1200$A, bunch charge $Q = 200$ pC, undulator period $\lambda_w = 30$mm and FEL parameter $\rho = 8.8 \times 10^{-4}$. These parameters are typical of a soft X-ray FEL. The sequence of prime delays, with $D = 0$, is again set so that at saturation the total slippage is equal to the FWHM electron bunch length, giving $F = 1.046$. The undulator modules have length $\bar{l} = 0.5$ equivalent to a real length $L = 1.35$m.

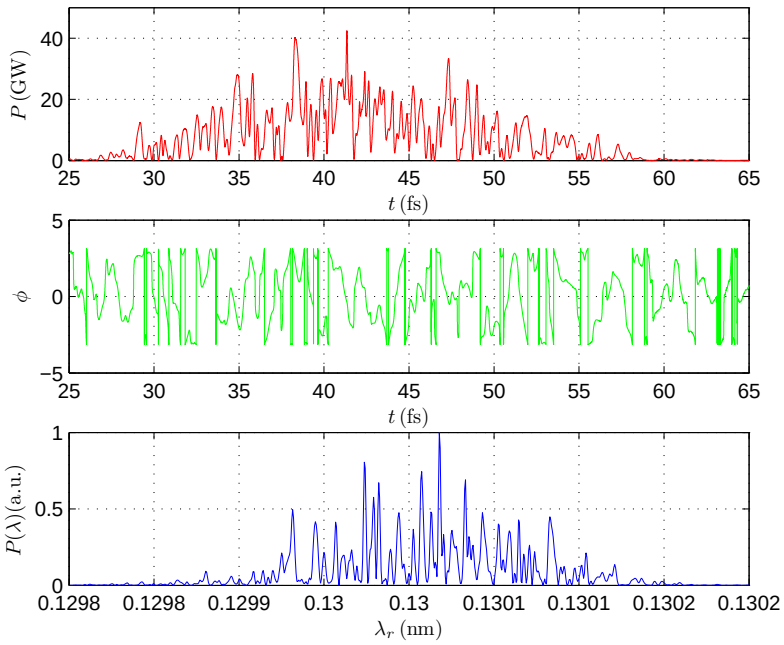

(a) SASE Control Case.

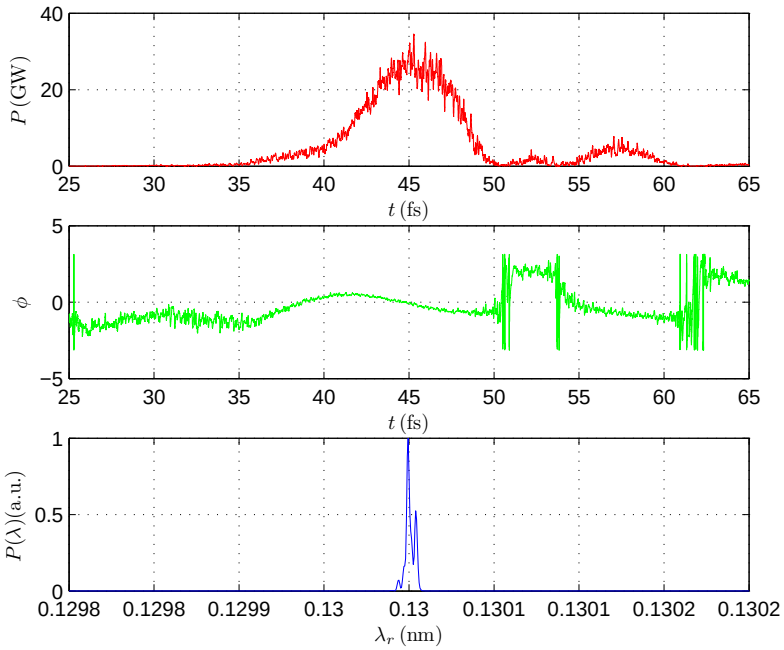

(b) HB-SASE.

Figure 3.45: Hard X-ray example at $\lambda_r = 0.13$ nm: the pulse profiles, phase profiles and spectra of (a) SASE and (b) HB-SASE. The SASE pulse is a broad bandwidth chaotic sequence of phase uncorrelated spikes whereas the HB-SASE pulse is near single spike with slowly varying phase and narrow bandwidth.

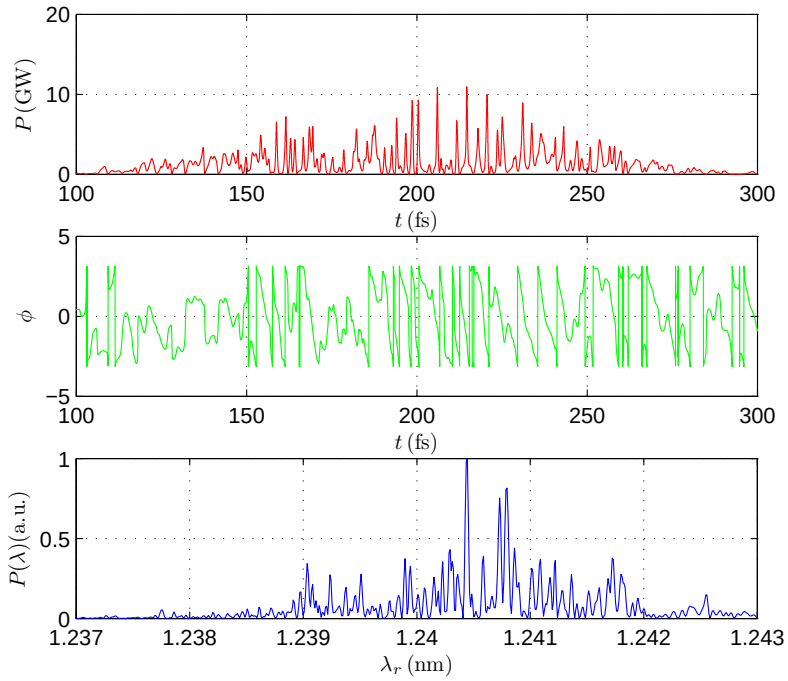

(a) SASE Control Case.

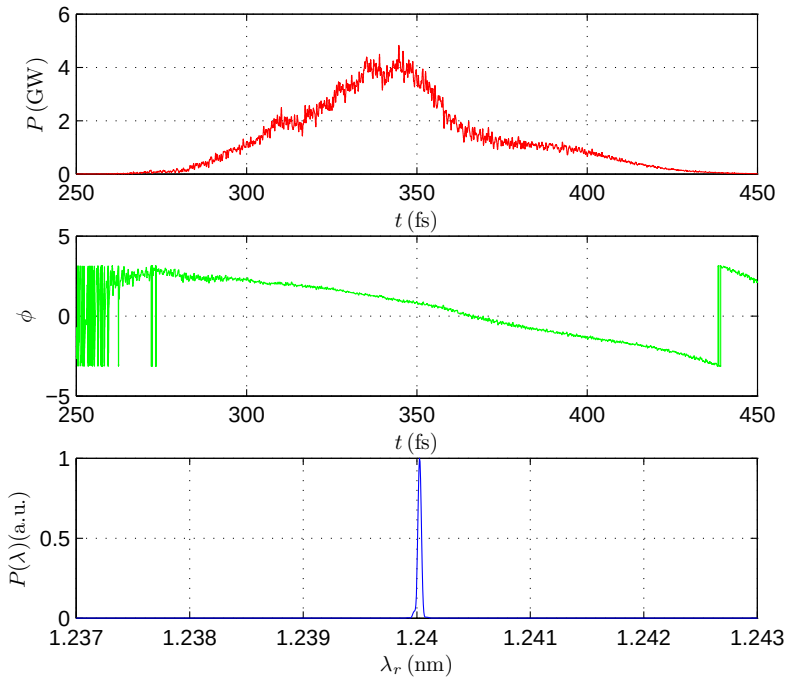

(b) HB-SASE.

Figure 3.46: Soft X-ray example at $\lambda_r = 1.24$ nm: the pulse profiles, phase profiles and spectra of (a) SASE and (b) HB-SASE. As in the hard X-ray example, the SASE pulse is again a broad bandwidth chaotic sequence of phase uncorrelated spikes whereas the HB-SASE pulse is near single spike with slowly varying phase and narrow bandwidth.

The results are shown scaled back into S.I. units. Figure 3.46 shows the pulse profiles, phase profiles and spectra of SASE and HB-SASE at saturation. For SASE the coherence time $t_{\rm coh} = l_{\rm coh}/c$ is 1.47fs, close to the value of 1.23fs predicted by (2.230), and $\sigma_\lambda/\lambda = 8.5 \times 10^{-4} \simeq \rho$ in agreement with SASE theory. For HB-SASE $t_{\rm coh} = 90$ fs, approximately the full duration of the pulse, with bandwidth $\sigma_\lambda/\lambda = 1.34 \times 10^{-5}$. The FWHM pulse duration and bandwidth give time-bandwidth product $\Delta\nu\Delta t = (1/\lambda)(\Delta\lambda/\lambda)c\Delta t = 0.53$, close to that of a transform-limited gaussian pulse.

	Hard X-Ray		**Soft X-Ray**	
	SASE	HB-SASE	SASE	HB-SASE
P (GW)	30	40	10	4
$\dot{N}$ (#ph/s)	2.6×10^{23}	2.0×10^{23}	6.2×10^{25}	2.5×10^{25}
σ_λ/λ	4.3×10^{-4}	2.0×10^{-5}	8.5×10^{-4}	1.3×10^{-5}
B (#ph/s/mm-mrad^2/0.1% bw)	5.7×10^{31}	9.3×10^{32}	7.6×10^{31}	1.9×10^{33}

Table 3.2: Brightness comparison between SASE and HB-SASE for hard X-ray and soft X-ray simulations.

3.8.3 Brightness Comparison

The brightness of a photon source is measured in terms of the phase space density of the photon flux, or the number of photons per unit solid angle per unit solid area, and is typically normalised to the radiation bandwidth [52]. The simulations performed here are one-dimensional and so the transverse properties of the photon source are not modelled. However, under the assumption that in reality the photon source would be close to diffraction limited (a good approximation for a SASE FEL) the normalised brightness can be estimated using

$$B \simeq \frac{4\dot{N}}{\lambda_r^2 \left| \frac{\Delta\lambda}{\lambda_r} \right|} \tag{3.73}$$

where $\dot{N}$ is the photon flux and $|\Delta\lambda/\lambda_r|$ is the FWHM bandwidth. This calculation has been made for the SASE and HB-SASE simulations of Sections 3.8.1 and 3.8.2. The FWHM bandwidths are taken to be 2.5 times broader than the quoted rms bandwidths. The results are shown in Table 3.2. The increase in brightness of HB-SASE over SASE is thus a factor of 16 in the hard X-ray and a factor of 25 in the soft X-ray. This can also be illustrated graphically by plotting the spectra of HB-SASE and SASE on the same $P(\lambda)$ scale as shown in Figure 3.47. These results show clearly that the brightness of HB-SASE far exceeds that of SASE—hence justifying the name.

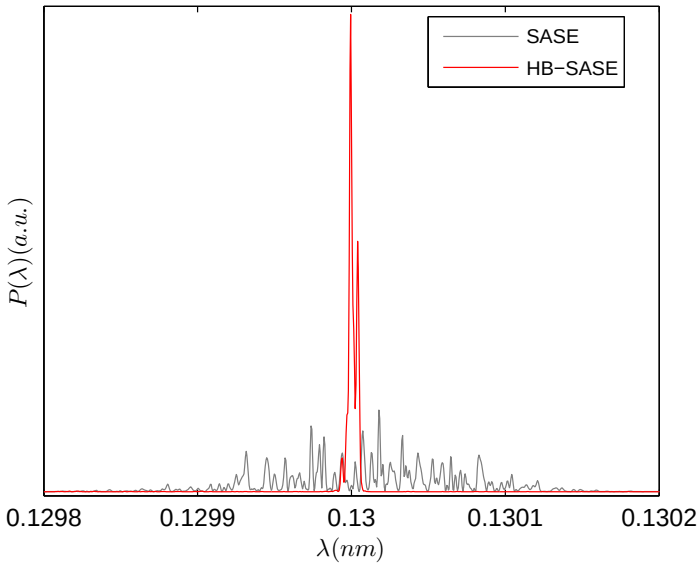

(a) Hard X-ray.

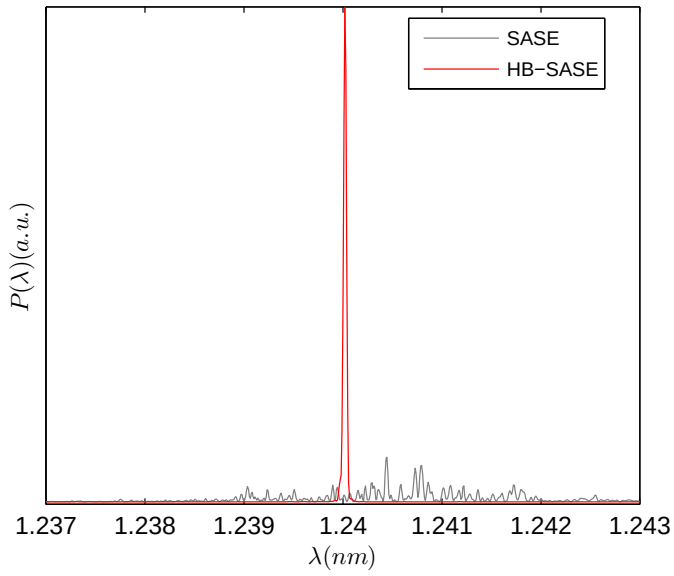

(b) Soft X-ray.

Figure 3.47: Spectra of HB-SASE and SASE plotted on the same $P(\lambda)$ scale to illustrate the comparative brightness, for (a) Hard X-ray and (b) Soft X-ray.

Chapter 4

Mode-Locked Amplifier FEL

4.1 Introduction

In this Chapter further investigation is made of the modal radiation structure discovered during the development of HB-SASE in Chapter 3. This leads to the concept of the Mode-Locked Amplifier FEL which may produce a train of cleanly separated, high-intensity, phase-locked radiation spikes with the duration of each spike dependent on the number of periods in each undulator module, rather than the cooperation length l_c. This gives the possibility of generating high-intensity FEL pulses with lengths $\ll l_c$.

In the X-ray region of the spectrum l_c is typically a few tens of nanometers, so a pulse of length l_c would have duration in the hundreds of attoseconds. Such pulses would enable observation and possible control of very fast phenomena at the atomic timescale [53]. Several techniques have already been identified that may produce FEL pulses in this regime. Selection of a short harmonic spike in a multiple undulator harmonic cascade may be one option [54]. Other techniques pre-modulate the electron bunch energy with an optical laser before the bunch enters the radiator undulator. The resonant FEL wavelength is correlated to this energy modulation and it may be possible to selectively filter [55] or amplify [56] a narrow wavelength band to generate short pulses with widths of a fraction of the modulation period. Other techniques rely upon similar electron bunch energy modulation methods [57, 58]. Another approach, called E-SASE [59, 60], uses an optical laser to modulate the electron bunch energy at an intermediate acceleration stage. Regions of enhanced current are created that subsequently generate short pulses in a final radiator undulator. A conceptually simpler method [61]

'spoils' all but a short region of the electron bunch. Only this region subsequently lases in the FEL to generate a short radiation pulse. More recently, a technique using an FEL with a negative undulator taper and a pre-modulated bunch energy has been proposed [62]. The above techniques all produce pulse durations of the order of the cooperation length and typically predict pulse widths ~ 100 as at a target wavelength of ~ 1.5 Å.

By comparison, the Mode-Locked Amplifier FEL breaks the dependence of the pulse length on the cooperation length and may generate pulses up to an order of magnitude shorter, with durations less than the atomic unit of time (24 as). By applying concepts from mode-locked cavity lasers [63], the prediction is the generation of a train of multi-GW peak power pulses, at wavelength 1.5 Å, of width ≈ 23 as with 150 as separation. Such pulses may have sufficient power, spatial and temporal resolution to offer a new scientific tool for observing the dynamics of atomic-scale phenomena.

4.2 Generation of Axial Modes

In Section 3.3 numerical simulations of the HB-SASE system, using equal delays, were presented. It was seen that sideband frequencies were generated in the spectra which corresponded to a temporal modulation of the pulse profile. The spectrum of the spontaneous emission was derived analytically (both without gain and also with a simple gain term included) to give some insight into the physics of the sideband generation. In the remainder of the Chapter efforts were made to remove these sideband frequencies because they inhibited the development of full longitudinal coherence—since there was no fixed phase relationship between the discrete frequencies they produced large and irregular time variations in the amplitude and phase of the output pulse.

The insight that enabled the development of the Mode-Locked Amplifier FEL was the realisation that *the frequency spectrum observed in the simulations and derived for the spontaneous emission is exactly analagous to the axial mode spectrum of a conventional cavity laser.* With this understanding it was possible to borrow methods from laser physics to lock the axial modes together and generate extremely short pulse output.

4.2.1 Axial Mode Spectrum of a Laser Cavity

Following [63] closely, the circulating signal inside an oscillating laser cavity can be described in the time domain using recirculating pulse concepts. A signal $\varepsilon(t)$ is considered which transits any reference plane within the cavity with period T given by $T = p/c$ for a ring cavity of perimeter p. The frequencies which can oscillate within the cavity, or the axial modes, are those for which the round trip phase shift inside the cavity is an integer multiple of 2π, or the perimeter p is an integer number of wavelengths

$$\frac{p}{\lambda} = q \tag{4.1}$$

where q is an integer. The axial mode frequencies are therefore

$$\omega_q = q\frac{2\pi c}{p} \tag{4.2}$$

and the spacing is

$$\Delta\omega = \frac{2\pi c}{p} = \frac{2\pi}{T} \tag{4.3}$$

If the signal $\varepsilon(t)$ has time fluctuations in amplitude or phase that are are rapid compared to the round trip time its spectrum $\tilde{E}(\omega)$ will have a spread in frequency wider than $2\pi/T$ and hence wider than the mode spacing $\Delta\omega$. By considering a signal comprising N repeated copies of $\varepsilon(t)$, each delayed by T,

$$\varepsilon^{(N)}(t) \equiv \sum_{n=0}^{N-1} \varepsilon(t - nT) \tag{4.4}$$

the Fourier transform is

$$\tilde{E}^{(N)}(\omega) = \tilde{E}(\omega) \sum_{n=0}^{N-1} e^{-inT\omega} = \tilde{E}(\omega)\frac{1 - e^{-iNT\omega}}{1 - e^{-iT\omega}} \tag{4.5}$$

with power spectral density

$$I^{(N)}(\omega) \equiv |\tilde{E}^{(N)}(\omega)|^2 = I(\omega)\frac{1 - \cos(NT\omega)}{1 - \cos(T\omega)} \tag{4.6}$$

which is the power spectral density of the original signal multiplied by an interference term. Examination of (4.6) shows that the function displays strong peaks at frequencies corresponding to the axial mode frequencies ω_q of the cavity, and

the interpretation of this result in [63] is that "It is the fixed time delay or time shift T between successive round trips that gives the axial mode character to a laser output signal, independent of the detailed waveform $\varepsilon(t)$ or of the carrier frequency ω_c that may characterise the optical sine waves under the output signal envelope".

4.2.2 The Analogy Between HB-SASE and Cavity Lasers

The spontaneous emission spectrum for HB-SASE with equal delays was shown to be (equation (3.33))

$$|\tilde{A}(\bar{\omega})|^2 = |\tilde{b}|^2 \bar{l}^2 \mathrm{sinc}^2\left(\frac{\bar{\omega}\bar{l}}{2}\right) \frac{1-\cos(N\bar{\omega}\bar{s}_1)}{1-\cos(\bar{\omega}\bar{s}_1)}. \tag{4.7}$$

which is the single undulator spectrum multiplied by an interference term. Comparison of Equations (4.6) and (4.7) shows that the spontaneous spectrum for HB-SASE with equal delays $\bar{s}_1$ is identical in form to that of a laser with ring cavity of perimeter p. As an example, suppose $\bar{s}_1 = 5$, and the FEL is operating in the X-ray at 0.15 nm for which typically $\rho = 5 \times 10^{-4}$, scaling $\bar{s}_1$ into S.I. units gives $s = 120$ nm. *In this case the process of repeatedly delaying the electron bunch is acting to synthesise an X-ray laser cavity of perimeter 120 nm.*

In a cavity laser the axial modes can be locked in phase to generate a single ultrashort pulse—it was the introduction of this concept in 1964 that allowed the pulse durations available from lasers to be reduced by orders of magnitudes over the next decades [53]. The realisation that the effect of the delays is to synthesise an optical cavity naturally led to the question of whether the modes in the FEL could also be phase locked.

4.3 Locking the Modes

As discussed in [63], the axial modes generated by a pulse circulating in a laser cavity are randomly phased with no fixed phase relationship between them, and this is responsible for large and irregular fluctuations in the amplitude and phase of the signal. In cavity lasers the modes can be actively locked in phase by introducing an amplitude modulator (AM) or frequency modulator (FM) inside the laser cavity with a modulation frequency ω_m. Each of the axial modes in the cavity then aquires modulation sidebands at frequencies $\omega_q \pm n \times \omega_m$. If

the modulator is driven at a frequency equal to the mode spacing, $\omega_m = \Delta\omega$, then the modulation sidebands of each cavity mode fall on top of adjacent cavity modes. The modulation sidebands 'injection lock' the axial modes with which they are in resonance (injection locking is a general phenomenon in which a weak monochromatic signal is injected into a more powerful free-running oscillator and captures the subsequent oscillation so that the oscillator becomes controlled by the injected signal) so that each axial mode becomes coupled via the modulation sidebands to one or more of its neighbouring modes. The result is that the axial modes become locked in phase. What this means is that if, for example, each of N modes is considered as a phasor of the same amplitude rotating at its own angular frequency ω_q there are some times $t = t_0 + nT$ at which all the phasors point in the same direction and the total field amplitude is then N times the amplitude of a single mode. At times $\Delta t = \pm T/N$ on either side of these peaks the phasors become uniformly distributed in angle and the total field amplitude is then zero. The result is a single pulse of FWHM duration $\approx T/N$ every cavity round trip period, separated by $N-2$ much weaker subsidiary peaks. If the mode amplitudes are not equal but have a gaussian envelope, the subsidiary peaks are eliminated.

In the FEL system the modulation required for locking is applied directly to the electron beam, either via an energy modulation [2], or via a modulation to the electron bunch current [64]. A modulation to the energy has multiple effects—it applies a frequency modulation to the system through the FEL resonance condition, a gain modulation because as seen in Section 2.5.4 the growth rate is a function of the energy detuning and a further gain modulation which depends on the local energy gradient. A modulation to the beam current will only modulate the gain. Whichever method is used, the end result is a modulation of the coupling between the electron beam and radiation which will cause a modulation of the electron beam bunching. The effect of this can be understood via the spontaneous emission spectrum (4.7). The term $\tilde{b}$ is the Fourier transform of the bunching term $b(\bar{z}, \bar{z}_1)$ which, as seen in (2.135), is the source term driving the field development. If a sinusoidal modulation of period $\bar{s}_1$ is applied to the bunching so that

$$b(\bar{z}_1) = b_0(\bar{z}_1)\left[1 + \cos\left(\frac{2\pi\bar{z}_1}{\bar{s}_1}\right)\right] \tag{4.8}$$

$$= b_0 + \frac{b_0}{2}\left[e^{i\frac{2\pi}{\bar{s}_1}\bar{z}_1} + e^{-i\frac{2\pi}{\bar{s}_1}\bar{z}_1}\right] \tag{4.9}$$

then the Fourier transform becomes

$$\tilde{b}(\bar{\omega}) = \tilde{b}_0(\bar{\omega}) + \tfrac{1}{2}\tilde{b}_0(\bar{\omega} - \tfrac{2\pi}{\bar{s}_1}) + \tfrac{1}{2}\tilde{b}_0(\bar{\omega} + \tfrac{2\pi}{\bar{s}_1}) \tag{4.10}$$

where the Fourier transform property

$$\mathbb{F}\left[e^{2\pi i a x} f(x)\right] = \tilde{f}(\omega - 2\pi a) \tag{4.11}$$

has been used. The spontaneous emission spectrum then becomes

$$\begin{aligned} |\tilde{A}(\bar{\omega})|^2 &= |\tilde{b}_0(\bar{\omega}) + \tfrac{1}{2}\tilde{b}_0(\bar{\omega} - \tfrac{2\pi}{\bar{s}_1}) + \tfrac{1}{2}\tilde{b}_0(\bar{\omega} + \tfrac{2\pi}{\bar{s}_1})|^2 & (4.12)\\ &\quad \times \bar{l}^2 \mathrm{sinc}^2\left(\frac{\bar{\omega}\bar{l}}{2}\right) \frac{1 - \cos(N\bar{\omega}\bar{s}_1)}{1 - \cos(\bar{\omega}\bar{s}_1)}. & (4.13) \end{aligned}$$

showing that the field A at frequency $\bar{\omega}$ is now driven by the bunching not just at frequency $\bar{\omega}$ but also by the bunching at frequencies $\bar{\omega} - \frac{2\pi}{\bar{s}_1}$ and $\bar{\omega} + \frac{2\pi}{\bar{s}_1}$. Recalling that the mode spacing is $\Delta\bar{\omega} = \frac{2\pi}{\bar{s}_1}$ this means that the field on resonance in now driven by the bunching at the resonant frequency *and also by the bunching at the frequencies of the adjoining modes*, and in fact each mode is now driven by the bunching at the frequencies of its nearest neighbours. The FEL is a coupled system—from (2.134) the field drives the electron energy, from (2.133) the electron energy drives a change in electron phase and the bunching parameter $b = \langle e^{i\theta} \rangle$ is the average over all the electron phases, so as the FEL interaction proceeds each mode drives the electron bunching at its frequency and the bunching at this frequency drives the radiation of the neighbouring modes. Therefore, through the electron beam bunching, a coupling develops between neighbouring field modes, and this then propagates to next nearest neighbours, and so on, until all the radiation modes becomes locked in phase.

4.4 Simulation Results

In this section results are shown using the one-dimensional code used to model HB-SASE, and then using Genesis 1.3, a well benchmarked three-dimensional code which extends the modelling to validate the technique with the inclusion of realistic beam transport, radiation diffraction, electron beam energy spread and emittance. Figure 4.1 shows a schematic of the three systems modelled in

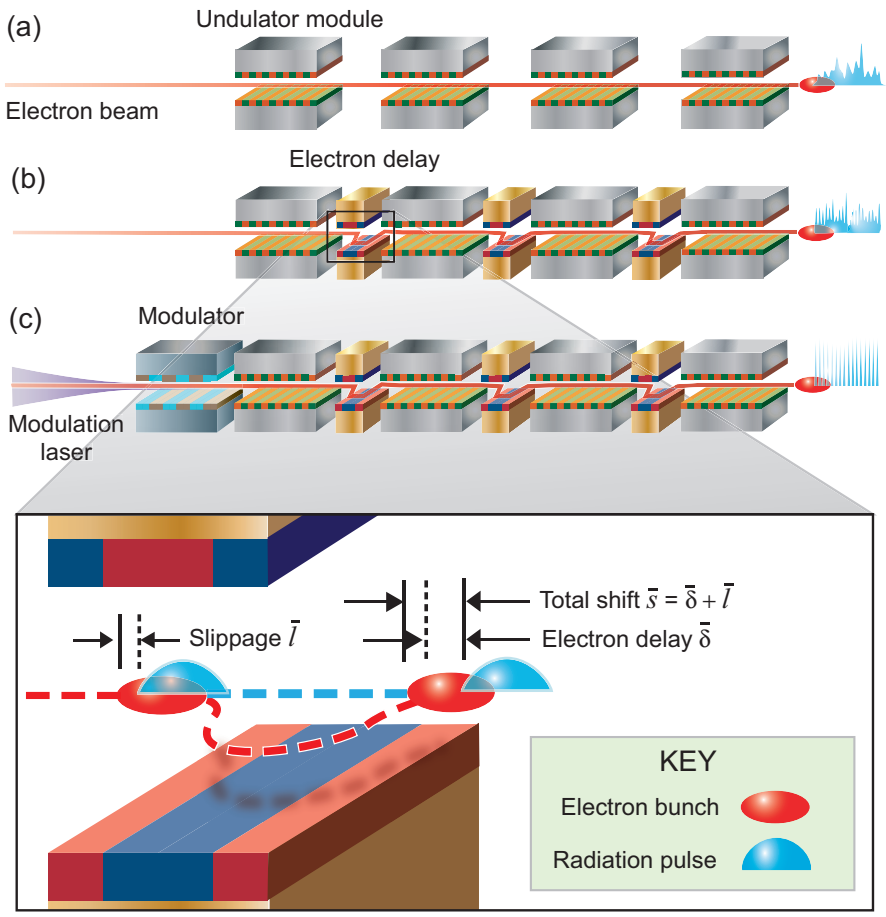

Figure 4.1: Schematic of three regimes of FEL interaction: (a) SASE regime (b) Chicane delays introduced with no energy modulation (c) Mode-locked via the introduction of an energy modulation. The inset shows detail of the electron delay.

this section—Figure 4.1(a) shows the normal SASE regime which was simulated as a control (not shown for 1D results), Figure 4.1(b) shows the introduction of chicane delays but no energy modulation, and Figure 4.1 (c) shows the mode-locked system where an energy modulation has been added.

4.4.1 One-Dimensional Simulations

The parameters used for the one dimensional simulations are module length $\bar{l} = 0.25$ and delay $\bar{\delta}_1 = 1.5$, so $\bar{s}_1 = 1.75$ and $S_e = 7$. The modulation to the system

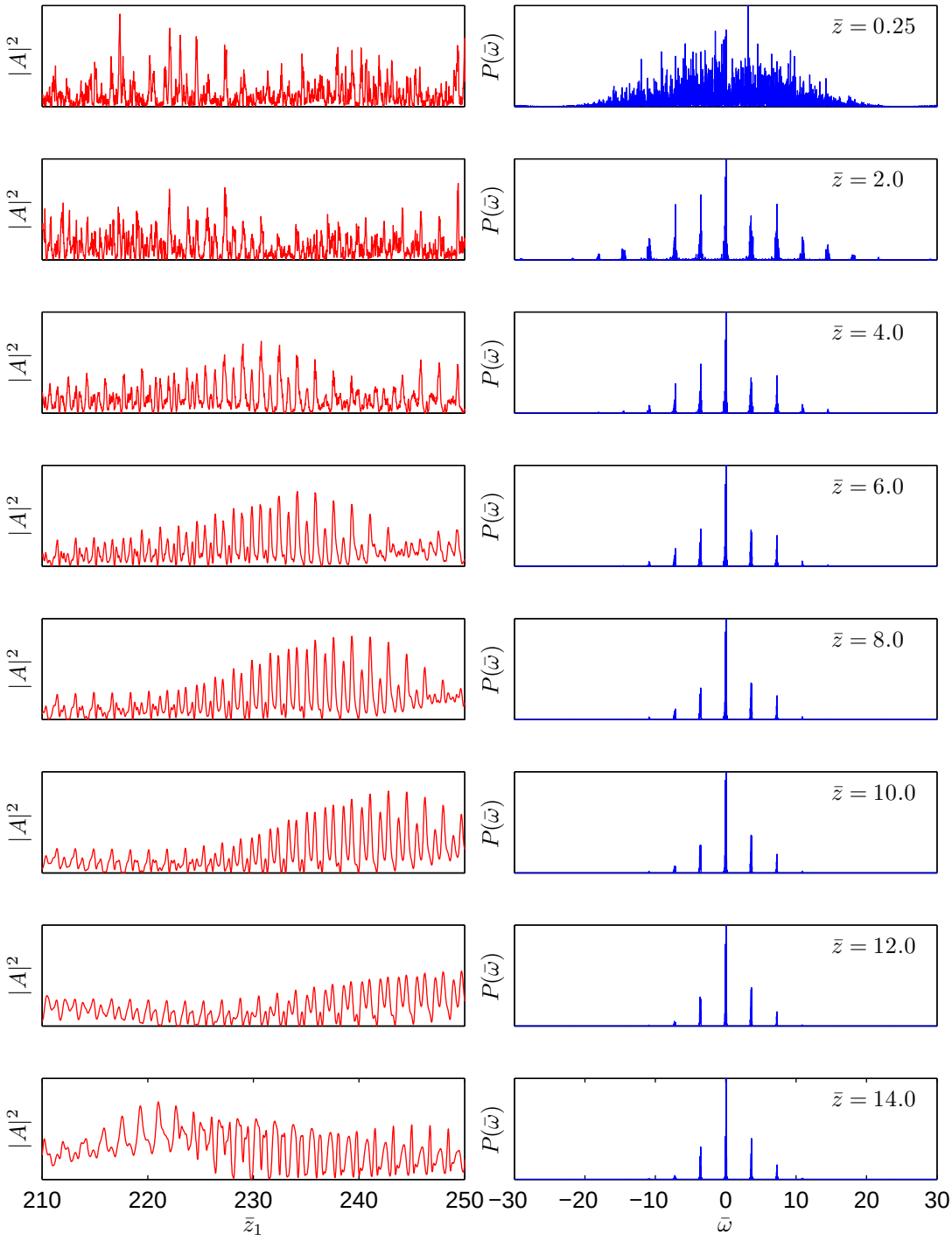

Figure 4.2: One dimensional mode-locking simulations with energy modulation set to $\Delta\bar{p} = 0$. The left column shows the pulse intensities $|A|^2$ vs $\bar{z}_1$. The scale of $|A|^2$ is not shown, but saturation occurs at $\bar{z} = 12.0$ where peak $|A|^2 \simeq 1.0$. The right column shows the normalised spectra.

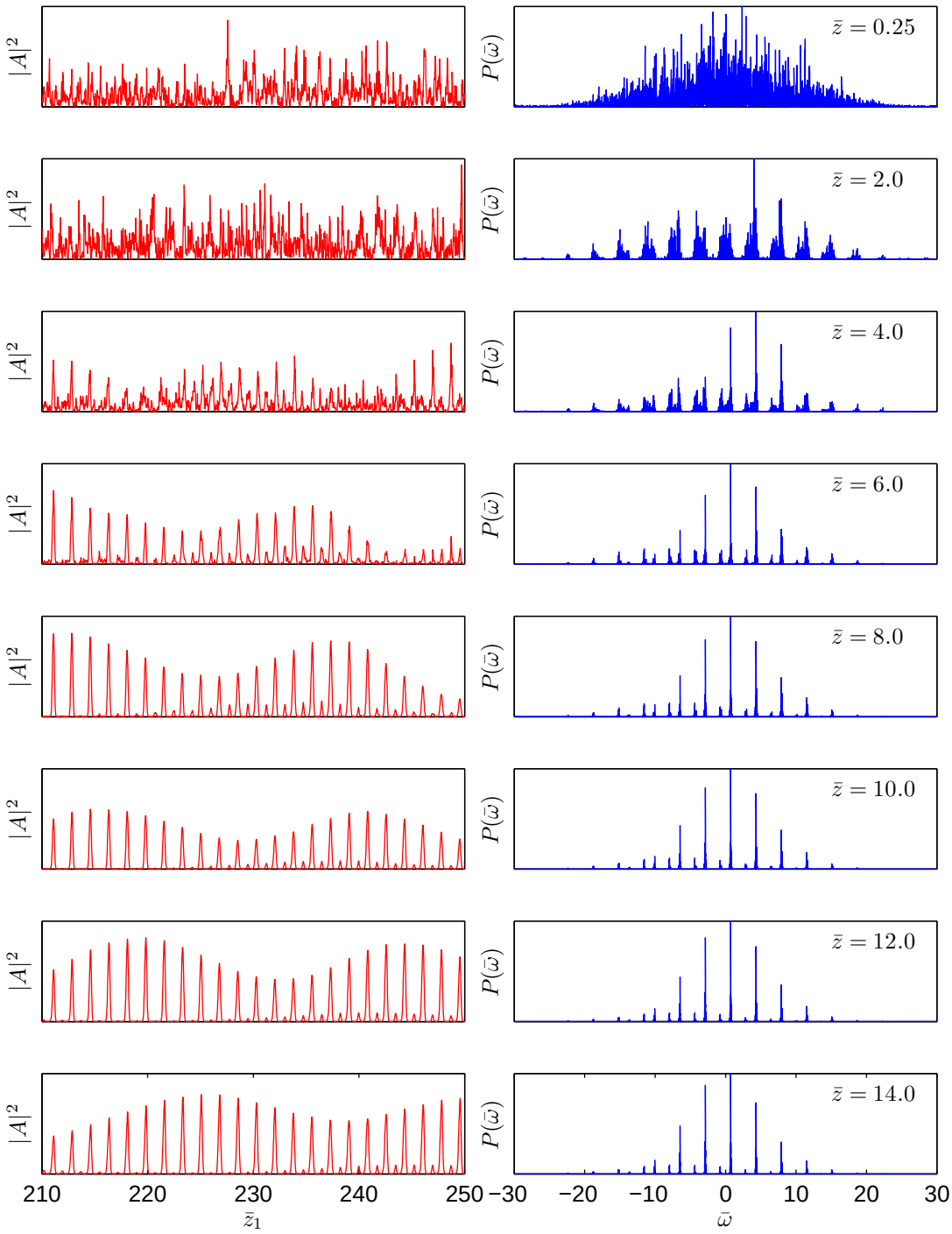

Figure 4.3: One dimensional mode-locking simulations with energy modulation $\Delta\bar{p} = 5$. The left column shows the pulse intensities $|A|^2$ vs $\bar{z}_1$. The scale of $|A|^2$ is not shown, but saturation occurs at $\bar{z} = 14.0$ where peak $|A|^2 \simeq 1.0$. The right column shows the normalised spectra.

was applied via an energy modulation of amplitude $\Delta\bar{p}$ and period $\bar{s}_1$, so that

$$\bar{p}(\bar{z}_1) = \bar{p}_0 + \Delta\bar{p}\cos\left(\frac{2\pi\bar{z}_1}{\bar{s}_1}\right). \tag{4.14}$$

First, results are shown where $\Delta\bar{p} = 0$. In this case the axial mode spectrum is generated but the modes are not phase locked. Figure 4.2 shows the pulse intensities $|A|^2$ vs $\bar{z}_1$ for different values of the propagation distance $\bar{z}$. The scale of $|A|^2$ is not shown, but saturation occurs at $\bar{z} = 12.0$ where peak $|A|^2 \simeq 1.0$. The right column shows the normalised spectra. The mode structure is clearly seen, with spacing $\Delta\bar{\omega} = 2\pi/\bar{s}_1 = 3.59$. In the time domain the pulse is strongly modulated with period $\bar{\tau} = \bar{s}_1 = 1.75$ but the spikes are not cleanly separated. This is because the axial modes are randomly phased.

Next, the energy modulation is increased to $\Delta\bar{p} = 5$ with all other parameters unchanged. The results are shown in Figure 4.3. Saturation now occurs at $\bar{z} = 14.0$. The pulse at saturation comprises a train of clearly separated spikes each of which has FWHM length $\simeq 0.25$ which is one quarter of the cooperation length and equal to the slippage in one undulator module of length $\bar{l} = 0.25$. Analysis of the full simulated pulse of length 300 shows that the slowly varying spike envelope has a mean peak-to-peak distance of 35 with a maximum of 42, very close to the normal SASE maximum spike spacing multiplied by the slippage enhancement $2\pi \times S_e = 44$. The spectra show substantial differences to the case with $\Delta\bar{p} = 0$. Towards the beginning of the interaction, at $\bar{z} = 2.0$, the individual modes appear much broader, then as $\bar{z}$ increases each mode is seen to split into two 'sub-modes', with the intensity of the higher frequency sub-mode gradually increasing with respect to the lower frequency one as $\bar{z}$ increases. At saturation this sub-mode structure is still apparent. The other important observations are that compared to the case with $\Delta\bar{p} = 0$, the mode spectrum remains extended to nearly the full single undulator bandwidth $2\pi/\bar{l} = 25$ as $\bar{z}$ increases and for a given $\bar{z}$ the decay in the mode intensities away from resonance is more gradual.

The differences in the spectra at saturation, for $\Delta\bar{p} = 0$ and $\Delta\bar{p} = 5$, are shown more clearly in Figure 4.4 on linear and logarithmic scales. It is seen clearly that with the energy modulation included each mode is split. Study of simulation results using different energy modulations shows that as $\Delta\bar{p}$ is increased the frequency split increases linearly, and that the asymmetry between

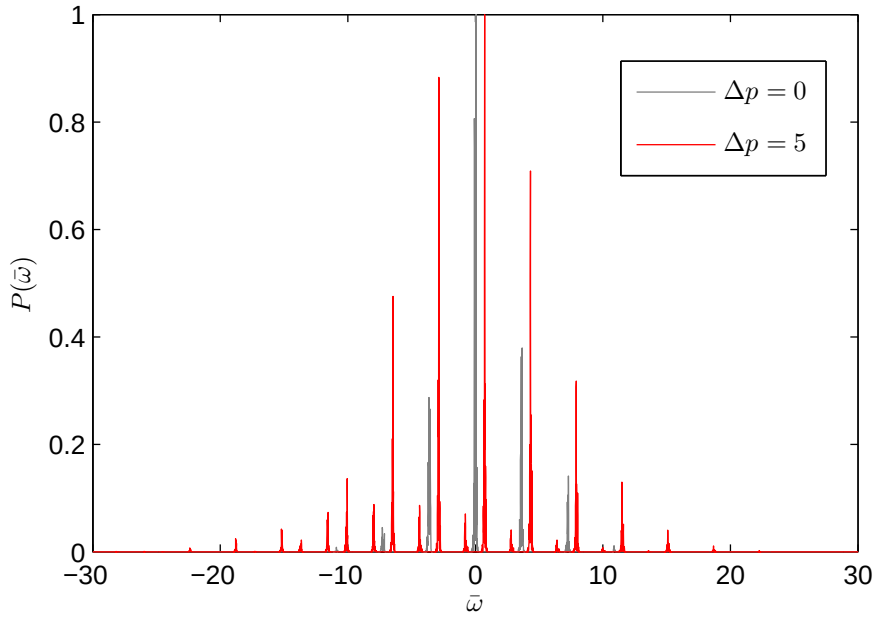

(a) Linear plot.

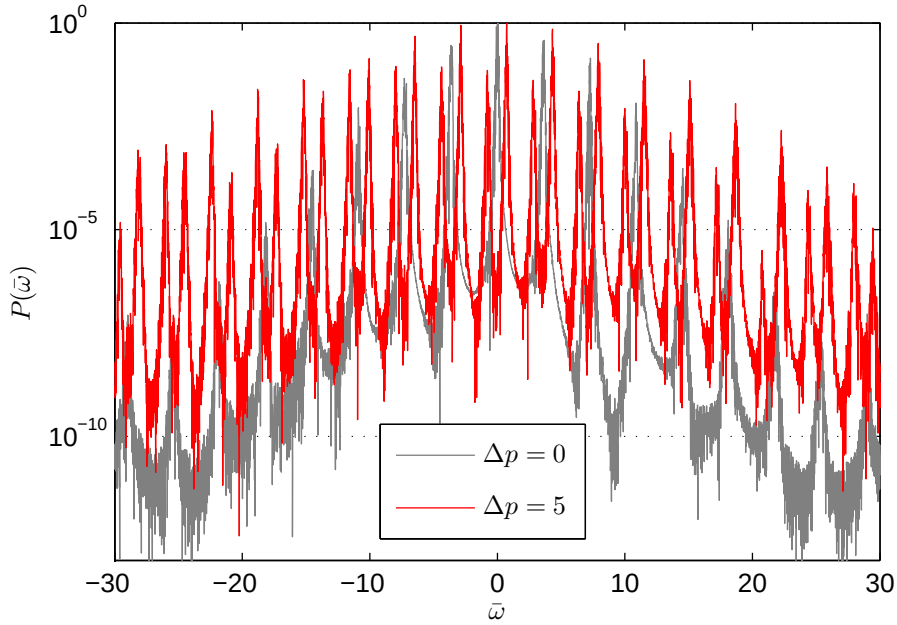

(b) Logarithmic plot.

Figure 4.4: Comparison of spectra at respective saturation points for $\Delta\bar{p} = 0$ and $\Delta\bar{p} = 5$ on (a) linear and (b) logarithmic scales. The coupling between the modes introduced by the energy modulation has driven the evolution of the radiation out to wider frequencies.

the intensity of the split modes also increases. Study of the pulses in the time domain, as seen in Figure 4.3, shows that there are small sub-spikes evident between the main spikes, with the intensity of these, relative to the intensity of the main spikes, approximately equal to the relative intensity between the dominant and lesser sub-modes. The interpretation of these results is that the dominant effect of the energy modulation in the electron beam is to provide a gain modulation which depends on the local energy gradient—as the radiation slips through the electron bunch during the interaction in each undulator the integrated energy spread experienced by the radiation is smallest at the maxima and minima of the energy modulation where the local gradient is zero so the gain at these positions is higher. The radiation spikes develop preferentially at these positions and the result is two separate interleaved trains of pulses, with the spectral comb comprising the dominant sub-modes corresponding to the dominant temporal spikes, and the spectral comb comprising the lesser sub-modes corresponding to the temporal sub-spikes. As seen in Figure 2.3 there is an asymmetry in the growth rate about resonance, so this accounts for the asymmetry between the two interleaved frequency combs and pulse trains and for the fact that this asymmetry increases as $\Delta\bar{p}$ increases.

The comparison between the spectra at saturation, for $\Delta\bar{p} = 0$ and $\Delta\bar{p} = 5$, as shown in Figure 4.4, also highlights the extended width of the mode spectrum when the energy modulation is included. For example, the mode that falls on the single undulator full bandwidth at $\bar{\omega} = -2\pi/\bar{l} = -25.13$ has a normalised intensity of 2×10^{-8} for $\Delta\bar{p} = 0$ and 1×10^{-3} for $\Delta\bar{p} = 5$, a difference of a factor of 5×10^4. The interpretation of this feature is that the coupling between the modes introduced by the energy modulation is driving the evolution of the radiation from mode to mode out to wider frequencies.

4.4.2 Three-Dimensional Simulations

The simulations presented so far have been done with the one-dimensional simulation code. This code neglects some of the physical effects which may have an effect on the performance of the Mode-Locked FEL. In order to make a more complete study the system was simulated using the 3-D code `Genesis 1.3` [65]. Simulations were done for operation at two different wavelengths, with typical realistic parameters given in Table 4.1. The extra physics included in the `Genesis 1.3` code is the inclusion of extra dimensions. In the one-dimensional code the electron

phase space is two dimensional—each electron has an energy p and a longitudinal position s (via a phase θ within an indexed window of length λ_r). In `Genesis 1.3` the electron phase space is six-dimensional, with the inclusion of transverse position and momentum in x and y. This allows the effect of beam emittance to be properly modelled as well as the transport of the electron bunch in the presence of focussing terms from the undulator and from external quadrupoles. In the one-dimensional code the radiation field is represented by a complex envelope A which is sampled once per radiation wavelength. In `Genesis 1.3` the radiation field is also sampled once per radiation wavelength but modelled over a transverse grid which permits transverse modes to evolve and the effect of diffraction to be included. `Genesis 1.3` also has a number of other features, not used in this work, but which are invaluable for modelling FELs for a variety of applications including: harmonic output; the ability to add errors and misalignments; the ability to import and export particle distributions and radiation field files and hence interface with other codes. For these reasons `Genesis 1.3` is very widely used, with its results well benchmarked against experiment, so it was interesting to apply it to the mode-locking scheme.

XUV Mode-Locking

The first system modelled was a typical XUV FEL design for operation at 12.4 nm, with parameters given in Table 4.1. Fig. 4.5 shows the radiation power output close to saturation, over a 100 fs window, for the three cases of SASE, equal delays with no energy modulation, and mode locking with the inclusion of energy modulation. Insets plot the power spectral density as a function of radiation wavelength. For the SASE case the output is seen to be noisy, comprising a series of irregularly spaced pulses with mean separation approximately $2\pi l_c$, corresponding to a temporal duration $2\pi\tau_{coh} = \lambda_r/2c\rho \approx 8$fs, with a spectrum centred at the resonant wavelength of fractional width $\approx 2\rho$. These results, as would be expected, are typical of SASE.

In Fig. 4.5(b) 4-dipole chicanes are introduced to give delay $\delta = 48\lambda_r$, with the total slippage due to the undulator and delay section $s = 60\lambda_r$. The total slippage time is $T_s \approx 2.48$ fs, with the slippage enhancement factor $S_e = 5$. Longitudinal dispersion of the chicanes is included in the simulation (equivalent to $D = 1$ in the 1D simulation code) which has the effect of reducing the saturation length to around 65% of that for the SASE case. This is due to the chicanes enhancing the

	XUV	**X-ray**
Bunch energy E(GeV)	0.75	14.3
Bunch peak current I(kA)	3	3.4
Normalised emittance ϵ_n(mm-mrad)	2	1.2
RMS fractional energy spread σ_γ/γ_0	10^{-4}	8×10^{-5}
Undulator period λ_w(cm)	3.1	3
Resonant wavelength λ_r(Å)	123	1.5
Undulator module length (units l/λ_w)	12	72
FEL parameter ρ	2.5×10^{-3}	5×10^{-4}
Chicane delay $N_c = \delta/\lambda_r$	48	228
Modulation period (units of λ_r)	61	303
Modulation amplitude (MeV)	5.8	14.3
Slippage enhancement S_e	5	5

Table 4.1: XUV and X-ray simulation parameters.

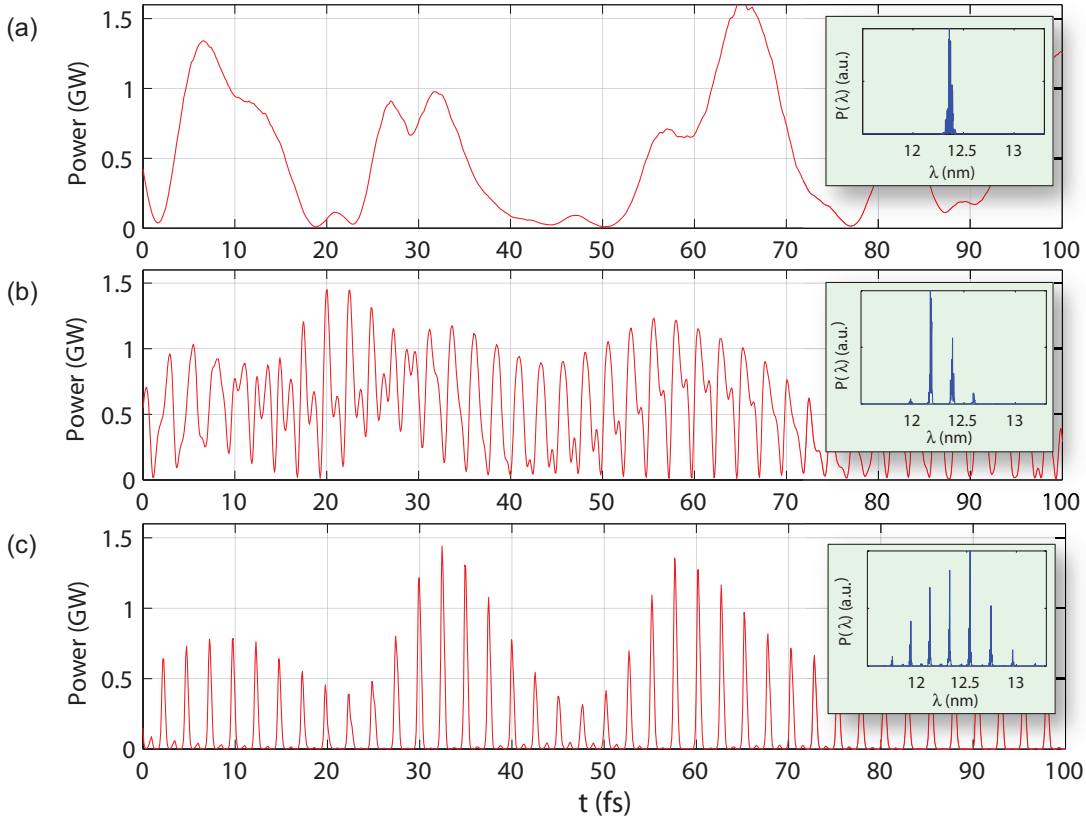

Figure 4.5: `Genesis 1.3` simulations in the XUV region of the spectrum at $\lambda_r = 12.4$ nm. The radiation power output close to saturation, over a 100fs sample, for the three cases of (a) SASE, (b) equal delays with no energy modulation, and (c) mode-locking with the inclusion of energy modulation. Insets plot the power spectral density as a function of radiation wavelength.

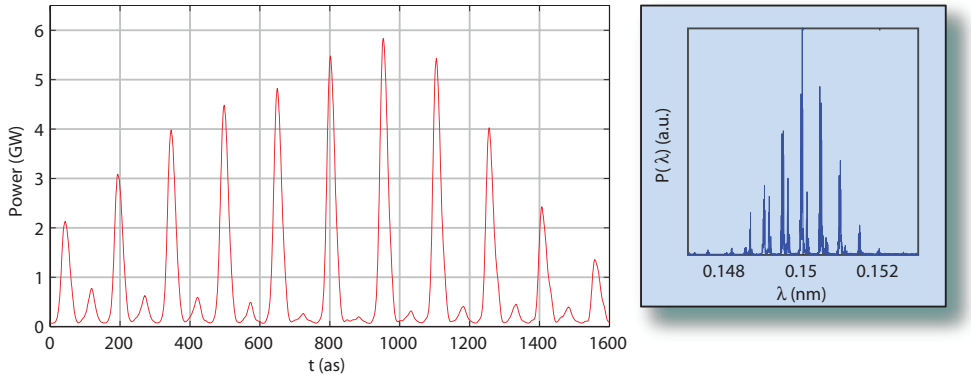

Figure 4.6: A mode-locked 1.5Å X-ray FEL example: the radiation power as a function of time t with radiation power spectrum as a function of wavelength in nm.

electron beam bunching rate, as seen in the simulations of HB-SASE in Section 3.7.2. The spectrum is seen to have modes with separation $\Delta\omega = 2\pi/T_s$, giving wavelength separation $\Delta\lambda \approx \lambda_r^2/s \approx 0.21$ nm. In the temporal domain the power comprises a series of spikes with width $\tau_p \simeq 1$ fs FWHM and separation $T_s \approx 2.48$fs. The modes here are randomly phased with the relative phases drifting along the pulse, giving the slowly evolving structure.

When the beam energy is modulated at the mode separation frequency $\Delta\omega$ the radiation modes are seen to phase lock over the entire bunch. A modulation amplitude of 5.8 MeV was used. This was obtained by modelling in `Genesis 1.3` a 10 period modulator undulator, $\lambda_w = 75$mm, seeded with a 230 MW 755 nm laser. From Fig. 4.5(c) it is seen that mode-locking occurs, dramatically improving the temporal pulse structure to give a train of pulses, evenly spaced by $T_s \approx 2.48$fs, of constant width $\tau_p \approx 400$as and peak power $\lesssim 1.4$GW. The contrast ratio between the peak power of the spikes and the background is > 100. The only remnant of the SASE noise is the slowly varying envelope of mean period $2\pi\tau_{coh} \approx 27$fs.

Hard X-ray Mode-Locking

The second system demonstrates the FEL mode-locking technique scaled to shorter wavelengths. Fig. 4.6 shows saturated output power in the X-ray at 1.5Å for $S_e = 5$ and other parameters similar to LCLS [66] and given in Table 4.1. The pulse train consists of ≈ 23 as pulses separated by $T_s \approx 150$ as with peak powers up to 6 GW and a contrast ratio ≈ 60.

From (3.42) the number of modes under the central peak of the spontaneous spectrum is $N_s \simeq 2S_e = 10$. From Fig. 4.5 and Fig. 4.6 the number of observed modes $N_0 \approx 8$ in the XUV and $N_0 \approx 9$ in the X-ray, indicating that the mode spectrum bandwidth is nearly as broad as the single undulator bandwidth. The output pulse width of a homogeneously broadened mode-locked cavity laser is given by [63]

$$\tau_p \approx \frac{0.5}{\sqrt{N_0} f_m} \tag{4.15}$$

where N_0 is the number of oscillating modes in the cavity and f_m the modulation frequency. Equation (4.15) can be translated into the parameters of the mode-locked FEL as

$$\tau_p \approx \frac{0.5 N_w \lambda_r S_e}{\sqrt{N_0} c} \tag{4.16}$$

which gives pulse lengths $\tau_p \approx 440$as in the XUV and $\tau_p \approx 25$as in the X-ray, in good agreement with the values from the simulations of $\tau_p \approx 400$as and $\tau_p \approx 23$as respectively. This result strengthens the analogy with the results of conventional mode-locked cavity lasers and indicates that the modes are indeed phase-locked.

4.5 Assessment of Tolerances

An assessment has been made of the required system parameter tolerances for a mode-locked SASE FEL system. The criteria derived, together with their numerical values for the XUV and X-ray systems modelled, are summarised in Table 4.2.

4.5.1 Energy Spread

High-gain optical klystron theory [67] gives a criterion for operation which relates the electron beam energy spread to the dispersive strength of the chicane:

$$\bar{\sigma}_\gamma \equiv \frac{\sigma_\gamma}{\rho\gamma} \lesssim \frac{1}{\bar{D}}, \tag{4.17}$$

where $\bar{D} = 2\pi\rho R_{56}/\lambda_r$, as given in (3.3), and from (3.4) and (3.5) the momentum compaction factor

$$R_{56} \simeq 2\delta \tag{4.18}$$

with δ the chicane delay in unscaled units. This gives

$$\frac{\sigma_\gamma}{\gamma} \lesssim \frac{\lambda_r}{4\pi\delta}. \tag{4.19}$$

Defining $N_\delta = \delta/\lambda_r$ gives

$$\frac{\sigma_\gamma}{\gamma} \lesssim \frac{1}{4\pi N_\delta}. \tag{4.20}$$

For the generation of a modal structure in the spontaneous emission spectrum the radiation pulses emitted from each of the first few undulator sections must have similar phases, which only occurs if the evolution of the bunching parameter $|b(\bar{z}, \bar{z}_1)|$ with respect to $\bar{z}$, the propagation distance through the undulator, is 'slow'. Any initial bunching would decay [68] as

$$|b(\bar{z}, \bar{z}_1)| \approx |b_0(\bar{z}_1)| e^{-\bar{z}^2\bar{\sigma}_\gamma^2/2} \tag{4.21}$$

where

$$\bar{\sigma}_\gamma \equiv \frac{1}{\rho}\frac{\sigma_\gamma}{\gamma} \tag{4.22}$$

and

$$\bar{z} = 4\pi\rho N_w. \tag{4.23}$$

To satisfy $b \approx b_0$

$$\bar{z}^2 \bar{\sigma}_\gamma^2 \ll 1 \tag{4.24}$$

so that

$$\frac{1}{\rho}\frac{\sigma_\gamma}{\gamma} 4\pi\rho N_w \ll 1 \tag{4.25}$$

giving an energy spread criterion:

$$\frac{\sigma_\gamma}{\gamma} \ll \frac{1}{4\pi N_w}. \tag{4.26}$$

Equations (4.20) and (4.26) have similar forms: in (4.20) N_δ is the delay in the chicane in units of the resonant wavelength and in (4.26) N_w is the delay in the undulator in units of the resonant wavelength. The overall energy spread requirement to maintain bunching through the undulator and the chicane can therefore be stated as approximately

$$\frac{\sigma_\gamma}{\gamma} \ll \frac{1}{4\pi(N_w + N_\delta)} = \frac{1}{4\pi N_w S_e} \tag{4.27}$$

where $S_e = (N_\delta + N_w)/N_w$.

4.5.2 Magnet Stability

Recall from (3.5) that the delay in a 4-dipole chicane with equal magnet and drift lengths L may be written as

$$\delta = \frac{5}{3} L\theta^2 \tag{4.28}$$

where θ is the deflection angle which is assumed to be small. For a relativistic beam the deflection angle in a single dipole of length L and field strength B is

$$\theta = \frac{LBc}{E} \tag{4.29}$$

where E is the beam energy in units of eV. Therefore from (4.28)

$$\delta = \frac{5}{3}\frac{L^3 B^2 c^2}{E^2}. \tag{4.30}$$

Taking the differential

$$\mathrm{d}\delta = \frac{10 L^3 B c^2}{3E^2}\mathrm{d}B = \frac{10\delta}{3}\frac{\mathrm{d}B}{B} \tag{4.31}$$

	XUV	**X-ray**
$\sigma_\gamma/\gamma < 1/(4\pi N_w S_e)$	1.3×10^{-3}	2.2×10^{-4}
$\Delta B/B < 1/(3N_\delta\sqrt{N})$	1.3×10^{-3}	2.7×10^{-4}

Table 4.2: Required tolerances for mode-locking, for the XUV and X-ray cases.

and applying the requirement for sub-wavelength phase matching $\mathrm{d}\delta < \lambda$ the tolerance on the magnetic field is obtained:

$$\frac{\mathrm{d}B}{B} < \frac{3\lambda}{10\delta} \simeq \frac{1}{3N_\delta} \tag{4.32}$$

If the chicanes are powered independently the errors will add as in a random walk so that the tolerance over N modules will be reduced by $1/\sqrt{N}$ to give

$$\frac{\mathrm{d}B}{B} < \frac{1}{3N_\delta\sqrt{N}}. \tag{4.33}$$

4.5.3 Energy Stability

The effect of shot-to-shot electron bunch energy fluctuation on the development of the synthesised axial modes is considered. The chicane delay is given by (4.30). As the resonant wavelength is given by

$$\lambda = \frac{\lambda_w}{2\gamma^2}(1 + a_w^2) \tag{4.34}$$

where $\gamma = E/E_0$ for a relativistic beam, the delay in units of resonant wavelengths is then given by

$$\frac{\delta}{\lambda} = \frac{10L^3B^2c^2}{3\lambda_w E_0^2(1 + a_w^2)}$$

which is independent of the beam energy so that if the beam energy fluctuates the chicanes always delay by exactly the same number of resonant wavelengths. This means that although the resonant wavelength may vary the development of the axial mode structure is unaffected.

4.5.4 Conclusion

The tolerances derived, and shown in Table 4.2 for the XUV and X-ray examples simulated, are achievable with current technology.

4.6 Further Mode-Locking Development

4.6.1 Non-Averaged Code Simulations

In previous sections the mode-locked FEL has been modelled in a one-dimensional code and in a three-dimensional code. Both of these codes are averaged codes—this means the equations they solve are averaged over a radiation wavelength, which restricts the scale of features which can be modelled and the accessible bandwidth. The minimum interval between sample points of the field is one radiation period, so the sampling rate is $\Delta t_s = f_r^{-1}$, the inverse of the resonant frequency. The Nyquist frequency, $f_N = 1/(2\Delta t_s)$, determines the bandwidth of frequencies that the field can contain without the effects of aliasing. Hence the range of frequencies that can be simulated by the averaged codes without aliasing effects is $f_r/2 < f_r < 3f_r/2$. As seen in the simulation results so far the bandwidth of the output is the single undulator full bandwidth, which although for the parameters used so far is adequately modelled by the averaged codes, could not be modelled properly if reducing the number of undulator periods per module to explore the minimum pulse durations possible.

A further limitation of the codes applied so far (in the versions used) is that the electrons are confined to their initial slices, each of a wavelength long, and no movement along the bunch can be modelled because each slice has periodic boundary conditions imposed. For the mode-locked FEL, the mode-locking is achieved by applying a sinusoidal energy modulation to the electron beam, with a period of many wavelengths. As the beam passes through the dispersive chicanes this sinusoidal energy variation will become sheared in longitudinal phase space, with the most and least energetic electrons moving through the beam by many resonant radiation wavelengths, and the energy modulation will evolve into a current modulation. This effect cannot be modelled in codes in which the electrons are confined to their initial slices.

The validity of the mode-locked simulations was therefore investigated by modelling the same system in a one-dimensional non-averaged code in which a far broader frequency range is accessible and the electrons are not confined to their buckets [69]. Some example results are shown in Figure 4.7. In this simulation the parameters are equivalent to that of the 12.4 nm `Genesis 1.3` simulations, including beam energy spread, the results of which are shown in Figure 4.5. The top plot shows the pulse temporal profile and the bottom plot shows the spectrum.

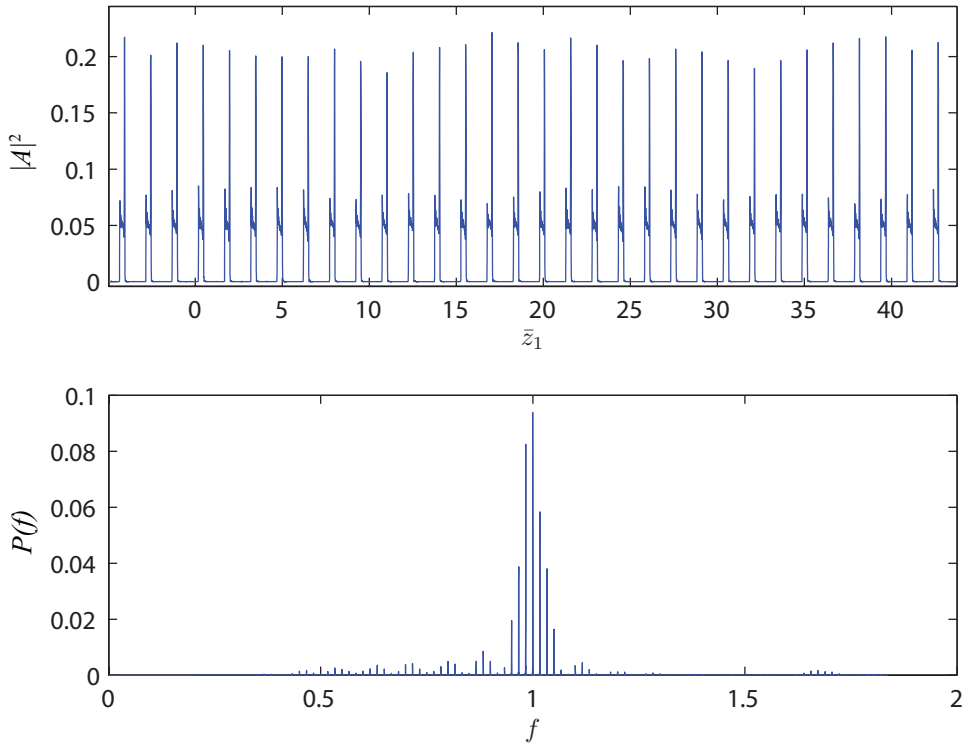

Figure 4.7: Simulation result from one-dimensional non-averaged code, for parameters equivalent to the 12.4 nm `Genesis 1.3` mode-locking simulations. The FWHM spike length scales to 57 as.

Note that in this plot the resonant frequency corresponds to $f = 1$. Converting the output to SI units gives peak power $\sim$1 GW with full variation in the spike-to-spike peak power $\Delta P/P \simeq 20\%$. The peak power is slightly reduced compared to the `Genesis 1.3` simulations, but the variation is much reduced. The small sub-spikes seen between the main spikes in the `Genesis 1.3` simulations are entirely absent, and the number of visible (on this linear scale) mode frequencies is about 50 over a very broad bandwidth, compared to around 9 in the `Genesis 1.3` simulations. Modes are visible outside the bandwidth $f_r/2 < f_r < 3f_r/2$ that can be modelled in the averaged codes and outside the full bandwidth of the undulator module—the sinc function envelope can be seen in Figure 4.7 and there are modes visible beyond the first minimum of this envelope. The spike lengths are correspondingly shorter: in this case the FWHM spike width is 57 as, which is 8 times shorter than in the Genesis 1.3 case, with the base width around

450 as which is the same as in the `Genesis 1.3` case. At 12.4 nm wavelength, 57 as is only 1.4 optical cycles. Scaling to shorter wavelengths, for a resonant wavelength of 0.15 nm a 1.4 optical cycle pulse would have a FWHM duration of 700 zs and an rms length of 300 zs.

Studying the evolution of the electron bunch longitudinal phase space shows the sinusoidal energy modulation gradually sheering and developing into a current modulation. The positions of the radiation spikes are initially aligned with the bottom of the energy modulation, for small $\bar{z}$, and as the interaction progresses and the energy modulation evolves into a current modulation the spikes shift to realign with the regions of enhanced peak current. The initial interpretation, which will be subject to further analysis, is that locking is achieved at first via the energy modulation, which gives a combined frequency and gain modulation to the system, then the gain modulation due to the current enhancement becomes dominant. This is the reason that the small sub-spikes between the dominant spikes are not evident, and why the frequency modes show no evidence of splitting.

This simulation shows that the process of mode-locking in the amplifier FEL is robust to the evolution of the beam energy modulation through the chicanes, and that this process ultimately provides a cleaner output pulse both temporally and spectrally. It also shows that the frequency bandwidth of the mode-locked FEL is far broader than originally thought, and that features with duration close to a single-cycle of the resonant wavelength are present in the output. It is clear therefore that non-averaged codes will be essential tools for further study of the mode-locked FEL.

4.6.2 Mode-Locking with Very Large Energy Spread Beam

The energy spread criterion (4.27), when applied to the 12.4 nm simulation case, gives $\sigma_\gamma/\gamma < 8 \times 10^{-4}$. This is consistent with experience using `Genesis 1.3` when it was found that for $\sigma_\gamma/\gamma = 10^{-3}$ the modal structure did not develop, but reducing the energy spread to $\sigma_\gamma/\gamma = 10^{-4}$ allowed the modal structure to emerge. However, simulations using the non-averaged code show clear mode-locking, although at reduced peak power, for significantly *greater* energy spread. An example is shown in Fig 4.8. Here the *rms* energy spread is $\sigma_\gamma/\gamma = 4 \times 10^{-3}$ (so the full energy spread is $\simeq 2.4\%$) which exceeds the criterion above, yet the growth of the modal structure and attosecond temporal structure is clear, with FWHM spike width of 192 as at 12.4 nm. However, the peak intensity

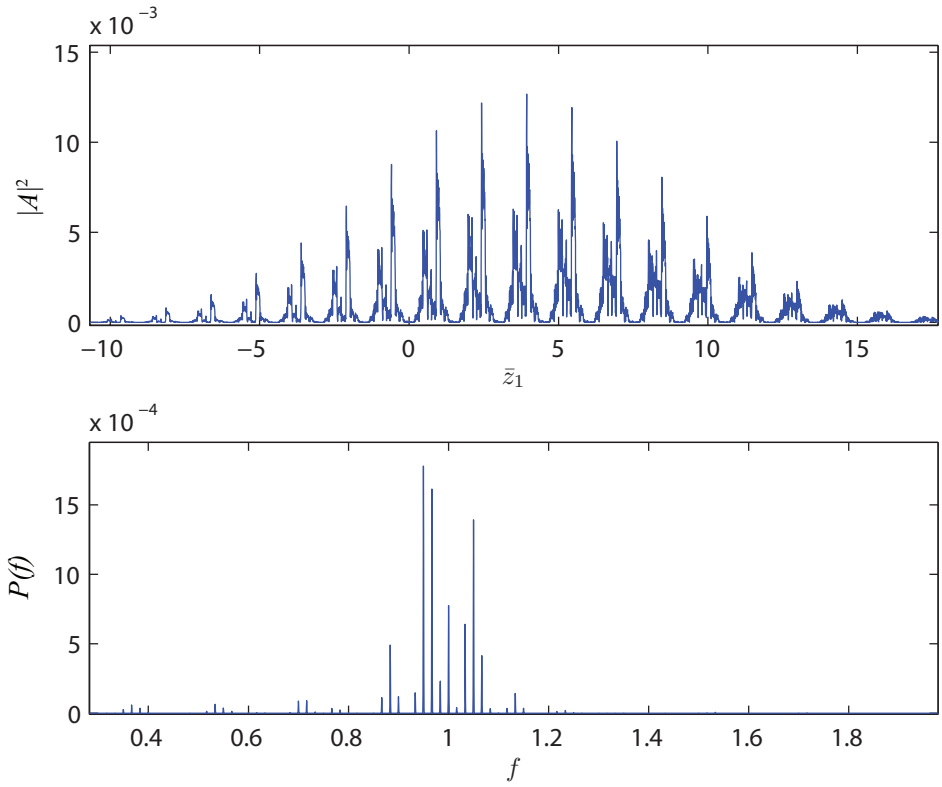

Figure 4.8: Simulation result from one-dimensional non-averaged code, for parameters equivalent to the 12.4 nm Genesis 1.3 mode-locking simulations, but with the energy spread increased to $\sigma_\gamma/\gamma = 4 \times 10^{-3}$. The FWHM spike length scales to 192 as.

is significantly reduced, to $|A|^2 \simeq 0.013$ equivalent to $\simeq$60 MW for the 12.4 nm case. The bandwidth of the radiation is extremely broad with modes visible at $f < f_r/2$, that is, outside the bandwidth that can be modelled in averaged codes.

The question of how the attosecond structure develops in the non-averaged simulation when the energy spread is far larger than the derived criterion is one for further study. However, these results indicate the potential for the mode-locking technique to be exploited on large energy spread electron beams, such as those produced by plasma-based accelerators which have demonstrated energy spreads of around 1%. A feature of the plasma beams is the extremely high peak current, in the tens of kA. If the results shown here are scaled to real powers assuming a 30kA electron beam, the peak power would be 0.6 GW. It is possible that it is the extremely broad bandwidth of the mode-locked FEL that allows it

Parameter	Value
Charge Q	1 pC
Energy E	1.7 GeV
Undulator Period λ_w	1.5 cm
FEL Wavelength λ_r	1 nm
Bunch Duration σ_b	1 fs
Energy Spread σ_E/E	10^{-4}
Normalised Emittance ε_n	0.1 mm-mrad
Average β-function $\langle\beta\rangle$	5 m
FEL Parameter ρ	8.4×10^{-4}

Table 4.3: Parameters for a potential low-charge mode of operation for the NGLS.

to couple with a large energy spread electron beam. This too is a topic for future study.

4.6.3 Mode-Locked Single-Spike SASE

Single-Spike SASE, as discussed in Section 2.7, is the regime of operation where the electron bunch length $l_b \leq 2\pi l_c$, in which case only a single SASE spike can develop. Some unpublished work has been done to assess the application of mode-locking to this regime, using as a parameter set a possible low-charge mode of operation for the Next Generation Light Source proposal by Lawrence Berkeley National Laboratory in the USA. The aim was to break the single SASE spike into a train of phase-locked attosecond pulses. The parameters of the FEL are listed in Table 4.3.

Figure 4.9(a) shows a typical single-spike SASE output pulse, simulated in the averaged one dimensional code used for most of the work in this thesis. The peak power is 600 MW, and the FWHM pulse duration 1.15 fs. The pulse is shown at saturation after an undulator length of 15 m. Figure 4.9(b) shows the results with mode-locking applied. The undulator modules have 50 periods, and the delay in the chicanes is 200 wavelengths, giving $S_e = 5$. A modulation of period 250 wavelengths has been applied to the electron beam energy of amplitude $\Delta E/E = \rho$. The pulse is shown after 10 m of undulator—the peak power is reduced by an order of magnitude compared to the SASE control case, because the slippage rate is enhanced and the radiation slips out of the electron bunch more quickly restricting the possible amplification, but the mode-locking has

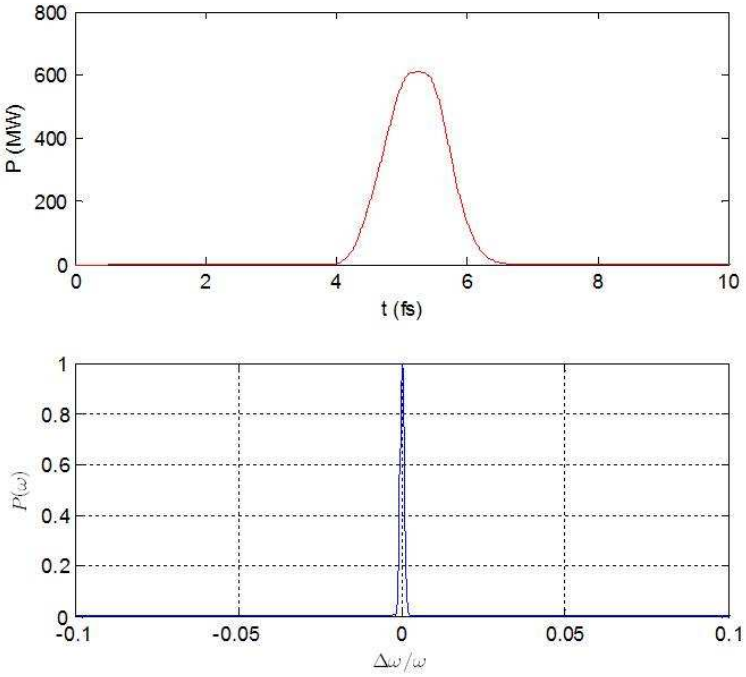

(a) Single Spike SASE Control.

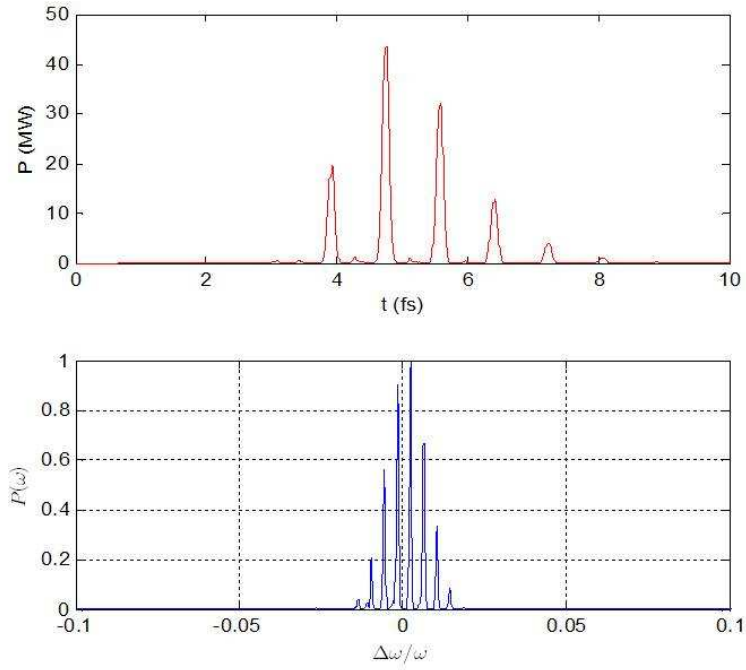

(b) Mode-Locking.

Figure 4.9: Mode-Locking applied to single spike SASE.

split the SASE pulse into a train of separate spikes, each of FWHM duration $\tau_p = 120$as.

4.6.4 Other Developments

The study of mode-locking in the FEL has been extended in a number of publications by the author and co-workers. The main results are briefly summarised here and the published papers are reproduced at the end of the thesis.

Attosecond Pulse Train Amplification

It was shown using three-dimensional simulations that the temporal structure of an attosecond pulse train, such as that generated via High Harmonic Generation (HHG) in noble gases, may be retained in a free electron laser amplifier through to saturation using a mode-locked configuration [31, 70]. At wavelength 12 nm, a train of attosecond pulses of widths ≈300 as with peak powers in excess of 1 GW were predicted, which is an amplification by a factor of 300 of the input field. No pre-conditioning of the electron beam (for example energy or current modulation) was required. The only requirement was that the mode-spacing of the FEL system matched the frequency comb spectrum of the HHG seed source.

Start-to-End Simulations

The mode-locked FEL was simulated in `Genesis 1.3` using a realistic electron bunch distribution incorporating the full physics of the generation, acceleration and transport of the beam from the cathode to the entrance of the undulator through a recirculating linac accelerator designed as a possible solution for the UK's New Light Source proposal [32, 71]. These simulations demonstrated that the mode-locked FEL is compatible with the present generation of radiofrequency accelerator designs. A study was made of the role of the electron beam energy modulation and it was shown how the pulses within the train align with the minima of the modulation. A relatively simple method of seeding the mode-locked FEL with a filtered HH source was shown to control the envelope and phase of the mode-locked pulse train. The limitations of averaged simulation codes were discussed, leading to the development of a criteria for the validity of these codes when simulating a system with an electron beam energy modulation. Finally, the use of coherent spontaneous emission in a mode-locked configuration

was discussed as this may offer a new method of generating short pulse trains of coherent, high power radiation without the need to rely upon the FEL interaction.

Mode-Locking in Oscillator FELs

An investigation was made of the application of the mode-locking concept to an oscillator free-electron laser [33]. A high-gain low-feedback oscillator utilising broadband mirrors, otherwise known as Regenerative Amplifier FEL (RAFEL), was shown in simulations to produce a mode-locked pulse at saturation with excellent pulse-to-pulse stability. The example shown, operating in the soft-X-ray, gave individual pulses conservatively estimated at ≈200 as duration at a wavelength of 3 nm. Scaled to the X-ray with wavelength $\lambda_r = 0.15$ nm, with $\rho = 5 \times 10^4$, such pulses are 24 as in duration. Such a system would require a method of modulating the electron bunch energy at the very high repetition rate required to match the cavity round trip time of the optical pulse, which may be challenging using a conventional seed source. One possibility would be to use a longer wavelength FEL as a beam modulator prior to the shorter wavelength mode-locked FEL, but as yet no real study has been made of this idea.

A feasibility study of demonstrating the mode-locked oscillator on a low gain FEL was also done, using the parameters of the ALICE IR-FEL [72] at Daresbury Laboratory as an example. The potential appeared very promising with simulations demonstrating clear evidence of mode generation and locking.

Chapter 5

Conclusions and Further Work

The original idea for the work presented in this thesis was to add delay chicanes along the FEL undulator to increase the slippage and improve the longitudinal coherence of SASE. The first results were published in 2010 [50] and the idea led eventually, through substantial simulation work solving the standard FEL equations (for which a full derivation is given in Chapter 2) and through some interpretation and simple theoretical analysis, to the technique called High-Brightness SASE described in Chapter 3. It was found in fact that to *really* improve the longitudinal coherence, to the point where it may be possible to generate a fully transform-limited FEL pulse in the hard X-ray, it is not sufficient to simply add chicanes to enhance the slippage. The important realisation was that repeatedly delaying the bunch creates interference effects in the FEL radiation, in the form of sidebands which can be quite widely separated from the FEL resonant frequency, and that because these sidebands have no fixed phase relationship they create a noisy periodic modulation in the output signal which limits its temporal coherence. To overcome this the delays must be made unequal which filters out the sidebands leaving a narrow bandwidth at resonance. Studies were made of the output properties of the HB-SASE radiation as a function of the length of the undulator modules and it was seen that the scheme is most effective when the undulator modules are shorter than a gain length. Comparisons were also made of the evolution of the radiation coherence length for normal SASE compared to HB-SASE and it was seen that the two systems were qualitatively different. In normal SASE, which is a local collective process between the coupled system of electrons and radiation, the coherence length was seen to saturate quite early in the interaction, at a value of around 3 cooperation lengths. For HB-SASE the

coherence length was seen to grow slowly at first, then just at the same position in the undulator where the SASE coherence length saturates, the HB-SASE coherence length enters a period of exponential growth. The explanation, which is consistent with HB-SASE working more effectively for shorter undulator modules, is that the HB-SASE technique is delocalising the collective FEL interaction.

The discovery of the sidebands in the spectrum was serendipitous because it was realised that the spectrum was analogous to the axial mode spectrum of a cavity laser. Adding equal delays in the chicanes has the effect of synthesising a very short optical cavity in the single pass amplifier FEL which allows techniques from conventional lasers to be applied analogously in the FEL to phase-lock the synthesised modes and generate extremely short pulses. This technique was called the Mode-Locked Amplifier FEL and was the subject of Chapter 4. Simulations of the technique for realistic parameters, using a well benchmarked three-dimensional code suggest pulse durations in the hard X-ray of around 23 attoseconds which is shorter than the atomic unit of time. Further study of the technique using a non-averaged code with wider bandwidth and sub-wavelength temporal resolution showed that the time structure of the FEL pulses could in fact be even shorter than this.

New codes are now available, such as a release of `Genesis 1.3` which incorporates electron movement along the beam (i.e. not confined to slices) and a fully three-dimensional, parallelised, non-averaged code called `Puffin` [73] which also incorporates variable polarisation within a single undulator lattice. These codes will now be used to improve the modelling of the HB-SASE and Mode-Locked FELs and their unique new features may allow new tricks to be played. For example new methods of locking the axial modes or broadening the bandwidth could be considered, such as alternating the undulator parameter from module to module to hop between the modes, or varying the polarisation in a periodic sequence. It may be possible to couple the modes to higher harmonics of the resonance as a way of stimulating harmonic emission and lasing at shorter wavelengths. Further study of some of some of the areas already identified, such as large energy spread beams, can also be done.

The development of a complete analytic theory describing HB-SASE and mode-locking is also an aim. Much progress has already been made using the linearisation techniques discussed in Chapter 2 [74] but plenty remains to be

done. Looking further ahead, experimental verification of some of the ideas presented in this thesis is a possibility. In fact, there has already been a proof of principle demonstration at LCLS of a scheme conceptually identical to HB-SASE. This is called iSASE [75] and the experiment used detuned LCLS undulators as delay sections to enhance the slippage—a factor of three reduction in linewidth was observed in agreement with expectation for the limited parameter range available [76]. Related theoretical work proposes the use of chicanes as delays. Another proposal uses subharmonic undulators as 'slippage boosted' sections [77]. There has also been a recent proposal for a mode-locked afterburner [78] in which the electron beam is 'prepared' within a standard FEL amplifier then injected into a much shorter afterburner comprising chicane delays and few-period undulator sections. Simulations of this scheme predict sub-attosecond pulses in the hard X-ray and the scheme has the attractive feature of being relatively easy to implement on an existing FEL facility. The other possibility is proof-of-principle demonstration on a low energy FEL test facility, such as the proposed CLARA accelerator at Daresbury Laboratory [79]. Both HB-SASE and Mode-Locking have been shown to be feasible on CLARA, with a Conceptual Design Report due out soon, so if funding becomes available experimental results may not be too far behind.

Bibliography

[1] B. W. J. M^{c}Neil, N. R. Thompson, and D. J. Dunning. Transform-Limited X-Ray Pulse Generation from a High-Brightness Self-Amplified Spontaneous-Emission Free-Electron Laser. *Phys. Rev. Lett.*, 110:134802, Mar 2013.

[2] N. R. Thompson and B. W. J. M^{c}Neil. Mode Locking in a Free-Electron Laser Amplifier. *Phys. Rev. Lett.*, 100:203901, 2008.

[3] J. M. J. Madey. Stimulated emission of bremsstrahlung in a periodic magnetic field. *J. Appl. Phys.*, 42:19061913, 1971.

[4] L. R. Elias, W. M. Fairbank, J. M. J. Madey, H. A. Schwettman and T. I. Smith. Observation of stimulated emission of radiation by relativistic electrons in a spatially periodic transverse magnetic field. *Phys. Rev. Lett.*, 36:717720, 1976.

[5] D. A. G. Deacon *et al.* First operation of a free electron laser. *Phys. Rev. Lett.*, 38:892894, 1977.

[6] B. W. J. M^{c}Neil and N. R. Thompson. X-ray Free-Electron Lasers. *Nature Photonics*, 4:814–821, 2010.

[7] W. A. Barletta *et al.* Free electron lasers: Present status and future challenges. *Nucl. Instrum. Methods Phys. Res. Sect. A*, 618(13):69–96, 2010. `http://www.sciencedirect.com/science/article/pii/S0168900210005656`.

[8] H. H. Braun. The Future of X-Ray FELs. In *Proc. of IPAC2012*, pages 4180–4183, 2012. `http://accelconf.web.cern.ch/AccelConf/IPAC2012/papers/fryap01.pdf`.

[9] A. M. Kondratenko and E. L. Saldin. Generation of coherent radiation by a relativistic electron beam in an ondulator. *Particle Accelerators*, 10:207, 1980.

[10] R. Bonifacio, C. Pellegrini, and L. Narducci. Collective Instabilities and High-Gain Regime in a Free-Electron Laser. *Opt. Commun.*, 50:373, 1984.

[11] R. Bonifacio *et al.* Spectrum, Temporal Structure and Fluctuations in a High-Gain Free-Electron Laser Starting from Noise. *Phys. Rev. Lett.*, 73:70, 1994.

[12] R. Bonifacio *et al.* Generation of XUV light by resonant frequency tripling in a two-wiggler FEL amplifier. *Nucl. Instrum. Methods Phys. Res. Sect. A*, 296:787, 1990.

[13] I. Ben-Zvi *et al.* Proposed UV FEL user facility at BNL. *Nucl. Instrum. Methods Phys. Res. Sect. A*, 304:151, 1991.

[14] L. H. Yu. Generation of intense UV radiation by subharmonically seeded single-pass free-electron lasers. *Phys. Rev. E*, 44:5178, 1991.

[15] L. H. Yu *et al.* High-Gain Harmonic-Generation Free-Electron Laser. *Science*, 289:932, 2000.

[16] G. Stupakov. Using the Beam-Echo Effect for Generation of Short-Wavelength Radiation. *Phys. Rev. Lett.*, 102:074801, 2009.

[17] D. Xiang *et al.* Demonstration of the Echo-Enabled Harmonic Generation Technique for Short-Wavelength Seeded Free-Electron Lasers. *Phys. Rev. Lett.*, 115:114801, 2010.

[18] J. Feldhaus *et al.* Possible application of X-ray optical elements for reducing the spectral bandwidth of an X-ray SASE FEL. *Opt. Commun.*, 140:341–352, 1997.

[19] E. L. Saldin *et al.* X-ray FEL with a meV bandwidth. *Nucl. Instrum. Methods Phys. Res. Sect. A*, 475:357–362, 2001.

[20] G. Geloni *et al.* A novel self-seeding scheme for hard X-ray FELs. *Journal of Modern Optics*, 58:1391–1403, 2011.

[21] J. Amann *et al.* Demonstration of self-seeding in a hard-X-ray free-electron laser. *Nature Photonics*, 6:693, 2012.

[22] R. Colella and A. Luccio. Proposal for a free electron laser in the X-ray region. *Opt. Commun.*, 50:41–44, 1984.

[23] K.-J. Kim *et al.* A Proposal for an X-Ray Free-Electron Laser Oscillator with an Energy-Recovery Linac. *Phys. Rev. Lett.*, 100:244802, 2008.

[24] B. W. J. M^{c}Neil. A simple model of the free electron laser oscillator from low into high gain. *IEEE J. Quant. Electron.*, 26:1124–1129, 1990.

[25] D. C. Nguyen *et al.* First lasing of the regenerative amplifier FEL. *Nucl. Instrum. Methods Phys. Res. Sect. A*, 429:125–130, 1999.

[26] B. Faatz *et al.* Regenerative FEL amplifier at the TESLA test facility at DESY. *Nucl. Instrum. Methods Phys. Res. Sect. A*, 429:424–428, 1999.

[27] Z. Huang and R. Ruth. Fully Coherent X-Ray Pulses from a Regenerative-Amplifier Free-Electron Laser. *Phys. Rev. Lett.*, 96:144801, 2006.

[28] B. W. J. M^{c}Neil *et al.* A design for the generation of temporally-coherent radiation pulses in the VUV and beyond by a self-seeding high-gain free electron laser amplifier. *New Journal of Physics*, 9:239, 2007.

[29] D. J. Dunning *et al.* Short wavelength regenerative amplifier free electron lasers. *Nucl. Instrum. Methods Phys. Res. Sect. A*, 593:116–119, 2008.

[30] B. W. J. M^{c}Neil, G. R. M. Robb, M. W. Poole, and N. R. Thompson. Harmonic Lasing in a Free-Electron Laser Amplifier. *Phys. Rev. Lett.*, 96:084801, 2006.

[31] B. W. J. M^{c}Neil, N. R. Thompson, D. J. Dunning, and B. Sheehy. High harmonic attosecond pulse train amplification in a Free Electron Laser. *J. Phys. B*, 44:065404, 2011.

[32] D. J. Dunning, B. W. J. M^{c}Neil, N. R. Thompson, and P. H. Williams. Start-to-end modelling of a mode-locked optical klystron free-electron laser amplifier. *Phys. Plasmas*, 18:073104, 2011.

[33] B. W. J. M^{c}Neil and N. R. Thompson. Cavity resonator free electron lasers as a source of stable attosecond pulses. *Europhys. Lett.*, 96:54004, 2011.

[34] W. B. Colson. One-body electron dynamics in a free electron laser. *Phys. Lett.*, 64A:190192, 1977.

[35] B. W. J. M^{c}Neil and R. R. M. Robb. Self-amplified coherent spontaneous emission in the planar wiggler free-electron laser. *Phys. Rev. E*, 65:046503, 2002.

[36] R. Bonifacio, R. M. Caloi, and C. Maroli. The slowly varying envelope approximation revisited. *Opt. Commun.*, 101:185–187, 1993.

[37] R. Bonifacio *et al.* Physics of the High-Gain FEL and Superradiance. *Riv. Nuovo Cimento*, 13(9):169, 1990.

[38] R. Bonifacio, F. Casagrande and L. De Salvo Souza. Collective variable description of a free-electron laser. *Phys. Rev. A*, 33(4):2836–2839, 1986.

[39] L. T. Campbell. *The Physics of a 4th Generation Light Source*. PhD thesis, University of Strathclyde, 2011.

[40] R. Bonifacio *et al.* New Effects in the Physics of High-Gain Free-Electron Lasers; a Proposed Experiment and Possible Applications. *Riv. Nuovo Cimento*, 15(11):152, 1993.

[41] J. W. Goodman. *Statistical Optics*. John Wiley & Sons Inc., 2000. See Chapter 5.

[42] E. L. Saldin, E. A. Schneidmiller, and M. V. Yurkov. Statistical and coherence properties of radiation from x-ray free-electron lasers. *New Journal of Physics*, 12:035010, 2010.

[43] R. Bonifacio, B. W. J. M^{c}Neil and P. Pierini. Superradiance in the high-gain free electron laser. *Phys. Rev. A*, 40:4467–4475, 1989.

[44] S. Reiche, P. Musumeci, C. Pellegrini, J. B. Rosenzweig. Development of ultra-short, single coherent spike for SASE X-ray FELs. *Nucl. Instrum. Methods Phys. Res. Sect. A*, 593:45–48, 2008.

[45] E. L. Saldin, E. A. Schneidmiller, and M. V. Yurkov. *The Physics of Free Electron Lasers*. Springer, 2000.

[46] B. W. J. M^{c}Neil, M. W. Poole, and G. R. M. Robb. Unified model of electron beam shot noise and coherent spontaneous emission in the helical wiggler free-electron laser. *Phys. Rev. Spec. Top. Accel. Beams*, 6:070701, 2003. See also reference [14] within.

[47] B. W. J. M^{c}Neil, G. R. M. Robb, D. J. Dunning, and N. R. Thompson. FELO: A One-Dimensional Time-Dependent FEL Oscillator Code. In *Proc. of FEL2006*, page 59, 2006.

[48] J. K. Jones, J. A. Clarke, and N. R. Thompson. A Compact, Modular Electron Beam Delay Line for Use in Novel Free-Electron Laser Schemes. In *Proc. of IPAC2012*, pages 1759–1761, 2012. TUPPP069.

[49] H. L. Owen and P. H. Williams. A modular path length corrector for recirculating linacs. *Nucl. Instrum. Methods Phys. Res. Sect. A*, 662:12–20, 2012.

[50] N. R. Thompson *et al.* Improved Longitudinal Coherence in SASE FELs. In *Proc. of IPAC2010*, pages 2257–2259, 2010. TUPE050.

[51] J. Wu, A. Marinelli, and C. Pellegrini. Generation of Longitudinally Coherent Ultra High Power X-Ray FEL Pulses by Phase and Amplitude Mixing. In *Proc. of FEL 2012*, 2012. also SLAC-PUB-15348.

[52] J. A. Clarke. *The Science and Technology of Undulators and Wigglers*. Oxford University Press, 2004.

[53] P. B. Corkum and F. Krausz. Attosecond Science. *Nature Physics*, 3:381–387, 2007.

[54] E. L. Saldin, E. A. Schneidmiller, and M. V. Yurkov. Scheme for attophysics experiments at a X-ray SASE FEL. *Opt. Commun.*, 212:377, 2002.

[55] E. L. Saldin, E. A. Schneidmiller, and M. V. Yurkov. Terawatt-scale sub 10-fs Laser Technology - Key to Generation of GW-level Attosecond Pulses in X-ray Free Electron Lasers. *Opt. Commun.*, 237:153, 2004.

[56] E. L. Saldin, E. A. Schneidmiller, and M. V. Yurkov. A New Technique to Generate 100 GW-level Attosecond X-ray Pulses from the Xray SASE-FELs. *Opt. Commun.*, 239:161, 2004.

[57] A. A. Zholents and W. M. Fawley. Proposal for Intense Attosecond Radiation from an X-Ray Free-Electron Laser. *Phys. Rev. Lett.*, 92:224801, 2004.

[58] A. A. Zholents and G. Penn. Obtaining Attosecond X-ray Pulses using a SASE-FEL. *Phys. Rev. Spec. Top. Accel. Beams*, 8:050704, 2005.

[59] A. A. Zholents *et al.* Current-enhanced SASE using an optical laser and its applicaion to the LCLS. In *Proc. of FEL2004*, pages 582–585, 2004. `http://www.jacow.org/`.

[60] A. A. Zholents. Method of an enhanced self-amplified spontaneous emission for x-ray free electron lasers. *Phys. Rev. Spec. Top. Accel. Beams*, 8:040701, 2005.

[61] P. Emma, Z. Huang, and M. Borland. Attosecond x-ray pulses in the LCLS using the slotted foil method. In *Proc. of FEL2004*, pages 333–338, 2004. `http://www.jacow.org/`.

[62] E. L. Saldin, E. A. Schneidmiller, and M. V. Yurkov. Self-amplified spontaneous emission FEL with energy-chirped electron beam and its application for generation of attosecond x-ray pulses. *Phys. Rev. Spec. Top. Accel. Beams*, 9(5):1–6, May 2006. `http://link.aps.org/doi/10.1103/PhysRevSTAB.9.050702`.

[63] A. E. Siegman. *Lasers*. University Science Books, Sausalito, USA, 1986. See chapter 27.

[64] E. Kur, D. J. Dunning, B. W. J. M^{c}Neil, J. Wurtele, and A. A. Zholents. A wide bandwidth free-electron laser with mode locking using current modulation. *New Journal of Physics*, 13, 2011. `http://dx.doi.org/10.1088/1367-2630/13/6/063012`.

[65] S. Reiche. GENESIS 1.3: a fully 3D time-dependent FEL simulation code. *Nucl. Instrum. Methods Phys. Res. Sect. A*, 429:243, 1999. Code available at `http://genesis.web.psi.ch/`.

[66] P. Emma *et al.* First lasing and operation of an angstrom-wavelength free-electron laser. *Nature Photonics*, 4:641 – 647, 2010.

[67] R. Bonifacio, R. Corsini, and P. Pierini. Theory of the high-gain optical klystron. *Phys. Rev. A*, 45:4091, 1992.

[68] R. Bonifacio, G. R. M. Robb, and B. W. J. M^{c}Neil. Propagation, cavity, and Doppler-broadening effects in the collective atomic recoil laser. *Phys. Rev. A*, 56:912, 1997. See Section V. A. which, while describing atomic bunching, is also valid for electrons.

[69] B. W. J. M^{c}Neil, G. R. M. Robb, and M. W. Poole. An Improved 1D Model for Ultra-High Power Radiation Pulse Propagation in the Helical Wiggler Free-Electron Laser. In *Proc. of PAC 2003*, pages 953–955, 2003. `http://www.jacow.org/`.

[70] B. W. J. M^{c}Neil, N. R. Thompson, and D. J. Dunning. Retention of attosecond pulse structure in an HHG seeded FEL Amplifier. In *Proc. of FEL2008*. `www.jacow.org`, 2008.

[71] D. J. Dunning, N. R. Thompson, P. H. Williams and B. W. J. M^{c}Neil. Start-To-End Simulations of SASE and HHG-Seeded Mode-Locked FEL. In *Proc. of FEL2009*, 2009.

[72] N. R. Thompson, D. J. Dunning, J. A. Clarke, M. Surman, A. D. Smith, Y. Saveliev, and S. Leonard. First lasing of the {ALICE} infra-red free-electron laser. *Nucl. Instrum. Methods Phys. Res. Sect. A*, 680(0):117 – 123, 2012.

[73] L. T. Campbell and B. W. J. M^{c}Neil. PUFFIN: a three-dimensional, unaveraged free-electron laser simulation code. *Phys. Plasmas*, 19:093119, 2012. `http://dx.doi.org/10.1063/1.4752743`.

[74] B. W. J. M^{c}Neil, 2012. Private Communication.

[75] J. Wu, C. Pellegrini, and A. Marinelli. Generation of Longitudinally Coherent Ultra High Power X-Ray FEL Pulses by Phase and Amplitude Mixing. In *Proc. of FEL 2012*, page 237, 2013. TUPD07.

[76] J. Wu and C. Pellegrini, 2012. Private Communication.

[77] D. Xiang, Y. Ding, Z. Huang, and H. Deng. Purified self-amplified spontaneous emission free-electron lasers with slippage-boosted filtering. *Phys. Rev. Spec. Top. Accel. Beams*, 16:010703, 2013.

[78] D. J. Dunning, B. W. J. M^{c}Neil, and N. R. Thompson. Few-Cycle Pulse Generation in an X-Ray Free-Electron Laser. *Phys. Rev. Lett.*, 110:104801, Mar 2013.

[79] J. A. Clarke *et al.* The Conceptual Design of CLARA, a Novel Test Facility for Ultrashort Pulse Generation. In *Proc. of IPAC 2013*, page 1265, 2013. TUPEA058.

Publications

Refereed Publications

- N. R. Thompson and B. W. J. M^{c}Neil, Mode Locking in a Free-Electron Laser Amplifier, *Phys. Rev. Lett.*, 100:203901, 2008.
  —I led this research under the supervision of M^{c}Neil.

- B. W. J. M^{c}Neil, N. R. Thompson, D. J. Dunning and B. Sheehy, High harmonic attosecond pulse train amplification in a Free Electron Laser, *Journal of Physics B: Atomic, Molecular & Optical Physics*, 44:065404, 2011.
  —I helped plan the research and interpret the results.

- D. J. Dunning, B. W. J. M^{c}Neil, N. R. Thompson and P. H. Williams, Start-to-end modelling of a mode-locked optical klystron free-electron laser amplifier, *Physics of Plasmas*, 18:073104, 2011.
  —I helped plan the research and interpret the results.

- B. W. J. M^{c}Neil and N. R. Thompson, Cavity resonator free electron lasers as a source of stable attosecond pulses, *Europhysics Letters*, 96:54004, 2011.
  —This was led my M^{c}Neil. I performed simulations and helped develop the concepts and plan the research.

- D. J. Dunning, B. W. J. M^{c}Neil and N. R. Thompson, Few-Cycle Pulse Generation in an X-Ray Free-Electron Laser, *Phys. Rev. Lett.*, 110:104801, Mar 2013.
  —This was led by Dunning. I helped write the paper.

- B. W. J. M^{c}Neil, N. R. Thompson and D. J. Dunning, Transform-Limited X-Ray Pulse Generation from a High-Brightness Self-Amplified Spontaneous-Emission Free-Electron Laser, *Phys. Rev. Lett.*, 110:134802, Mar 2013.

—This is my original concept developed under supervision of M^{c}Neil and assisted by Dunning.

Conference Publications

- B. W. J. M^{c}Neil, N. R. Thompson and D. J. Dunning, Retention of attosecond pulse structure in an HHG seeded FEL Amplifier, *In Proceedings of FEL 2008*, 2008.

- D. J. Dunning, N. R. Thompson, P. H. Williams and B. W. J. M^{c}Neil, Start-To-End Simulations of SASE and HHG-Seeded Mode-Locked FEL, *In Proceedings of FEL 2009*, 2009.

- N. R. Thompson, D. J. Dunning and B. W. J. M^{c}Neil, Improved Longitudinal Coherence in SASE FELs, *In Proc. of IPAC 2010*, pages 22572259, 2010. TUPE050.

- J. A. Clarke, J. K. Jones and N. R. Thompson, A Compact, Modular Electron Beam Delay Line for Use in Novel Free-Electron Laser Schemes, *In Proc. of IPAC 2012*, pages 17591761, 2012. TUPPP069.

Invited Talks

- High Brightness SASE operation of X-ray FELs, *Physics and Applications of High Brightness Beams: Towards a Fifth Generation Light Source*, San Juan Marriott Resort, Puerto Rico, March 25-28, 2013. `http://pbpl.physics.ucla.edu/HBEB2013/`

Contributed Talks

- Improved temporal coherence in SASE FELs and generation of ultrashort pulses by mode-locking a SASE FEL, *International Workshop on Frontiers in FEL Physics and Related Topics*, Elba Island, Tuscany (Italy), September 8-14, 2007. `http://www.lnf.infn.it/conference/elba07/`